# Finite-size scaling for lattice fermions in two dimensions

Dissertation
zur Erlangung des akademischen Grades
Dr. rer. nat.
an der Mathematisch-Naturwissenschaftlichen Fakultät
der Universität Augsburg

vorgelegt von

Antonio Hill

Augsburg, Dezember 2012

# Contents

# 1. Introduction

The prediction by Anderson in 1958 [1], that electronic states can become localized in a spatial region of a solid, has opened a new field in condensed matter physics, namely Anderson localization [2, 3]. He was the first to recognize that extended states, existing in a perfect metal, can become exponentially localized when the amount of disorder is above a critical value. This implies that states have to undergo a metal-insulator or Anderson transition under certain conditions.

Let us suppose you have a perfect metal where electrons do not scatter. As a consequence, conductivity is infinite. However, from experimental experience we know that the conductivity in metals is finite. The reason is that a real metal is by no means perfect and electrons scatter at vacancies or impurities. In a simplified picture charge carriers are considered to perform random walks in the metal, resulting in diffusion and, thus, to a finite conductivity. What happens if we increase the number of impurities and thus disorder? Naively, one would expect that this leads to an increasing diffusion constant and, therefore, increasing resistivity. But it turned out to be different.

Anderson has shown in his pioneering work that there exists a mobility edge and electron wave functions become exponentially decaying when reaching a certain amount of disorder. In this case diffusion is absent and, consequently, charge carriers are trapped and can not contribute to transport anymore. The metal gets insulating which is a purely quantum effect (at zero temperature) due to interference of the wave function.

The next major step towards a better understanding of the disorder driven metal-insulator transition was made when Abrahams et al. [4] introduced their scaling theory of localization. They discussed the behavior of the conductance of a finite system under change of its size $L$ leading to the $\beta$-function $(d \ln g / d \ln L)$ of the conductance $g$. The behavior of this function indicates under which conditions an Anderson transition is expected. It turned out that for spinless and non-interacting electrons this transition only exists in dimensions $d > 2$. Meaning that any amount of disorder in two dimensions must lead to localization even though the localization length might be larger than the system size.

At this time in the early 1980ies, computers began to play a greater role in physics and Pichard and Sarma [5] introduced a numerical method for the localization length and also a scaling theory. This transfer matrix approach allows to calculate the localization length of electron wave functions on finite strips and was

originally used in the context of stochastic dynamical systems (cf. e.g. Ref. [6]). The simplest model for this is the Anderson Hamiltonian which consists of a hopping term and a diagonal term with random on-site energies. MacKinnon and Kramer introduced a further numerical method using Green functions [7, 8] for the localization length. They have shown the Anderson transition for a three dimensional cubic lattice and have calculated the critical exponent of the localization length at the metal-insulator transition using finite-size scaling. The question of whether this transition and thus, the critical exponent is universal (i.e. independent of the underlying model) is still debated.

In two dimensions it has been shown, at least for relatively strong disorder, that a metal-insulator transition does not occur [9, 10]. But it is still unclear whether states are truly exponentially localized for weak disorder or whether the wave function decays with a power-law [5, 11, 12]. Questions have been raised whether there might be a transition from power-law localized states to exponentially localized states [11, 13, 14]. Currently, this rigorous argument is no longer valid and several Anderson transitions are known to exist in two dimensions [15]. Probably the best known example is the quantum Hall transition. The discovery of the quantized Hall effect by von Klitzing [16, 17] had a huge impact and there has been a great effort to understand this effect to this day. It is believed that the quantum Hall transition also belongs to the class of Anderson transitions. Chalker and Coddington came up with a network model describing the transition between plateaux [18]. Indeed, their model using the transfer matrix approach shows a critical point. Somewhat later Dirac fermions were proposed as a model for understanding the quantum Hall effect. Haldane suggested a model for the quantized Hall effect without magnetic field using a honeycomb lattice [19]. Ludwig et al. gave an alternative approach to the quantum Hall transition deriving Dirac fermions from a square lattice with half a magnetic flux quantum per plaquette [20]. The latter authors observed that the Hall conductivity of a single Dirac fermion acquires a finite value when its mass is non-zero in the absence of disorder. A further indication for Dirac fermions was the mapping from the Chalker Coddington model to a Dirac Hamiltonian [21]. Despite the progress made, it remains unclear if Dirac fermions or their lattice realizations share the same transition.

The Dirac equation was introduced by Paul A. M. Dirac uniting the principles of quantum mechanics and special relativity. His equation, originally formulated for electrons [22], describes relativistic particles with spin 1/2, thus describing fermions, and their anti-particles. A major property of Dirac fermions is the linear dependence of the energy on momentum. This is in direct contrast to particles described by the Schrödinger equation, which show quadratic dispersion. Four years before Haldanes paper, Semenoff introduced a two dimensional lattice realization of Dirac fermions on a honeycomb lattice as a single layer of graphite. The

band structure of graphite and, consequently, the linear momentum dependence for small energies of a single layer, was already known since 1947 [23], but it was common belief that such a system could not be stable. Nevertheless, in 2004 the model of Semenoff became reality when Novoselov and Geim [24] managed to prepare samples made of monocrystalline graphitic films, later called graphene. They were able to connect leads to a single graphene sheet and showed that graphene has a minimal conductivity of order $\approx e^2/h$. Moreover, a new type of quantum Hall effect has been discovered [25], where a half integer plateau exists at zero carrier density. Both findings are explained by using two dimensional Dirac fermions. The minimal conductivity can be calculated by means of the Kubo formalism [20, 26, 27] or the Landauer approach [28]. The unconventional Hall effect can be justified by Landau levels [29, 30], which are different as for a usual two dimensional electron gas.

Further examples where Dirac fermions are present are fullerenes [31, 32] and topological insulators [33, 34, 35, 36]. Whereas it was interesting to study Dirac fermions in order to gain wider understanding of the quantum Hall transition in the past, the driving force today is graphene and topological insulators.

Using a quantum field theoretical approach, it has been shown that Dirac fermions can undergo a metal-insulator transition [37, 38] and a similar transition has also been found numerically [39]. This has drawn our attention to lattice fermions and in particular on the question "Is there a metal-insulator transition and, if so, is it universal?". It is due to this question that we have been encouraged to adapt the transfer matrix approach to lattice fermions and to investigate Anderson localization using finite-size scaling.

## Outline of this thesis

In this thesis we study the influence of disorder on Dirac fermions in the continuous case and realized on various lattices, which we refer to as lattice fermions. We discuss the origin of Dirac fermions in graphene as a prominent example in chapter 2. In chapter 3 the concept of transfer matrices is introduced and applied to calculations of transmission coefficients for the continuous case in one dimension. We extend this concept in chapter 4 and implement an algorithm for calculations of Lyapunov characteristic exponents in one and two spatial dimensions. Before we turn to numerical calculations, the method of finite-size scaling is introduced in chapter 5.

In chapter 6 we discretize the Dirac equation, in such manner that we can avoid the problem of fermion doubling, followed by the construction of a transfer matrix. The introduced model allows to study the influence of multiple fermions. Whenever possible, we compare between results of different models or methods. Moreover, we compare results for a special case with perturbation theory.

The remaining chapters are devoted to simulations for two dimensional lattice fermions, where we consider lattice fermions with random gap in chapter 7 and perform finite-size scaling analysis. For random scalar potential this is carried out in chapter 8. In both cases we find an Anderson transition and for random gap our analysis leads to a phase diagram. Finally, in chapter 9, we treat the random mass problem using tight-binding models for lattice fermions and show that results can be compared with certain results from chapter 7. In the last chapter our findings are summarized and a conclusion is drawn.

# 2. Dirac fermions in graphene

Graphene is a single layer of carbon atoms arranged in a honeycomb lattice. Most of its celebrated properties can be attributed to its lattice structure [24, 25, 29] leading to a linear momentum dependence of the spectrum for low energies. The probably most important property is the minimal conductivity, already mentioned in the introduction. Although the density of states for Dirac fermions in two dimensions is zero at the neutrality point ($E = 0$) the conductivity is finite and of the order of $e^2/h$. Moreover, the spacing of Landau levels for Dirac fermions is proportional to $\sqrt{n}$, with $n$ being the index of a Landau level, whereas it is proportional to $n$ for a usual two dimensional electron gas.

In this section we like to give the basis for understanding the latter and to clarify the origin of Dirac fermions. For this reason, let us start with the tight-binding description of electrons in graphene.

## 2.1. Tight-binding model

The honeycomb lattice is composed of two triangular lattices both tilted by an angle of $\pi/3$ with respect to each other [23, 40]. We refer to lattice points of one sublattice as type A and B respectively cf. figure 2.1. Each carbon atom of type $A$ has three neighbors of type $B$ linked with strong $\sigma$ bonds, which are a result of $sp^2$ hybridization of the $2s$, $2p_x$ and $2p_y$ orbitals.

The electron in the $2p_z$ orbital, perpendicular to the sheet, forms a weak $\pi$ bond by overlap of two half-filled $2p_z$ orbitals. These $\pi$ electrons can tunnel from site to site and are well described with a tight-binding Hamiltonian [41, 42, 43]

$$H = -t \sum_{<r_A, r_B>} c_A^\dagger c_B + H.c. \, , \tag{2.1}$$

where $t \approx 2.8eV$ is the hopping parameter, $c_i^\dagger$ ($c_i$) is the creation (annihilation) operator of an electron at site $A$ and $B$ respectively. The summation is taken over all pairs of nearest neighbors. The lattice can also be viewed as a triangular lattice composed of two atoms per unit cell with basis vectors

$$\mathbf{v}_1 = \tfrac{a}{2}(3, \sqrt{3}), \quad \mathbf{v}_2 = \tfrac{a}{2}(3, -\sqrt{3}) \, , \tag{2.2}$$
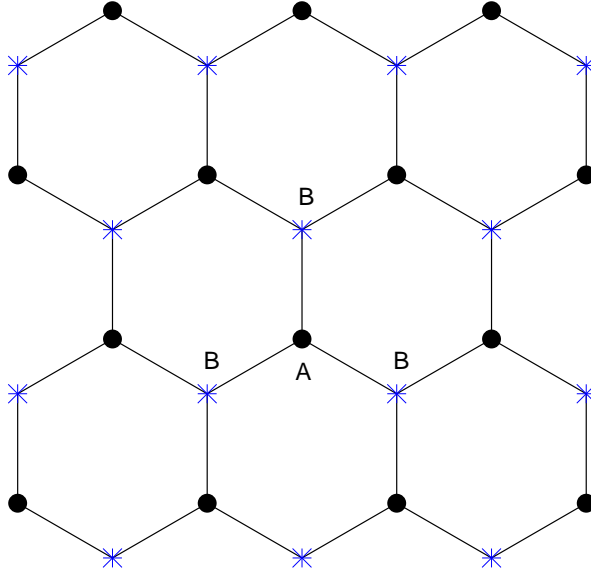
**Figure 2.1.:** Honeycomb lattice composed of two sublattices $A$ and $B$.

where $a = 1.42\text{Å}$ denotes the lattice constant. Using a Fourier representation of the operators

$$c_A = \int_{\Omega_B} \frac{d^2k}{(2\pi)^2} \exp(i\mathbf{k} \cdot \mathbf{A})\, \tilde{c}_A, \quad c_B = \int_{\Omega_B} \frac{d^2k}{(2\pi)^2} \exp(i\mathbf{k} \cdot \mathbf{B})\, \tilde{c}_B, \qquad (2.3)$$

where $\Omega_B$ is the area of the Brillouin zone and $\mathbf{A}, \mathbf{B}$ are the coordinates of sites $A, B$, the Hamiltonian is given by [40]

$$\mathcal{H} = \int_{\Omega_B} \frac{d^2k}{(2\pi)^2} \left( \tilde{c}_A^\dagger,\ \tilde{c}_B^\dagger \right) \begin{pmatrix} 0 & \sum_{i=1}^3 \exp(\mathbf{a}_i \cdot \mathbf{k}) \\ \sum_{i=1}^3 \exp(-\mathbf{a}_i \cdot \mathbf{k}) & 0 \end{pmatrix} \begin{pmatrix} \tilde{c}_A \\ \tilde{c}_B \end{pmatrix}, \quad (2.4)$$

with nearest neighbor vectors

$$\mathbf{a}_1 = a(0, -1), \quad \mathbf{a}_2 = \tfrac{a}{2}(\sqrt{3}, 1), \quad \mathbf{a}_3 = \tfrac{a}{2}(-\sqrt{3}, 1). \qquad (2.5)$$

Equivalently we can write the Hamiltonian matrix in sublattice representation [19, 26]

$$H = h_1 \sigma_1 + h_2 \sigma_2, \qquad (2.6)$$

where $\sigma_i$ are the Pauli matrices

$$\sigma_0 = \begin{pmatrix} 1 & 0 \\ 0 & 1 \end{pmatrix} \qquad \sigma_1 = \begin{pmatrix} 0 & 1 \\ 1 & 0 \end{pmatrix} \qquad \sigma_2 = \begin{pmatrix} 0 & -i \\ i & 0 \end{pmatrix} \qquad \sigma_3 = \begin{pmatrix} 1 & 0 \\ 0 & -1 \end{pmatrix} \qquad (2.7)$$

and

$$h_1 = -t \sum_{i=1}^{3} \cos(\mathbf{a}_i \cdot \mathbf{k}), \qquad h_2 = -t \sum_{i=1}^{3} \sin(\mathbf{a}_i \cdot \mathbf{k}) . \qquad (2.8)$$

This representation is very convenient not only the energy dispersion

$$E = \pm \sqrt{h_1^2 + h_2^2} \qquad (2.9)$$

can easily be obtained, but the Hamiltonian has a Dirac like structure, too. The naming will be explained below. After some elementary transformations of equation (2.9) we end up with

$$E(k_x, k_y) = \pm t \sqrt{3 + 2\cos\left(\sqrt{3}\, a\, k_x\right) + 4\cos\left(\frac{\sqrt{3}}{2}\, a\, k_x\right)\cos\left(\frac{3}{2}\, a\, k_y\right)} . \qquad (2.10)$$

Let us now take a closer look at the energy dispersion to clarify the origin of the reference to Dirac. The resulting spectrum is shown as a density plot in figure 2.2 and as a typical band structure plot along the high symmetry axes in figure 2.3.



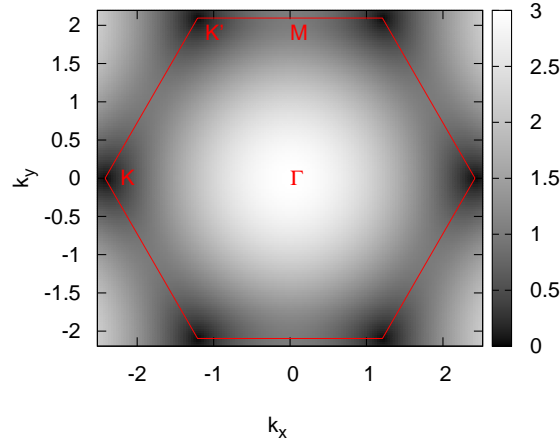**Figure 2.2.:** Density plot of the bandstructure of graphene, the energy is in units of $t$. Brillouin zone and points of high symmetry are marked in red.

As a direct consequence of the sublattice structure the spectrum has two bands, the valence and the conduction band. Both bands touch each other at two distinct points $K$ and $K'$, the so-called Dirac points, and in the vicinity of these points the
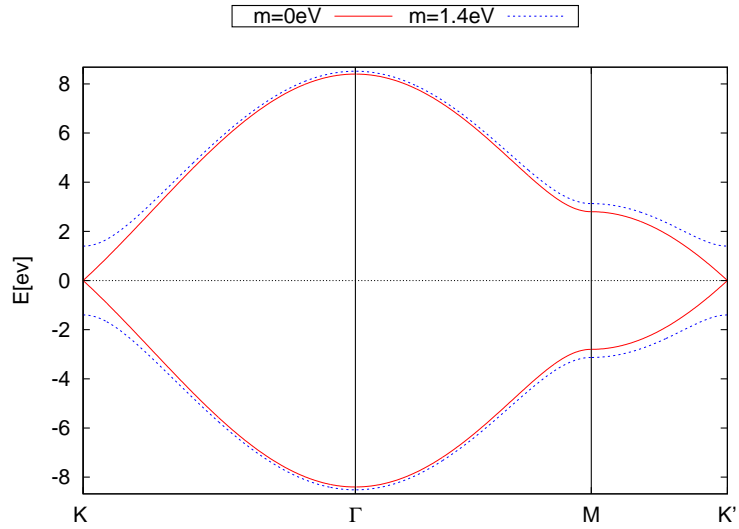
**Figure 2.3.:** Band structure of graphene along the high symmetry axes for the ungapped (red line) and the gapped case (blue line).

energy spectrum is linear in momentum. In undoped graphene the valence band is fully occupied and the conduction band is empty. If we look at figure 2.2, it seems that there are six Dirac points with coordinates

$$\mathbf{b}_1^\pm = \frac{4\pi}{3\sqrt{3}a}(\pm 1, 0) \quad \mathbf{b}_2^\pm = \frac{2\pi}{3\sqrt{3}a}(-1, \pm\sqrt{3}) \quad \mathbf{b}_3^\pm = \frac{2\pi}{3\sqrt{3}a}(1, \pm\sqrt{3}) \tag{2.11}$$

but each cone only contributes with one third, since they all lie at the border of the Brillouin zone. The total band width in graphene is $\Delta E = 6t \approx 16.8eV$. Furthermore, the influence of thermal fluctuations, even at room temperatures, is small. The reason is that the hopping rate is large, compared to the energy scale of typical fluctuations. Accordingly, temperature effects can be mostly neglected, this makes it for example possible to observe the quantum Hall effect at room temperatures [44].

The next property we like to draw attention on, is, that in vicinity of each Dirac point the dispersion is linear in momentum, exhibiting a cone like structure. A Taylor expansion around each Dirac cone indeed gives the linear behavior

$$E = \pm\hbar v_F |\mathbf{k} + \mathbf{b}_i^\pm| \,. \tag{2.12}$$

This is equivalent to the dispersion of the Dirac equation in two dimensions, where $v_F = 3ta/2$ is the corresponding "speed of light", which is actually 300 times slower in graphene. After shifting $\mathbf{k} \to \mathbf{k} - \mathbf{b}_i^\pm$, we can describe the low-energy behavior of quasi particles in graphene with the Dirac Hamiltonian

$$H = -\hbar v_F (k_x \sigma_1 + k_y \sigma_2) \,. \tag{2.13}$$

This approximation is reasonable if scattering between two Dirac cones can be ruled out and if energies are smaller then $E \approx 0.2eV$. The latter corresponds to infrared light of wavelength $\approx 6\mu m$. Note, that by replacing $k_i \to h_i$ we recover the original Hamiltonian (2.6) for the honeycomb lattice (neglecting prefactors). In real space the effective low-energy Hamiltonian reads

$$H = -i\hbar v_F(\sigma_1\partial_x + \sigma_2\partial_y)\,. \tag{2.14}$$

All this is in contrast to usual semiconductor physics, where the energy dispersion has parabolic shape, and thus, can be described by the Schrödinger equation with an effective mass [45, 46]. In graphene low-energy transport properties can be described using the Dirac equation and for several properties, like the conductivity, there are analytical solutions [27, 28].

We have seen that a tight-binding description of electrons, moving on a honeycomb lattice, results directly in two bands. Both bands touch each other at two distinct points and exhibit a linear dispersion for small energies, wich can be described by the Dirac equation. This made graphene very popular because people got enthusiastic about the new material with relativistic massless particles.

### 2.1.1. Breaking the sublattice symmetry and generating mass

As graphene might be a candidate for future transistors [47], it is of great interest to understand the mechanism which creates a gap. Since the origin of the sublattice symmetry are the two identical carbon atoms at sites $A$ and $B$, this symmetry can be broken by replacing one atom. In experiments this can be done by adsorption of atoms on the graphene sheet, for example hydrogen [48]. The energy difference of electrons located on site $A$ and $B$, parametrized as $m$, results in a gap between valence and conduction band [40]. The Hamiltonian for this case in $k$-space reads

$$\mathcal{H} = \int_{\Omega_B} \frac{d^2k}{(2\pi)^2} \ \left(\tilde{c}_A^\dagger, \ \tilde{c}_B^\dagger\right) \begin{pmatrix} m & \sum_{i=1}^3 \exp(\mathbf{a}_i \cdot \mathbf{k}) \\ \sum_{i=1}^3 \exp(-\mathbf{a}_i \cdot \mathbf{k}) & -m \end{pmatrix} \begin{pmatrix} \tilde{c}_A \\ \tilde{c}_B \end{pmatrix}\,. \tag{2.15}$$

In sublattice representation the Hamiltonian matrix gets

$$H = h_1\sigma_1 + h_2\sigma_2 + m\sigma_3\,, \tag{2.16}$$

with the energy dispersion

$$E = \pm\sqrt{h_1^2 + h_2^2 + m^2}\,. \tag{2.17}$$

For the effective low-energy Hamiltonian it follows

$$H = -\hbar v_F(k_x\sigma_1 + k_y\sigma_2) + \hbar v_F^2\, m\sigma_3, \quad E = \pm\hbar v_F\sqrt{k_x^2 + k_y^2 + m^2}\,, \tag{2.18}$$

where $m$ is the mass of the relativistic particle.

In summary this means that by breaking the sublattice symmetry we open a uniform gap at each Dirac cone cf. figure 2.3, which leads to massive Dirac fermions in the low-energy approximation. In this thesis the brickwork lattice and the low-energy approximation serves as a basis for later models for calculations of the localization length using a transfer matrix approach to study scaling behavior and the influence of disorder.

# 3. Transfer matrix approach

In this chapter we like to present the concept of transfer matrices as a introduction. A more detailed discussion can be found, for example, in textbook [49]. Suppose the following setup shown in figure 3.1. Waves are sent into a sample and due to scattering processes parts are reflected and transmitted. The probably easiest example, where this can be studied, is scattering at a potential barrier in one dimensional quantum mechanics. The wave functions are described by the Schrödinger equation, and from the continuation conditions, reflection and transmission amplitudes can be calculated.

A different approach to describe the same situation is to introduce a so called transfer matrix. This matrix relates wave functions from one side of a sample to
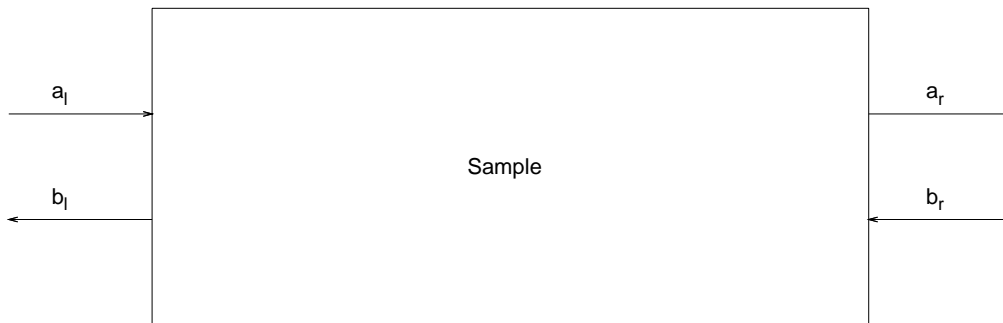


**Figure 3.1.:** Setup for a typical scattering experiment, the arrows represent in- and outgoing waves.

the other

$$\psi_{right} = T \ \psi_{left} \tag{3.1}$$

and wave functions $\psi_{left/right} = (a_{l/r} \ b_{l/r})^T$ are superpositions of in- and outgoing waves. Whereas the scattering matrix defined through

$$\begin{pmatrix} b_l \\ a_r \end{pmatrix} = \begin{pmatrix} r & t' \\ t & r' \end{pmatrix} \begin{pmatrix} a_l \\ b_r \end{pmatrix} = S \begin{pmatrix} a_l \\ b_r \end{pmatrix} , \tag{3.2}$$

relates in- and outgoing waves, with transmission $(t, t')$ and reflection amplitudes $(r, r')$. Transmission from left to right is described by $t$ and reflection on the left

by $r$. One major difference between both approaches is that the transfer matrix is multiplicative

$$\psi_3 = T_2 T_1 \ \psi_1 \Rightarrow \psi_L = \prod_{n=1}^{L} T_n \ \psi_1 \tag{3.3}$$

and an arbitrary number of samples can be connected by multiplication of the corresponding transfer matrices

$$\begin{pmatrix} a_r \\ b_r \end{pmatrix} = \mathcal{M} \begin{pmatrix} a_l \\ b_l \end{pmatrix} \quad \mathcal{M} = \prod_{n=1}^{L} T_n \, . \tag{3.4}$$

Using elementary transformations we can express $\mathcal{M}$ with elements of $S$ [50, 51]

$$\mathcal{M} = \begin{pmatrix} t' - rt^{-1}r' & rt^{-1} \\ t^{-1}r' & t^{-1} \end{pmatrix} \, . \tag{3.5}$$

## 3.1. Application to Dirac fermions in one dimension

Since the solution of scattering at a potential barrier for a one dimensional Schrödinger particle can be found in any textbook on introductory quantum mechanics (e.g. Ref. [52]), we like to illustrate the concept of transfer matrices considering Dirac fermions in one dimension.

### 3.1.1. Transmission through a massive barrier

A massive fermion is described by the time independent Dirac equation

$$\left( -i\hbar v_F \, \sigma_1 \, \partial_x + v_F^2 \, m \, \sigma_3 - E\sigma_0 \right) \psi(x) = 0 \, , \tag{3.6}$$

where $v_F$ is a velocity, $m$ the fermion mass and $\sigma_i$ are the usual Pauli matrices, given by equation (2.7), with energy dispersion

$$E = \pm\sqrt{k^2 + m^2}.$$

For simplicity we have also set $\hbar$ and $v_F$ to unity. Let now the mass be a function of space where the incident wave is scattered

$$m(x) = \begin{cases} 0 & \text{for } x < a \quad \text{region I} \\ m & a < x < b \quad \text{region II} \\ 0 & x > b \qquad \text{region III} \, . \end{cases}$$

Then, a general solution of equation (3.6) in the three regions is given by

$$\psi(x) = \begin{cases} A \begin{pmatrix} 1 \\ 1 \end{pmatrix} \exp(ikx) + B \begin{pmatrix} -1 \\ 1 \end{pmatrix} \exp(-ikx) & \text{for } x < a \\ C \begin{pmatrix} \xi \\ 1 \end{pmatrix} \exp(iqx) + D \begin{pmatrix} -\xi \\ 1 \end{pmatrix} \exp(-iqx) & a < x < b \\ E \begin{pmatrix} 1 \\ 1 \end{pmatrix} \exp(ikx) + F \begin{pmatrix} -1 \\ 1 \end{pmatrix} \exp(-ikx) & x > b \end{cases}$$

with $\xi = \sqrt{(E + m)/(E - m)}$ and $q = \sqrt{E^2 - m^2}$ in the region with finite mass. In order to find the matrix which fulfills the following relation

$$\psi(b) = \mathcal{M}\psi(a)$$

$$\begin{pmatrix} E \exp(ikb) \\ E \exp(ikb) \\ -F \exp(-ikb) \\ F \exp(-ikb) \end{pmatrix} = \mathcal{M} \begin{pmatrix} A \exp(ika) \\ A \exp(ika) \\ -B \exp(-ika) \\ B \exp(-ika) \end{pmatrix}, \tag{3.7}$$

we use continuity of the wave function $\psi^I(a) = \psi^{II}(a)$ and $\psi^{II}(b) = \psi^{III}(b)$. This leads to four equations

$$A \exp(ika) - B \exp(-ika) = C\xi \exp(iqa) - D\xi \exp(-iqa)$$
$$A \exp(ika) + B \exp(-ika) = C \exp(iqa) + D \exp(-iqa)$$
$$E \exp(ikb) - F \exp(-ikb) = C\xi \exp(iqb) - D\xi \exp(-iqb)$$
$$E \exp(ikb) + F \exp(-ikb) = C \exp(iqb) + D \exp(-iqb).$$

Multiplying the second equation by $\xi$ and adding (subtracting) the first, then adding (subtracting) the third equation to (from) the fourth gives

$$C = \frac{1}{2\xi} \exp(-iqa)\{A(\xi + 1) \exp(ika) - B(\xi - 1) \exp(-ika)\}$$
$$D = \frac{1}{2\xi} \exp(iqa)\{A(\xi - 1) \exp(ika) + B(\xi + 1) \exp(-ika)\}$$
$$2E \exp(ikb) = C(1 + \xi) \exp(iqb) + D(1 - \xi) \exp(-iqa)$$
$$2F \exp(-ikb) = C(1 - \xi) \exp(iqb) + D(1 + \xi) \exp(-iqa).$$

Using the latter equations we can eliminate coefficients $C$, $D$ and express $E$, $F$ only with $A$ and $B$. This leads to the following structure of the transfer matrix

$$\mathcal{M} = \begin{pmatrix} \mathcal{M}_{11}\sigma_0 & \mathcal{M}_{12}\sigma_3 \\ -\mathcal{M}_{12}\sigma_3 & \mathcal{M}_{11}^\star\sigma_0 \end{pmatrix}, \tag{3.8}$$

which has non-zero entries

$$\mathcal{M}_{11} = \frac{iE}{\sqrt{E^2 - m^2}} \sin{(qd)} + \cos{(qd)} \tag{3.9}$$

$$\mathcal{M}_{12} = -\frac{im}{\sqrt{E^2 - m^2}} \sin{(qd)} \tag{3.10}$$

with $d = b - a$. The matrix $\mathcal{M}$ contains all information an the scattering process at the barrier. Due to the spinor structure of the Dirac equation the transfer matrix is $4 \times 4$ instead of $2 \times 2$ in the Schrödinger case. It is worth mentioning for later discussions that in the absence of the barrier ($m = 0$) the transfer matrix is diagonal with entries $\mathcal{M}_{11} = \exp(ikx)$. Comparing equation (3.8) with equation (3.5) we can directly obtain the transmission coefficient

$$|t|^2 = \frac{1}{|\mathcal{M}_{11}|^2} = \left( \frac{E^2}{E^2 - m^2} \sin^2{(qd)} + \cos^2{(qd)} \right)^{-1} \tag{3.11}$$

which is shown in figure 3.2 and 3.3. In region II the wave is decaying like $\psi \approx \exp(-md)$. If the barrier width is small compared to its hight $m$, the fermion can tunnel through the barrier. This can be seen by comparing to the red curve, where $|t|^2 > 0$ for energies smaller than the gap width. As the mass barrier gets wider transmission is only possible for energies larger than the gap.
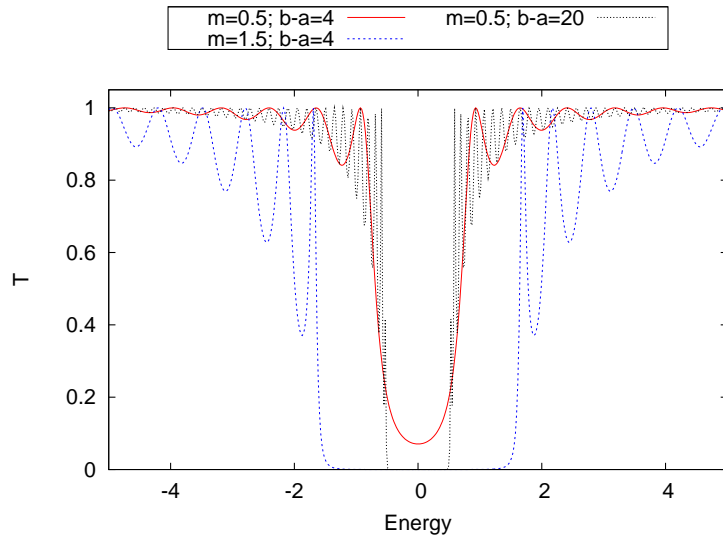


**Figure 3.2.:** Transmission coefficient for a Dirac fermion scattering at a massive barrier.

Now that we have derived a transfer matrix describing a single barrier we can generalize easily to the case of $N$ identical scatterers, which brings us to the next section.
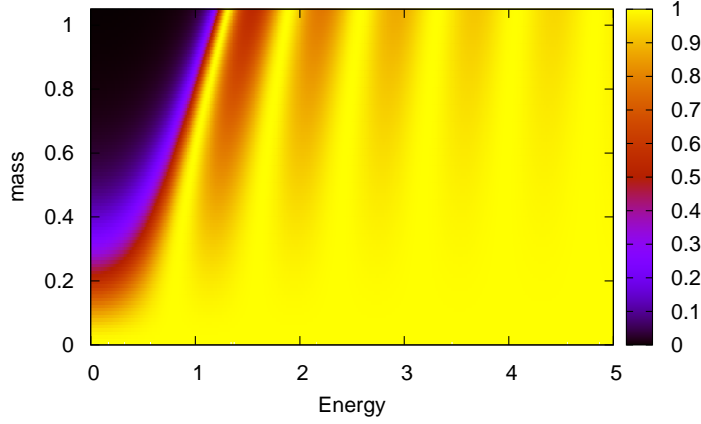
**Figure 3.3.:** Density plot of the transmission coefficient (3.11) for $d = 4$

## 3.1.2. Transmission through $N$ identical barriers

We already mentioned one big benefit of the transfer matrix formalism: Once we know the matrix for one barrier, we can simply multiply the matrices and thus connect an arbitrary number of scatterers. If we link $N$ identical barriers it turns out that the only change is that the width of the barrier $d$ is multiplied by $N$, as we would expect. Therefore, we should investigate a more interesting case.

Let us assume the situation where we put a region of length $l$ with $m = 0$ between each barrier of same width similar to the Kronig-Penny model. This can be described by the matrix

$$\tilde{\mathcal{M}} = \begin{pmatrix} \exp(ikl)\sigma_0 & 0 \\ 0 & \exp(-ikl)\sigma_0 \end{pmatrix} \begin{pmatrix} \mathcal{M}_{11}\sigma_0 & \mathcal{M}_{12}\sigma_3 \\ -\mathcal{M}_{12}\sigma_3 & \mathcal{M}_{11}^\star\sigma_0 \end{pmatrix}$$
$$= \begin{pmatrix} \tilde{\mathcal{M}}_{11}\,\sigma_0 & \tilde{\mathcal{M}}_{12}\,\sigma_3 \\ \tilde{\mathcal{M}}_{12}^\star\,\sigma_3 & \tilde{\mathcal{M}}_{11}^\star\,\sigma_0 \end{pmatrix}. \tag{3.12}$$

Since we want to consider $N$ barriers we have to evaluate

$$\tilde{\mathcal{M}}^N = U \operatorname{diag}(\lambda_1, \lambda_2, \lambda_3, \lambda_4)^N\ U^{-1} \tag{3.13}$$

with

$$U^{-1}\,\tilde{\mathcal{M}}U = \operatorname{diag}(\lambda_1, \lambda_2, \lambda_3, \lambda_4). \tag{3.14}$$

Thus we need to calculate the eigenvalues $\lambda_i$ and the transformation matrices $U$.

For this reason it is convenient to abbreviate the entries of $\tilde{\mathcal{M}}$ as

$$\tilde{\mathcal{M}}_{11} = A + iB$$

$$A = \cos(qd)\cos(kl) - \frac{E}{\sqrt{E^2 - m^2}}\sin(qd)\sin(kl) \tag{3.15}$$

$$B = \cos(qd)\sin(kl) + \frac{E}{\sqrt{E^2 - m^2}}\sin(qd)\cos(kl) \tag{3.16}$$

and

$$\tilde{\mathcal{M}}_{12} = W - iC$$

$$W = \frac{m}{\sqrt{E^2 - m^2}}\sin(qd)\sin(kl) \tag{3.17}$$

$$C = \frac{m}{\sqrt{E^2 - m^2}}\sin(qd)\cos(kl)\,. \tag{3.18}$$

The eigenvalues are then given by

$$\lambda = A \pm \sqrt{C^2 - B^2 + W^2} = A \pm \alpha \tag{3.19}$$

and the corresponding transformation matrix

$$U = \begin{pmatrix} \frac{B-i\alpha}{C-iW} & 0 & \frac{B+i\alpha}{C-iW} & 0 \\ 0 & -\frac{B-i\alpha}{C+iW} & 0 & -\frac{B+i\alpha}{C+iW} \\ 1 & 0 & 1 & 0 \\ 0 & 1 & 0 & 1 \end{pmatrix}. \tag{3.20}$$

We can now work out expression (3.13) which gives

$$\tilde{\mathcal{M}}^N = \begin{pmatrix} D-G & 0 & F & 0 \\ 0 & D-G & 0 & -F^\star \\ -F^\star & 0 & D+G & 0 \\ 0 & F & 0 & D+G \end{pmatrix}, \tag{3.21}$$

where we have used

$$D = \cos(qdN) \tag{3.22}$$

$$G = \frac{B}{\sqrt{C^2 - B^2 + W^2}}\sin(qdN) \tag{3.23}$$

$$F = \frac{C+iW}{\sqrt{C^2 - B^2 + W^2}}\sin(qdN)\,. \tag{3.24}$$

Finally, the transmission coefficient is given by

$$|t|^2 = |D + G|^{-2}\,. \tag{3.25}$$

The resulting expression for the transmission coefficient is rather lengthy and therefore we will not reinsert the abbreviations but plot the result directly in figure 3.4. Here we have chosen the width of each barrier and the distance between them to be equal. The first property that can be seen is that a particle can pass the barriers for energies about half of the gap. This is because each single barrier is narrow compared to $m$, thus, the particle can tunnel through it. If we increase the width of a barrier the situation gets different, shown in figure 3.5, where tunneling for $E < m$ is suppressed.
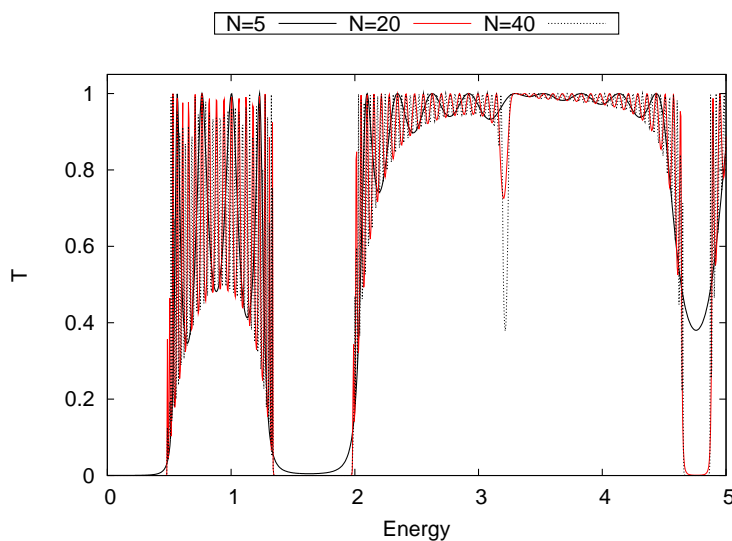


**Figure 3.4.:** Transmission through identical barriers with equal distances $l = 1$ and widths $d = 1$.

### 3.1.3. Transmission through a scalar potential barrier

Let us now consider the case of a massless fermion in one dimension scattering at a scalar potential of width $d$, which is described by

$$(-i\hbar v_F\,\sigma_1\,\partial_x + (V_0 - E)\,\sigma_0)\,\psi(x) = 0\,. \tag{3.26}$$

Adapting the calculation of section 3.1 to the latter equation leads to the transfer matrix

$$\mathcal{M} = \begin{pmatrix} \mathcal{M}_{11}\sigma_0 & 0 \\ 0 & \mathcal{M}_{11}^\star\sigma_0 \end{pmatrix} \tag{3.27}$$

with non-zero entry

$$\mathcal{M}_{11} = \exp\left[-id(V_0 - E)\right]\,. \tag{3.28}$$
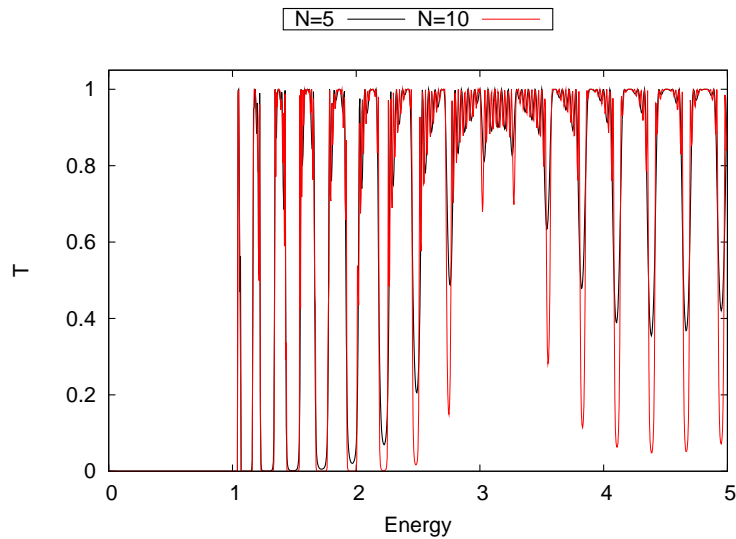
**Figure 3.5.:** Transmission through identical barriers with equal distances $l = 1$ and widths $d = 10$ for $m = 1$.

Since the resulting transfer matrix contains only phase factors in the diagonal, it is clear that the transmission coefficient, given by $|t|^2 = |\mathcal{M}_{11}|^{-2}$ is always one. In other words, the fermion is not scattered at a scalar potential barrier. This behavior is known as Klein tunneling named after Oskar Klein, who solved this problem for electrons in 1928 [53]. On the first sight this result is strongly counter intuitive, but the physical explanation does not seem so farfetched: When the particle hits the barrier, for example as an electron, it turns into an positron inside the potential barrier and finally leaves it again as an electron. This is possible since the Dirac equation simultaneously describes a particle and its anti-particle.

It soon has been noticed that the so called Klein paradox could be tested experimentally using graphene samples [54]. In this work the transmission coefficient consequently is angle dependent since graphene is two dimensional, but can be compared for particles hitting the barrier perpendicular. Indeed, particles in monolayer graphene can pass a potential barrier when moving perpendicular to the barrier [55, 56]. For more publications on Klein tunneling in graphene, we refer to Ref. [57] for further reading.

# 4. Lyapunov exponent and localization length

This chapter is intended to provide the background and method needed for later calculations and follows mainly Ref. [58]. We previously have introduced the transmission coefficient as a quantity that can be calculated by means of a transfer matrix. In this chapter we are going to introduce an additional quantity, namely the Lyapunov characteristic exponent (LCE) or just Lyapunov exponent (LE). They are a very useful tool for studying metal-insulator transitions and are mostly encountered with random matrices. Since the main interest in this thesis is to perform finite-size scaling for lattice fermions and to study their metal-insulator transitions, Lyapunov exponents are a welcome candidate to deal with.

## 4.1. Definition and properties

Whenever random numbers are involved, limit theorems come into play. Just think of the central limit theorem for independent and identically distributed random variables, which tend to be normal distributed for large numbers. One question arises: Is there also a limit theorem if we deal with random matrices? The answer is: Yes.

An introduction to random matrix theory can be found in textbooks [58, 59]. The multiplicative ergodic theorem of Oseledec [60] is a limit theorem for a product of random matrices. A more detailed discussion can be found in Ref. [61]. For a sequence of matrices, where the logarithm of the norm is finite ( $\langle \ln \|T\| \rangle < \infty$ ), there exists a limiting matrix $\Gamma$

$$\lim_{L \to \infty} (\mathcal{M}_L^\dagger \mathcal{M}_L)^{1/2L} = \Gamma \tag{4.1}$$

with

$$\mathcal{M}_L = \prod_{i=1}^{L} T_i \,, \tag{4.2}$$

where $T_i$ is the transfer matrix of one step.

The eigenvalues of $\Gamma$ are usually written as $\exp(\gamma_i)$ defining $\gamma_i$, which are called Lyapunov exponents and are real and positive. When the sequence of matrices is

ergodic the Lyapunov spectrum is independent of the particular sequence, thus, the Lyapunov exponents are global properties of the random matrix product. If one knows the eigenvalues, one also knows that there is a set of orthonormal eigenvectors called Lyapunov basis $\vec{v}_i$, which allows to write

$$\gamma_i = \lim_{n\to\infty} \frac{1}{n} \ln |\mathcal{M}_n\,\vec{v}_i|\,. \tag{4.3}$$

This implies the existence of subspaces where the growth rate might be slower. For this reason it is not sufficient to calculate only the maximum Lyapunov exponent in a system with dimensionality higher than one. It is important to keep in mind that the eigenvectors are in general not the eigenvectors of $\mathcal{M}_n$ but of $\mathcal{M}_n^\dagger \mathcal{M}_n$ because

$$|\mathcal{M}_n\,\vec{z}|^2 = \langle \vec{z}|\mathcal{M}_n^\dagger \mathcal{M}_n|\vec{z}\rangle\,. \tag{4.4}$$

Another important point is that the Lyapunov basis depends on the certain sequence of matrices and therefore is only a local property in contrast to the Lyapunov spectrum.

## 4.1.1. Identical non-random matrices

Let us now define a new set of stability exponents (cf. Ref. [58]). Let $\beta_i$ be the eigenvalues of $\mathcal{M}_n$ then

$$\alpha_i = \lim_{n\to\infty} \frac{1}{n} \ln\langle \beta_i\rangle \quad \alpha_i \in \mathbb{C}\,. \tag{4.5}$$

If we are able to write $\mathcal{M}_n$ in diagonal form, the Lyapunov exponents are the real part of $\alpha_i$

$$\Re(\alpha_i) = \gamma_i\,, \tag{4.6}$$

which is in our case helpful to compare between clean and disordered case. In a system where disorder is absent all transfer matrices are equal. This allows us to write

$$\mathcal{M} = \prod_{i=1}^{N} T_i = T \times T \times ... \times T = T^N\,. \tag{4.7}$$

Next we can use

$$diag(T) = \Lambda = U^{-1}\,T\,U \quad \Rightarrow \quad T = U\,\Lambda\,U^{-1}, \tag{4.8}$$

which leads to

$$T^N = U\,\Lambda\,U^{-1}\,U\,\Lambda\,U^{-1}...U\,\Lambda\,U^{-1} = \Lambda^N\,. \tag{4.9}$$

As a consequence only eigenvalues of a single transfer matrix have to be calculated. If we denote the eigenvalues of the transfer matrix as $\tau_i$, we get

$$\alpha_i = \lim_{N\to\infty} \frac{1}{N} \ln(\beta_i) = \lim_{N\to\infty} \frac{1}{N} \ln(\tau_i^N) = \ln(\tau_i) \qquad (4.10)$$

and finally

$$\gamma_i = \Re(\ln(\tau_i)) \,, \qquad (4.11)$$

which is independent of the number of multiplications. If we recall the transfer matrix for one dimensional Dirac fermions from the previous chapter, it is clear that the wave number is given by

$$k_i = \Im(\ln(\tau_i)) \,. \qquad (4.12)$$

The condition for the existence of an extended state is $\gamma_i = 0$. With the latter relations we are able to compare the numerical results with analytical results for clean systems. In general there is no equivalent theorem for $\alpha_i$ like the Oseledec theorem. Furthermore, for a product of random matrices the real part of $\alpha_i$ can differ from the corresponding Lyapunov exponent.

## 4.2. Numerical algorithm

In principle we could write a code, which computes the product of an arbitrary number of random matrices, multiplies the result by its adjoint and then calculates the eigenvalues to obtain the Lyapunov exponents in the end. Since computer power and memory is limited one can imagine that numbers will be soon out of range. In practice, it is not possible to get even close to $10^3$ multiplications. A solution to this problem is an algorithm that Pichard [5] and MacKinnon et al. [9] introduced to the field of metal-insulator transitions. There are also former works using the same method [6] in a different context.

During the iterative procedure described in Ref. [9], the product of a couple of matrices has to be orthonormalized using the Gram-Schmidt process. The best result is obtained when the latter is performed after each step of multiplication. The benefit of increasing the number of multiplications is only a speed up in calculations. This method allows to calculate the whole Lyapunov spectrum. The smallest Lyapunov exponent is identified with the inverse localization length [5, 7] and we define

$$\min\{|\gamma_i|\} = \gamma_{min} = \Lambda^{-1} \,. \qquad (4.13)$$

For the infinite system the localization length is denoted by $\xi$ and determines the exponential decay of the wave functions envelope

$$|\psi(\mathbf{r})| \propto \exp\left(-\frac{|\mathbf{r}|}{\xi}\right) \,. \qquad (4.14)$$

Calculating the Lyapunov spectrum by means of the Gram-Schmidt process is equivalent to an consecutive $QR$ factorization, where $Q$ is an orthogonal- and $R$ an upper triangular matrix. For our further calculations we choose $QR$ factorization instead of the Gram-Schmidt process. The reason is that we use a numerical library, which provides a fast $QR$ factorization.

The algorithm for the calculation of the Lyapunov exponents with $QR$ factorizations works as follows: Start with the product $T_n T_{n-1} \times ... \times T_2 T_1$ of random matrices. Set $B_1 = T_1$ and factorize $B_1 = Q_1 R_1$ using $QR$ factorization. Replace the latter in the product $T_n T_{n-1} \times ... \times (T_2 Q_1) R_1$. Then store $\gamma_k^{(1)} = \ln |R_1(k, k)|$, replace $T_2 Q_1 = B_2$ and factorize again $B_2 = Q_2 R_2$. The logarithm of all diagonal entries is stored iteratively $\gamma_k^{(2)} = \gamma_k^{(1)} + \ln |R_2(k, k)|$. By setting $B_i = Q_{i+1} R_{i+1}$ the procedure can be repeated $(n-1)$-times, which gives finally $Q_n(R_n R_{n-1} \times ... \times R_2 R_1) = Q_n R$.

The diagonal entries of $R$ converge to the eigenvalues of $\Gamma$ and the Lyapunov exponents are given by

$$\gamma_k = \frac{1}{n} \sum_{i=1}^{n} \ln |R_i(k, k)| \ . \tag{4.15}$$

Factorization after each step of multiplication leads to the highest accuracy. We have controlled the precision by calculating the sum of all Lyapunov exponents, which should be zero and is $\approx 10^{-15}$ in our case. Increasing the multiplications between each $QR$ factorization increases also the sum of $\gamma_k$. The convergence of the Lyapunov exponents has been controlled by storing the last $\approx 10^4$ and calculating mean and variance. After reaching the desired error limit the multiplication of transfer matrices has been stopped.

For our calculations we have used random number generators provided by a numerical library, and the corresponding probability density functions can be taken from appendix A.

# 5. Finite-size scaling

The algorithm provided in the previous sections allows to calculate $\Lambda$ as a function of system size $M$, and of disorder $W$. Since computational performance and computer memory are both limited, numerical simulations are restricted to finite systems and results have to be extrapolated to infinite ones. This can be achieved by studying the size dependence of the localization length and more precisely by finite-size scaling. In the following we like to introduce a scaling theory for the localization length, which allows to make statements on infinite systems. Usually the localization length normalized by strip width [7, 8, 9, 10, 62]

$$\tilde{\Lambda} = \frac{\Lambda}{M} \tag{5.1}$$

or equivalently the normalized Lyapunov exponent [63]

$$z = \frac{M}{\Lambda} = M\,\gamma_{min}. \tag{5.2}$$

is discussed in this context. Assuming that the considered system is metallic, it is clear that the localization length must grow faster than the strip width, thus diverge. When the system is in the localized phase the normalized localization length has to converge to zero consequently, when increasing the system width. Especially in the two dimensional case it is sometimes favorable to consider $\Lambda$ unnormalized. According to [5] this allows us to distinguish between two different kinds of divergences. If $\Lambda$ increases with system size $M$, it may grow faster than $M$, which corresponds to an extended state or it may grow linear with $M$. Usually the linear growth is interpreted as critical behavior, but the localization length may also grow slower than $M$ in an intermediate regime [12]. At least there exists no argument against it, for the best of our knowledge. In both cases $\Lambda$ will diverge, and diffusion in two dimensions can not be ruled out for states decaying with a power law (cf. Appendix in Ref. [64]). States are only exponentially localized if $\Lambda$ converges towards a finite limit. This behavior of $\Lambda$ for $M \to \infty$ can be summarized as

$$\Lambda(W) \propto M^{\alpha}. \tag{5.3}$$

States are extended for $\alpha > 1$, decaying for $0 < \alpha < 1$, critical for $\alpha = 1$. Only if $\alpha = 0$ states are exponentially localized. According to [7] the normalized

localization length $\tilde{\Lambda}$ obeys a scaling theory such that

$$\frac{d \ln \tilde{\Lambda}}{d \ln M} = \chi(\ln \tilde{\Lambda}), \tag{5.4}$$

where $\chi$ is an unknown function with solutions of the form

$$\tilde{\Lambda}(M, W) = f(\xi(W)/M). \tag{5.5}$$

Here $\xi$ is a characteristic length of the system. The scaling theory states that $\tilde{\Lambda}$ is not depending on $M$ and $W$ separately. Any change of disorder can be compensated by a change of the length scale, i.e. system size. The scaling theory presented here is based on ideas of [4, 65, 66] and was applied to the localization length in [5, 9]. Having calculated $\xi$, it should be possible to rescale all data onto a single curve. Let us illustrate two methods to calculate $\xi$.

A scale invariant point, where $\tilde{\Lambda}$ is independent of $M$, indicates a metal-insulator transition. From its behavior in vicinity of such a point it is possible to calculate the critical exponent $\nu$ of the correlation length [9]. The length $\xi$ can then be identified with the localization length of a infinite system. All critical quantities can be obtained by Taylor expansion

$$\ln \tilde{\Lambda} = \ln \tilde{\Lambda}_c + \sum_{s=1}^{S} A_s \left( |W - W_c| M^{1/\nu} \right)^s \tag{5.6}$$

$$= \ln \tilde{\Lambda}_c + \sum_{s=1}^{S} A_s \left( \frac{\xi}{M} \right)^{-s/\nu} \tag{5.7}$$

with $\xi = |W - W_c|^{-\nu}$. Comparing the latter with equation (5.5), the scaling function $\xi$ can be interpreted as the characteristic length scale. This means that we have extrapolated the localization length of a infinite system by finite-size scaling.

In addition, there might be results which do not exhibit a critical point. In that case, there is a second method to perform finite-size scaling. After calculating the localization lengths of different strip widths and for different disorder strengths, we arrive at a set of curves. For each disorder strength there is a corresponding curve. Furthermore, we consider the data on a logarithmic scale. In general there are several combinations of strip width $M$ and disorder $W$ leading to the same localization length. If the scaling argument holds, it should be possible to find a function $\xi(W)$ which maps all data points onto a single curve [7, 9]. For this reason we have to minimize the variance of $\ln M - \ln \xi$ for each localization length

$$S = \sum_i \left\{ \frac{1}{N_i} \sum_j [\ln M_{ij} - \ln \xi(W_j)]^2 - \left[ \frac{1}{N_i} \sum_j (\ln M_{ij} - \ln \xi(W_j)) \right]^2 \right\} \tag{5.8}$$

to obtain the scaling function. Index $j$ labels different disorder strengths and $i$ corresponds to the number of certain localization lengths which share the same value and intersect with different curves of disorder. The total number of these localization lengths is given by $N_i$. Equating the partial derivatives to zero

$$\frac{\partial S}{\partial \xi(W_k)} = 0$$

$$= \sum_i \left\{ -\frac{2}{N_i} \sum_j \left[ \ln M_{ij} - \ln \xi(W_j) \right] \delta_{jk} + \frac{2}{N_i^2} \left[ \sum_j (\ln M_{ij} - \ln \xi(W_j)) \right] \right\}$$

$$= \sum_{i,j} \left\{ -\frac{2}{N_i} \ln(M_{ij}) \delta_{jk} + \frac{2}{N_i} \ln \xi(W_j) \delta_{jk} + \frac{2}{N_i^2} \ln(M_{ij}) - \frac{2}{N_i^2} \ln \xi(W_j) \right\}$$

leads to a set of equations

$$\Rightarrow \sum_{i,j} \left( \frac{1}{N_i^2} - \frac{\delta_{jk}}{N_i} \right) \ln(M_{ij}) = \sum_{i,j} \left( \frac{1}{N_i^2} - \frac{\delta_{jk}}{N_i} \right) \ln \xi(W_j) \qquad (5.9)$$

that allow to compute $\xi$.

Solving the system of equations (5.9) is equivalent to calculate the average of distances between curves of different disorder. The result gives the number which is needed to shift the curves relatively to each other. Since the position of the resulting curve is irrelevant, it is convenient to shift all curves onto the lowest one, i.e. that for biggest disorder [9]. In order to get the needed values of $\ln M_{ij}$ for a single $\tilde{\Lambda}$ with different disorders, it may be necessary to interpolate between calculated values. This can be done by fitting a polynomial to $\ln[\Lambda(M)]$.

In order to illustrate that, in this case, one-parameter scaling results in shifting curves by its distance, we solve equation (5.8) for three curves and four points as an example. The latter expression gets

$$S = \frac{1}{2} \left( (A - x_2)^2 + (B - x_1)^2 + (C - x_3)^2 + (D - x_2)^2 \right)$$

$$- \frac{1}{4} \left[ (A - x_2) + (B - x_1) \right]^2 + \left[ (C - x_3) + (D - x_2) \right]^2 ,$$

where we have used the abbreviations $A = \ln M_{12}$, $B = \ln M_{11}$, $C = \ln M_{23}$, $D = \ln M_{22}$ and $x_j = \ln \xi(W_j)$. The three equations we solve are given by

$$\frac{dS}{dx_1} \Rightarrow x_1 - x_2 + A - B = 0 \qquad (5.10)$$

$$\frac{dS}{dx_2} \Rightarrow x_1 - 2x_2 + x_3 + A - B - D = 0 \qquad (5.11)$$

$$\frac{dS}{dx_3} \Rightarrow x_2 - x_3 + C - D = 0 . \qquad (5.12)$$

If we assume leaving the curve for the biggest disorder unshifted, this leads to $x_3 = 0$. From equation (5.12) it follows that

$$x_2 = D - C\,,\tag{5.13}$$

which is exactly the distance between the third and second curve. Inserting this result into (5.10), we get

$$x_1 = B - A + C - D\,.\tag{5.14}$$

Now it is obvious, that one has only to calculate the average of distances between all curves. This gives the correct value for the scaling parameter $\ln \xi(W)$.

# 6. Dirac equation on a lattice

We have seen in chapter 2, that electrons in graphene can be treated within the tight-binding approximation. In the low-energy regime around one nodal point the spectrum of such an electron is linear. It can be modeled using the two dimensional Dirac equation, known from relativistic quantum mechanics.

In this chapter we like to give the basis to treat the problem of disordered Dirac fermions numerically. For this reason we derive a discrete version of the Dirac equation in one and two spatial dimensions and construct transfer matrices which we subsequently use for calculations of the Lyapunov characteristic exponents. Whenever possible we compare our numerical to analytical results or numerical results from different methods.

We also recall briefly a second model for comparison, that describes Dirac fermions on a lattice introduced in Ref. [67] and used for similar calculations.

## 6.1. Discretization in one dimension

In order to begin with the simplest possible model, we start with discretization in one dimension. The time independent Dirac equation for a free particle can be written as

$$H\psi(x) = E\psi(x) \,, \tag{6.1}$$

where the wave functions $\psi(x)$ are spinors and the Hamiltonian is given by

$$H = -(i\hbar v_F)\,\sigma_1\,\partial_x \,, \tag{6.2}$$

with a characteristic velocity $v_F$ corresponding to the speed of light in the relativistic case. If we call $\hbar v_F = \alpha$ and write the Dirac equation in momentum space

$$\alpha \begin{pmatrix} 0 & k_x \\ k_x & 0 \end{pmatrix} \psi(x) = E\,\psi(x), \tag{6.3}$$

we immediately obtain the energy dispersion

$$E(k_x) = \pm\alpha\,k_x \,, \tag{6.4}$$

describing a free massless relativistic particle in one dimension. To ensure Hamiltonian (6.2) remains hermitian we have chosen a symmetric discretization of the

differential operator

$$\partial_x \psi(x) \approx \frac{1}{2\Delta}(\psi_{x+\Delta} - \psi_{x-\Delta}) \,. \tag{6.5}$$

Thus, the Dirac equation gets

$$\Rightarrow -\frac{i\alpha}{2\Delta}\sigma_1(\psi_{x+\Delta} - \psi_{x-\Delta}) = E \,\sigma_0 \psi(x) \,. \tag{6.6}$$

The energy dispersion for discretized Hamiltonian can be calculated using Fourier transformation

$$\int dk \,\, \tilde{\psi}(k_x) \begin{pmatrix} -E & \frac{\alpha}{\Delta}\sin(\Delta k_x) \\ \frac{\alpha}{\Delta}\sin(\Delta k_x) & -E \end{pmatrix} e^{ik_x x} = 0 \,. \tag{6.7}$$

Since the real space is now discrete we can think of $\Delta$ as a lattice constant. In the following we set $\Delta$ and $\alpha$ to unity for simplicity. The energy dispersion for lattice fermions in one dimension is then given by

$$E(k_x) = \pm \sin(k_x) \,. \tag{6.8}$$

The dispersion has nodal points at in the center of the Brillouin zone ($k_x = 0$) and at the border ($k_x = \pm\pi$). The outer two only contribute with $1/2$, which gives two Dirac cones in total.

As a surprising result of discretization, a single fermion gets doubled. This is called fermion doubling or species multiplication and was already observed in the late 1970ies [68, 69]. Solutions to this problem were also given by the same authors.

Following Ref. [70] we introduce a lattice operator $\hat{B}_1$ and label the lattice points with integer numbers $l$

$$\hat{B}_1 \psi_l = \frac{1}{2}\left\{ \psi_{l+1} + \psi_{l-1} \right\} \,. \tag{6.9}$$

The operator $\hat{B}_1$ breaks up the cones at the borders of the Brillouin zone. We obtain the new Hamiltonian by transforming the old one as

$$H \rightarrow H + \delta(\hat{B}_1 - 1)\sigma_3 \,, \tag{6.10}$$

with the corresponding energy dispersion

$$E = \pm\sqrt{sin(k_x)^2 + (\delta(cos(k_x) - 1))^2} \,. \tag{6.11}$$

The lattice operator allows us to tune the gap of the outer nodal points via the parameter $\delta$, while $m$ acts on both neutrality points. Opening a gap at one Dirac point breaks the symmetry between the two cones or valleys, for this reason we call the situation where $\delta \neq 0$, broken valley symmetry. For $\delta = 2m$ the outer gap closes again and massless fermions reappear at the border of the Brillouin zone.

Different potentials can be included easily in (6.10) which have corresponding energy dispersions

$$H \rightarrow H + m(l)\sigma_3 \qquad\qquad \text{mass}$$

$$E = \pm\sqrt{sin(k_x)^2 + (m + \delta(cos(k_x) - 1))^2} \qquad\qquad (6.12)$$

$$H \rightarrow H + U(l)\sigma_0 \qquad\qquad \text{scalar potential}$$

$$E = U \pm \sqrt{sin(k_x)^2 + (\delta(cos(k_x) - 1))^2} \qquad\qquad (6.13)$$

$$H \rightarrow H + V_1(l)\sigma_1 \qquad\qquad \text{vector potential}$$

$$E = \pm\sqrt{(sin(k_x) + V_1)^2 + (\delta(cos(k_x) - 1))^2} \,. \qquad\qquad (6.14)$$

## 6.1.1. Recurrence equation

Before we derive a transfer matrix for one dimensional lattice fermions, we like to introduce recurrence equations to calculate Lyapunov exponents. This can be done only in the one dimensional case without valley symmetry breaking ($\delta = 0$). The recurrence equation method can then serve as a testing ground and results can be compared with those obtained from the transfer matrix method.

### Random mass and scalar potential

For random mass and scalar potential the recurrence equations can be derived simultaneously. We set the energy to zero and write for the Dirac equation

$$\begin{pmatrix} a & -i\partial_x \\ -i\partial_x & b \end{pmatrix} \begin{pmatrix} u(x) \\ v(x) \end{pmatrix} = 0 \,. \qquad\qquad (6.15)$$

The coefficients $a$ and $b$ can be replaced by random mass or scalar potential in the end. After discretization we get two equations which couple both spinor components

$$a_l \, u_l = \frac{i}{2}\{v_{l+1} - v_{l-1}\} \qquad\qquad (6.16)$$

$$b_l \, v_l = \frac{i}{2}\{u_{l+1} - u_{l-1}\} \,. \qquad\qquad (6.17)$$

One spinor component can be eliminated by shifting the index in the first equation

$$u_{l+1} = \frac{i}{2a_{l+1}}\{v_{l+2} - v_l\} \qquad\qquad (6.18)$$

$$u_{l-1} = \frac{i}{2a_{l-1}}\{v_l - v_{l-2}\} \qquad\qquad (6.19)$$

and we are left with one equation

$$v_l = \frac{i}{2b_l} \left\{ \frac{i}{2a_{l+1}}(v_{l+2} - v_l) - \frac{i}{2a_{l-1}}(v_l - v_{l-2}) \right\} . \tag{6.20}$$

Rearranging leads to

$$\frac{v_{l+2}}{4b_l a_{l+1}} = -\frac{v_{l-2}}{4b_l a_{l-1}} + \left\{ \frac{1}{4b_l a_{l+1}} + \frac{1}{4b_l a_{l-1}} - 1 \right\} v_l \tag{6.21}$$

$$\frac{v_{l+2}}{v_l} = -\frac{v_{l-2}}{v_l}\frac{a_{l+1}}{a_{l-1}} + \left\{ 1 + \frac{a_{l+1}}{a_{l-1}} - 4b_l a_{l+1} \right\} . \tag{6.22}$$

Now we define $z_{l+2} = v_{l+2}/v_l$ and get finally

$$z_{l+2} = a_{l+1} \left\{ \frac{1}{a_{l+1}} - 4b_l + \frac{1}{a_{l-1}}(1 - z_l^{-1}) \right\} \tag{6.23}$$

for the recurrence equation. The $a_l$ are random numbers and correspond to random mass for $b_l = -a_l = m_l$ and to random scalar potential for $a_l = b_l = U_l$. According to Ref. [71] the Lyapunov exponent can be defined as

$$\gamma = \lim_{n \to \infty} \frac{1}{2n} \sum_{l=1}^{n} \langle \ln |z_l| \rangle . \tag{6.24}$$

In a clean system $a_l$ and $b_l$ are non-random and the Lyapunov exponent can be calculated solving a quadratic equation

$$z^2 - (2 - 4ab)z + 1 = 0 \Rightarrow z_{1,2} = 1 - 2ab \pm \sqrt{ab(ab - 1)}$$

$$\text{random mass :} \qquad z_{1,2} = 1 + 2m^2 \pm \sqrt{m^2 + m} \tag{6.25}$$

$$\text{scalar potential :} \qquad z_{1,2} = 1 - 2U^2 \pm \sqrt{U^2 - U} . \tag{6.26}$$

This yields

$$\gamma = \frac{1}{2} \ln |z| , \tag{6.27}$$

thus, in the clean limit, $\gamma$ should acquire the values $\gamma \approx 0.4812$ for random mass and $\gamma = 0$ for scalar potential.

Using the recurrence equation (6.23) and the definition (6.24) we can directly calculate the Lyapunov exponents for the introduced random potentials and several probability distributions.

The random numbers have been generated by a distribution generator for gaussian- and cauchy distributed random numbers. Then the Lyapunov exponent has been

calculated for various widths of the corresponding distribution, which can be seen as the disorder strength. Calculations have been performed with *Mathematica* for chains of length $n = 4000$ and an average over 10 realizations. We denote the expectation value of a random number $x$ by $\langle x \rangle$ or $\bar{x}$ equivalently.

Results for random mass are presented in figure 6.1. The plot shows the Lyapunov exponent as a function of disorder strength, with $\bar{m}$ being the expectation value. Since the Lyapunov exponent is only zero for zero disorder and elsewhere growing, we conclude that Dirac fermions are always localized by disorder. Only for gaussian disorder and $\bar{m} \neq 0$ there is a small dip where the Lyapunov exponent has a local minimum but $\gamma = 0$ is never reached.
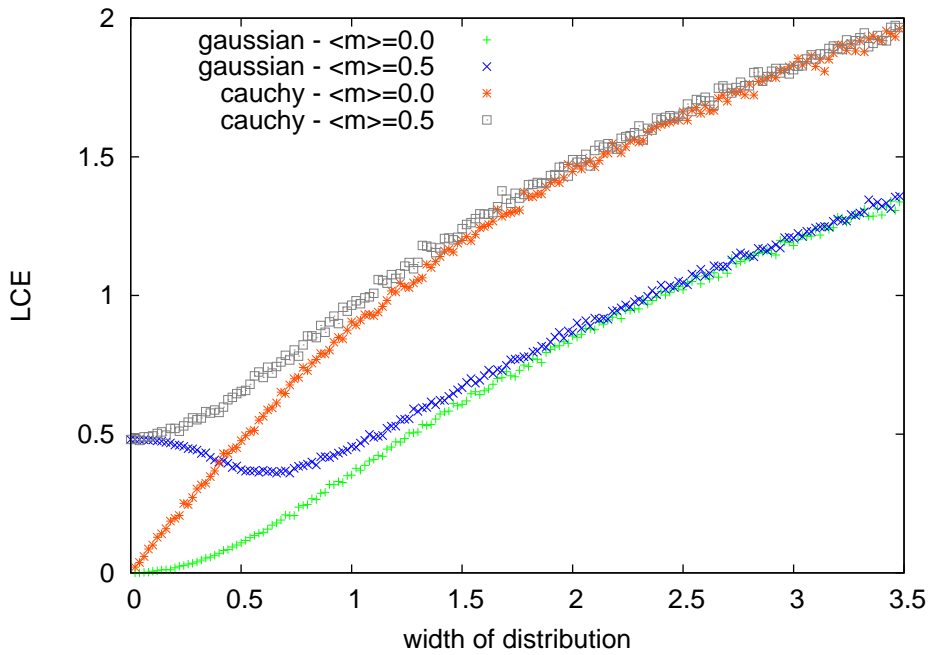


**Figure 6.1.:** Comparison of the Lyapunov exponent for different disorder types with random mass in a one dimensional chain of Dirac fermions.

**Random vector potential**

For random vector potential the Dirac equation reads

$$\begin{pmatrix} 0 & -i\partial_x + V \\ -i\partial_x + V & 0 \end{pmatrix} \begin{pmatrix} u(x) \\ v(x) \end{pmatrix} = 0 \,. \tag{6.28}$$

Both equations do not couple and we write directly

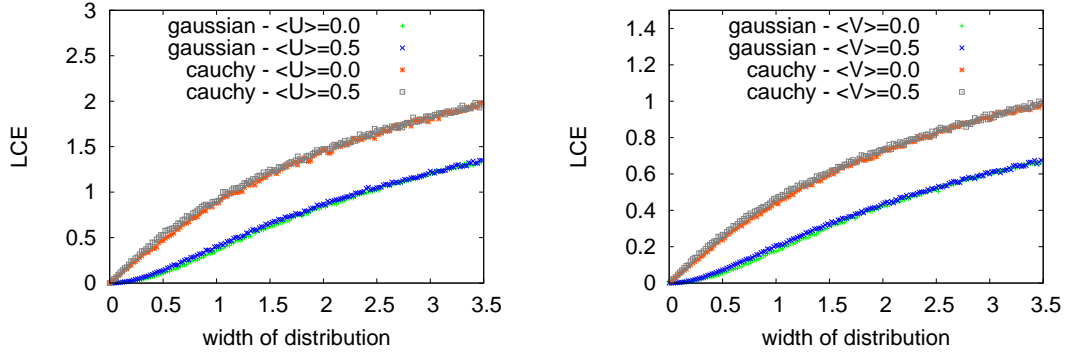$$z_{l+1} = -2iV_l + \frac{1}{z_l} \tag{6.29}$$

**Figure 6.2.:** Lyapunov exponents as function of disorder strength for different disorder types of Dirac fermions in one dimensions. Left: Scalar potential and right: Random vector potential.

for each spinor. The results are plotted in figure 6.2. As we could have expected from the energy dispersion the Lyapunov exponent is zero in the clean limit.

For all three disorder types results show similar behavior: As disorder increases Lyapunov exponents are always growing. Except for random mass with finite mean, we see $\gamma \neq 0$ for vanishing disorder, arising from the gap in the spectrum. In the next section we proceed and derive a transfer matrix for the introduced discretization. By means of the transfer matrix method we should then be able to reproduce the results from this section.

## 6.1.2. Constructing the transfer matrix

Whereas the recurrence equation could only be used to calculate Lyapunov exponents of the one dimensional Dirac equation without valley symmetry breaking, it is possible to derive a transfer matrix for a more general case.

We start with equation (6.10) including a random mass term and write the discretized Dirac equation as

$$E\,\sigma_0\psi_l = \frac{1}{2}(-\sigma_1\psi_{l+1} + \sigma_1\psi_{l-1}) + \frac{\delta}{2}(\sigma_3\psi_{l+1} + \sigma_3\psi_{l-1}) + (\delta - m_l)\sigma_3\psi_l\,.$$

Rearranging gives

$$\Rightarrow \psi_{l+l} = 2S^{-1}\left[E\sigma_0 + (\delta - m_l)\sigma_3\right]\psi_l - S^{-1}\left[i\sigma_1 + \delta\sigma_3\right]\psi_{l-l} \tag{6.30}$$

with

$$S = \delta\sigma_3 - i\sigma_1\,.$$

From equation (6.30) we construct a matrix of the following form

$$\begin{pmatrix} \psi_{l+1} \\ \psi_l \end{pmatrix} = T_l \begin{pmatrix} \psi_l \\ \psi_{l-1} \end{pmatrix}, \tag{6.31}$$

which is explicitly written as

$$T_l = \begin{bmatrix} \frac{2\delta\,(E+\delta-m_l)}{\delta^2-1} & -\frac{2\,i(E-\delta+m_l)}{\delta^2-1} & \frac{-\delta^2-1}{\delta^2-1} & -\frac{2\,i\delta}{\delta^2-1} \\ -\frac{2\,i(E+\delta-m_l)}{\delta^2-1} & -\frac{2\delta\,(E-\delta+m_l)}{\delta^2-1} & \frac{2\,i\delta}{\delta^2-1} & \frac{-\delta^2-1}{\delta^2-1} \\ 1 & 0 & 0 & 0 \\ 0 & 1 & 0 & 0 \end{bmatrix}. \tag{6.32}$$

The eigenvalues are given by

$$\tau_1 = -\frac{1}{\delta^2-1}\left(-\delta^2+\delta m_l-\sqrt{1+f}\right.$$
$$\left.-\sqrt{-2\delta^3 m_l-2\delta^2\sqrt{1+f}+m_l^2\delta^2-2\delta m_l\sqrt{1+f}+f+2\delta^2}\right)$$

$$\tau_2 = -\frac{1}{\delta^2-1}\left(-\delta^2+\delta m_l-\sqrt{1+f}\right.$$
$$\left.+\sqrt{-2\delta^3 m_l+2\delta^2\sqrt{1+f}+m_l^2\delta^2-2\delta m_l\sqrt{1+f}+f+2\delta^2}\right)$$

$$\tau_3 = -\frac{1}{\delta^2-1}\left(-\delta^2+\delta m_l+\sqrt{1+f}\right.$$
$$\left.-\sqrt{-2\delta^3 m_l-2\delta^2\sqrt{1+f}+m_l^2\delta^2+2\delta m_l\sqrt{1+f}+f+2\delta^2}\right)$$

$$\tau_4 = -\frac{1}{\delta^2-1}\left(-\delta^2+\delta m_l+\sqrt{1+f}\right.$$
$$\left.+\sqrt{-2\delta^3 m_l-2\delta^2\sqrt{1+f}+m_l^2\delta^2+2\delta m_l\sqrt{1+f}+f+2\delta^2}\right) \tag{6.33}$$

with $f = E^2\delta^2 - E^2 - 2\delta m_l + m_l^2$. To see whether states are either extended or localized, we distinguish four cases: Gapped ($m = 0.2$), ungapped ($m = 0.0$) and one ($\delta = 0.5$) or two Dirac cones ($\delta = 0.0$).

First we consider the clean case and calculate $\gamma_i = \Re(\ln(\tau_i))$ as a function of energy. Figure 6.3 (left panel) shows the results for two Dirac cones without a gap. Up to energies of $E \approx 1$ all four Lyapunov exponents are degenerate and zero, which means that all states in this case are extended. In figure 6.3 (right panel) the model has also extended states up to high energies. If we now look at the gapped case we see in both cases, cf. left panel in figure 6.4 and right panel

in figure 6.4, that for energies around the Dirac point (i.e. $E = 0$) all Lyapunov exponents are non-zero, which means that the states are exponential decaying. For energies bigger than the gap $E > 0.2$ at least two Lyapunov exponents go to zero and extended states appear again. For the gapped and the ungapped case the valley symmetry breaking results in a degeneracy lifting of the Lyapunov exponents. Since Lyapunov exponents are in the clean case related to the wave number (cf. equation (4.12)) the latter behavior is evident.
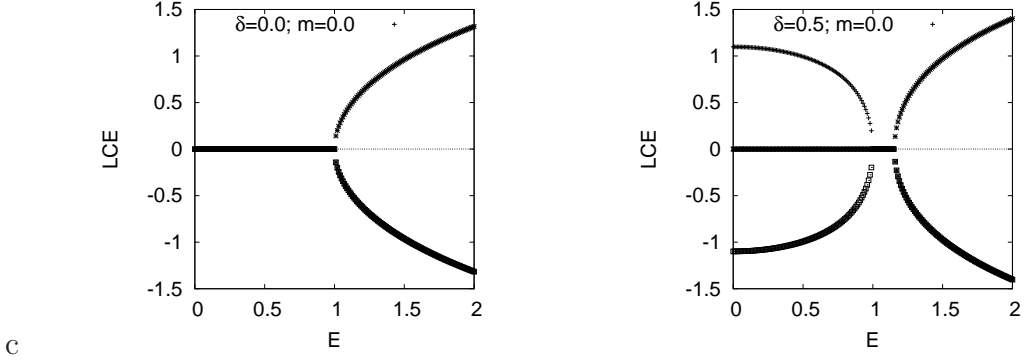


c

**Figure 6.3.:** Lyapunov exponents for the gapless case in one dimension. Left panel: $m = 0$ and $\delta = 0$; Right panel: $m = 0$ and $\delta = 0.5$.
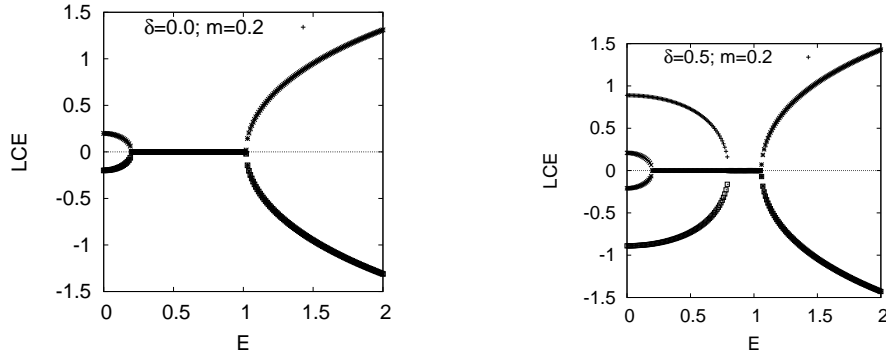


**Figure 6.4.:** Lyapunov exponents for the gapped case in one dimension. Left panel: $m = 0.2$ and $\delta = 0$; Right panel: $m = 0.2$ and $\delta = 0.5$.

**Random gap**

We now proceed and include a random gap in equation (6.32) as a model for disorder. At each lattice point we choose a random value for $m_l$ taken from a uniform distribution of width $W$ on the interval $[\bar{m} - W/2, \bar{m} + W/2]$ and calculate

the spectrum of Lyapunov exponents as described in section 4.2. This allows us to compare results obtained from the recurrence equation with those from the transfer matrix method. The results for preserved and broken valley symmetry are presented in figure 6.5. The difference between both cases is that the two-fold degeneracy of the Lyapunov exponents is lifted for $\delta \neq 0$. Qualitatively we see similar behavior as in section 6.1.1. As an representative example the result from the recurrence equation for $\bar{m} = 0.3$ is included in the left panel of figure 6.5. Both methods give the same result. For increasing disorder strength the smallest Lyapunov exponent increases thus the localization length decreases respectively.

The lattice model we used so far is nothing else than scattering of a Dirac fermion at $N$-barriers. We can identify each lattice point with a barrier of random height. Thus, by adjusting the barrier width in the continuous version of the transfer matrix (3.8) used in section 3.1.2 we should be able to calculate the same result as in the discrete case. Figure 6.6 clearly shows that this is the case for random gap with zero mean and uniform distribution.
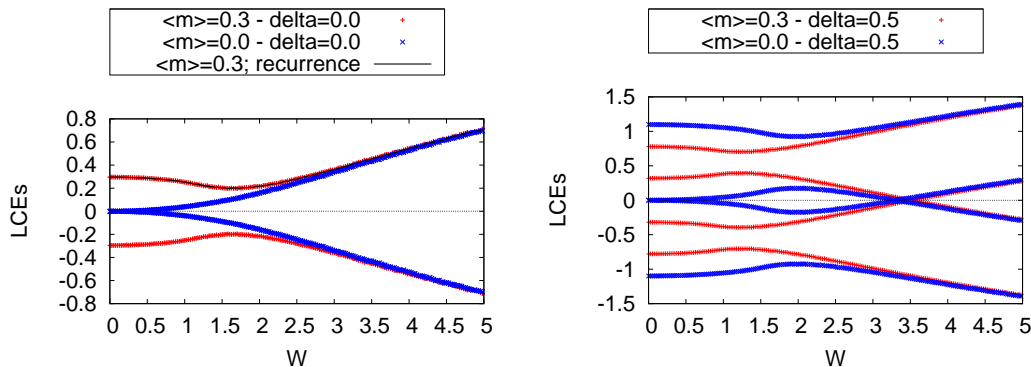


**Figure 6.5.:** Lyapunov spectrum for Dirac fermions in one dimension with random gap over width of uniform distribution, in red numerical results for the gapped and blue for the ungapped case. Left: Preserved valley symmetry, the black line is the result of the recurrence equation. Right: broken valley symmetry
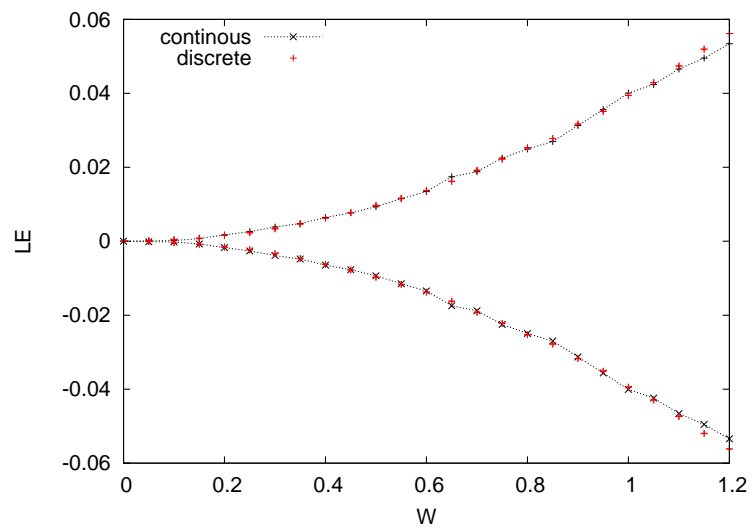
**Figure 6.6.:** Comparison of the Lyapunov exponents obtained from the transfer matrix for the continuous case with those from the discrete case. The dotted line is a guide for the eye.

## 6.2. Discretization in two dimensions

Now that we have established a reliable method to calculate Lyapunov exponents by means of transfer matrices, we proceed and derive a discrete version of the two dimensional Dirac equation.

### 6.2.1. Symmetric discretization – model $A$

As we have already mentioned, it was soon recognized that a naive discretization of the Dirac equation leads to additional fermions. In real space there are two methods to circumvent this problem. The one that we will describe here goes back to ideas of Susskind [68]. For the derivation we will only consider the random gap problem and give the expressions for vector and scalar potential later.

The Dirac equation for a free particle reads in matrix notation

$$-i\hbar \begin{pmatrix} 0 & i\partial_x + \partial_y \\ i\partial_x - \partial_y & 0 \end{pmatrix} \begin{pmatrix} \varphi_1 \\ \varphi_2 \end{pmatrix} = E \begin{pmatrix} \varphi_1 \\ \varphi_2 \end{pmatrix} \tag{6.34}$$

and accordingly, the Dirac Hamiltonian is given by

$$H = -i\hbar(\sigma_1 \partial_x + \sigma_2 \partial_y). \tag{6.35}$$

We discretize the differential operator in a symmetric way

$$\partial_x f(x) \approx \frac{1}{2\Delta}(f_{l+\Delta} - f_{l-\Delta}), \tag{6.36}$$

where $\Delta$ is the lattice constant, which we set to unity in the following. The discrete Dirac equation for free particles takes then the form

$$-\frac{i}{2}\sigma_1 \{\psi_{l+1,n} - \psi_{l-1,n}\} - \frac{i}{2}\sigma_2 \{\psi_{l,n+1} - \psi_{l,n-1}\} = E\sigma_0 \psi_{l,n}.$$

A lattice point is given by the coordinates $(l, n)$ with integer numbers $l$ and $n$. Because of translational invariance, diagonalization by Fourier transformation is possible

$$E = \pm\sqrt{\sin^2(k_x) + \sin^2(k_y)}. \tag{6.37}$$

The latter spectrum has four nodal points in the Brillouin zone corresponding to four Dirac fermions. Figure 6.7 shows a density plot of dispersion (6.37). The red circles indicate the location of Dirac cones. Only the cone in the center lies fully in the Brillouin zone. Cones at the border are counted as $1/2$, cones at the corners with $1/4$.
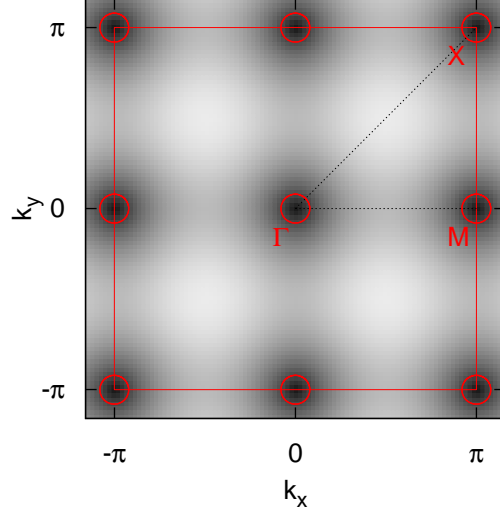
**Figure 6.7.:** Density plot of the energy dispersion (6.41) for the discretized Dirac equation with $\delta = 0$ and $m = 0$. Brillouin zone and points of high symmetry are in red. The location of the Dirac cones is indicated by red circles.

In order to lift the valley degeneracy and thus remove the fermion doubling, we introduce a lattice operator [70] analogous to that in one dimension

$$\sigma_3 \hat{B} \, \psi_{l,n} = \frac{1}{2}\sigma_3 \left\{ \psi_{l+1,n} + \psi_{l-1,n} + \psi_{l,n+1} + \psi_{l,n-1} \right\} . \tag{6.38}$$

We transform Hamiltonian (6.35) by including the lattice operator $\hat{B}$ and a random gap term

$$H \to H + \delta(\hat{B} - 2)\sigma_3 + m_{l,n}\,\sigma_3 . \tag{6.39}$$

Our new Hamiltonian reads in Fourier representation

$$\tilde{H} = \begin{pmatrix} m + \delta(\cos(k_x) + \cos(k_y) - 2) & \sin(k_x) + i\sin(k_y) \\ \sin(k_x) - i\sin(k_y) & -m - \delta(\cos(k_x) + \cos(k_y) - 2) \end{pmatrix} \tag{6.40}$$

with energy dispersion

$$E = \pm\sqrt{\sin^2(k_x) + \sin^2(k_y) + (m + \delta\cos(k_x) + \delta\cos(k_y) - 2\delta)^2} . \tag{6.41}$$

The resulting band structure is shown in figure 6.8 for several parameter combinations. In the simplest case ($\delta = 0, m = 0$), we have four nodal points in total. One node located at point $\Gamma$ in the center, two at $M$ and one in the corners at $X$. If we set $0 < \delta < 1$ and leave $m = 0$ we open a gap at $M$ and $X$ retaining only one Dirac Point at $\Gamma$ in the Brillouin zone. If we increase the mass with $m < \delta$, a gap opens also at the $\Gamma$-point. When the mass reaches $m = 2\delta$ two Dirac fermions appear again at $M$, for $m = 4\delta$ the nodes appear at $X$. Consequently, we can choose the number of Dirac fermions by tuning the parameter $\delta$ with the prize that our model is not symmetric when replacing $m \to -m$. The bandwidth depends on the certain combination of parameters and is e.g. $\triangle E \approx 2.23$ for $\delta = 0$ or $\triangle E = 4$ for $\delta = 0.5$ in the gapless case and not symmetric in $m$.
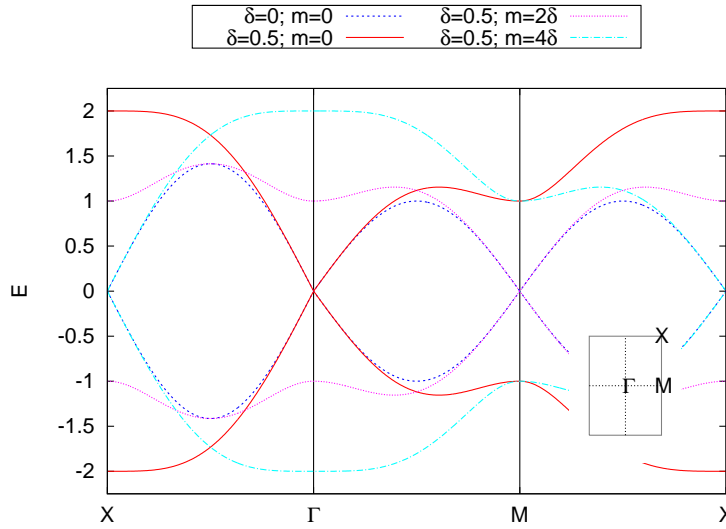


**Figure 6.8.:** Energy dispersion (6.41) of the discretized Dirac equation for various combinations of $\delta$ and $m$ connecting points of high symmetry. The inset represents the Brillouin zone with symmetry points

## Transfer matrix

Our goal is now to obtain a transfer matrix which connects column $l + 1$ with column $l$ of our lattice, cf. figure 6.9. To achieve this we rearrange the discrete Dirac equation with lattice operator $\hat{B}$ and random gap

$$\psi_{l+1,n} = 2 \, S^{-1} \left[ E\sigma_0 + (2\delta - m)\sigma_3 \right] \psi_{l,n} - S^{-1} \left[ i\sigma_1 + \delta\sigma_3 \right] \psi_{l-1,n}$$
$$+ S^{-1} \left[ i\sigma_2 - \delta\sigma_3 \right] \psi_{l,n+1} - S^{-1} \left[ i\sigma_2 + \delta\sigma_3 \right] \psi_{l,n-1} \,, \qquad (6.42)$$

with

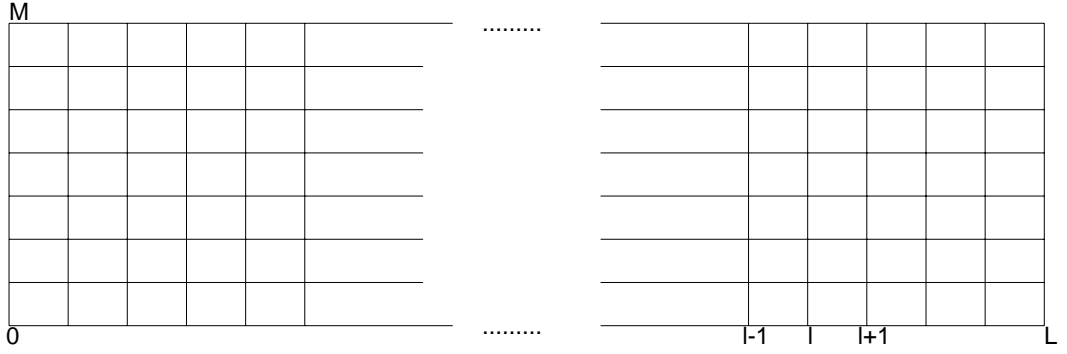$$S = \left[ -i\sigma_1 + \delta\sigma_3 \right] . \qquad (6.43)$$

**Figure 6.9.:** Illustration of the $M \times L$ lattice used for the transfer matrix method.

We absorb the transverse index $n$ with the help of two matrices

$$\psi_{l+1} = H^Y \, \psi_l + H^D \, \psi_{l-1} \, . \tag{6.44}$$

with non-zero elements given by

$$H^Y_{n,n} = 2S^{-1} \left[ E \, \sigma_0 + (2\delta - m)\sigma_3 \right] \qquad H^Y_{n,n+1} = S^{-1} \left[ i\sigma_2 - \delta\sigma_3 \right]$$
$$H^Y_{n,n-1} = -S^{-1} \left[ i\sigma_2 + \delta\sigma_3 \right] \qquad H^D_{n,n} = -S^{-1} \left[ i\sigma_1 + \delta\sigma_3 \right]$$

Each spinor component is now a $M$-component vector, where $M$ is the width of a strip and thus $n = 1, 2, ..., M$. The matrix $H^Y$ contains periodicity in $y$-direction yielding

$$\to H^Y_{M,1} = H^Y_{1,M}$$

This allows us to construct a transfer matrix similar to [9]

$$\begin{pmatrix} \psi_{l+1} \\ \psi_l \end{pmatrix} = \begin{pmatrix} H^Y & H^D \\ \mathbb{1} & 0 \end{pmatrix} \begin{pmatrix} \psi_l \\ \psi_{l-1} \end{pmatrix} = T_l \begin{pmatrix} \psi_l \\ \psi_{l-1} \end{pmatrix} \, . \tag{6.45}$$

It is convenient to have all entries in explicit matrix form for implementation in a programming language. The diagonal term of $H^Y$ reads

$$S^{-1} \left[ E \, \sigma_0 + (2\delta - m)\sigma_3 \right] = \frac{1}{\delta^2 - 1} \begin{pmatrix} \delta(E + 2\delta - m) & -i(E - 2\delta + m) \\ -i(E + 2\delta - m) & -\delta(E - 2\delta + m) \end{pmatrix} \tag{6.46}$$

its upper off-diagonal term is

$$S^{-1} \left[ i\sigma_2 - \delta\sigma_3 \right] = \frac{1}{\delta^2 - 1} \begin{pmatrix} -\delta^2 + i & \delta(1 - i) \\ \delta(1 + i) & -\delta^2 - i \end{pmatrix} \tag{6.47}$$

and the lower off-diagonal term of $H^Y$ is given by

$$-S^{-1}\left[i\sigma_2 + \delta\sigma_3\right] = \frac{1}{\delta^2 - 1}\begin{pmatrix} -\delta^2 - i & -\delta(1+i) \\ \delta(-1+i) & -\delta^2 + i \end{pmatrix} \tag{6.48}$$

The diagonal entries of $H^D$ read

$$-S^{-1}\left[i\sigma_1 + \delta\sigma_3\right] = \frac{1}{\delta^2 - 1}\begin{pmatrix} -\delta^2 - 1 & -2i\delta \\ 2i\delta & -\delta^2 - 1 \end{pmatrix} \tag{6.49}$$

Since the prefactor of the latter matrices diverges for $\delta = 1$ we are restricted to values $\delta < 1$, which is by no means problematic for later calculations. The introduction of a different random potential, e.g. random scalar potential is discussed below.

### Random scalar potential

To include scalar disorder, in this problem we transform the Hamiltonian by

$$H \to H + \delta(\hat{B} - 2)\sigma_3 + U(l, n)\,\sigma_0\,. \tag{6.50}$$

Equation (6.42) becomes

$$\begin{aligned}
\psi_{l+1,n} =\,& 2\Delta S^{-1}\left[E\sigma_0 + 2\delta\sigma_3 - U\sigma_0\right]\psi_{l,n} - S^{-1}\left[i\sigma_1 + \delta\sigma_3\right]\psi_{l-1,n} \\
& + S^{-1}\left[i\sigma_2 - \delta\sigma_3\right]\psi_{l,n+1} - S^{-1}\left[i\sigma_2 + \delta\sigma_3\right]\psi_{l,n-1}
\end{aligned} \tag{6.51}$$

and only the diagonal entry of $H^Y$ changes

$$S^{-1}\left[E\,\sigma_0 + 2\delta\sigma_3 - U\sigma_0\right] = \frac{1}{\delta^2 - 1}\begin{pmatrix} \delta(E + 2\delta - U) & -i(E - 2\delta - U) \\ -i(E + 2\delta - U) & -\delta(E - 2\delta - U) \end{pmatrix}\,. \tag{6.52}$$

### Random vector potential

We introduce a vector potential in the following form

$$H \to H + \delta(\hat{B} - 2)\sigma_3 + V_1(l, n)\,\sigma_1 + V_2(l, n)\,\sigma_0\,. \tag{6.53}$$

This implies for equation (6.42) $\Rightarrow$

$$\begin{aligned}
\psi_{l+1,n} =\,& 2\Delta S^{-1}\left[E\sigma_0 + 2\delta\sigma_3 - V_1\sigma_1 - V_2\sigma_2\right]\psi_{l,n} \\
& - S^{-1}\left[i\sigma_1 + \delta\sigma_3\right]\psi_{l-1,n} & (6.54) \\
& + S^{-1}\left[i\sigma_2 - \delta\sigma_3\right]\psi_{l,n+1} - S^{-1}\left[i\sigma_2 + \delta\sigma_3\right]\psi_{l,n-1}\,. & (6.55)
\end{aligned}$$

As in the two cases before, the random vector potential only affects the diagonal term of $H^Y$

$$S^{-1}\left[E\,\sigma_0 + 2\delta\sigma_3 - V_1\sigma_1 - V_2\sigma_2\right] = \tag{6.56}$$

$$\frac{1}{\delta^2 - 1}\begin{pmatrix} \delta(E + 2\delta) + iV_1 - V_2 & -i(E - 2\delta) - \delta V_1 + i\delta V_2 \\ -i(E + 2\delta) + \delta V_1 + i\delta V_2 & -\delta(E - 2\delta) + iV_1 + V_2 \end{pmatrix} \tag{6.57}$$

**Symmetry properties of the transfer matrix**

In the tight-binding model for on-site disorder, the transfer matrix is symplectic [9, 63] (or $J$-orthogonal) which means that the relation

$$T^\dagger \, J \, T = J \,, \tag{6.58}$$

with

$$J = \begin{pmatrix} 0 & -\mathbb{1} \\ \mathbb{1} & 0 \end{pmatrix} \tag{6.59}$$

is fulfilled. This property implies that eigenvalues of $T$ appear in inverse pairs $\lambda_i$ and $1/\lambda_i$. Every Lyapunov exponent $\gamma_i$ has its negative counterpart, corresponding to back and forth going states. Thus, in- and outgoing fluxes are equal, yielding that the transfer matrix represents an area preserving map with $\det(T) = 1$, if so the current is conserved.

To make sure that the transfer matrix for the discretized Dirac equation is reasonable, we have to assure the current conservation. Recalling its structure

$$T_l = \begin{pmatrix} H^Y & H^D \\ \mathbb{1} & 0 \end{pmatrix}$$

and evaluation the condition for symplecticity gives

$$T_l^\dagger \, J \, T_l = \begin{pmatrix} H^Y - (H^Y)^\dagger & H^D \\ -H^D & 0 \end{pmatrix} = -J, \tag{6.60}$$

which is valid for $\delta = 0$. Apparently, the demanded result differs by a sign but this has no effect on the determinant of the transfer matrix and it follows $\det(T) = 1$. For the case of the broken valley symmetry ($\delta \neq 0$) we prove current conservation by calculating the determinant directly. The matrix $T$ has a block structure and consists of four blocks with dimension $2M \times 2M$. The block $H^Y$ is invertible for $\delta \neq 0$ and the determinant can be written as

$$\det(T) = \det(H^Y)\det(-(H^Y)^{-1}H^D) = \underbrace{\det(H^Y)\det(-(H^Y)^{-1})}_{=1} \det(H^D) \,. \tag{6.61}$$

The matrix $H^D$ itself consists of $M$ $2 \times 2$ blocks cf. equation (6.49)

$$h^D = \frac{1}{\delta^2 - 1} \begin{pmatrix} -\delta^2 - 1 & -2i\delta \\ 2i\delta & -\delta^2 - 1 \end{pmatrix} \tag{6.62}$$

in the diagonal. Hence

$$\det(H^D) = [\det(h^D)]^N = \left[ \frac{1}{(\delta^2 - 1)^2} \{(\delta^2 + 1)^2 - 4\delta^2\} \right]^N = 1 \tag{6.63}$$

and it follows that $\det(T) = 1$ as required for current conservation. Consequently, all eigenvalues come in inverse pairs $\lambda_i$ and $1/\lambda_i$ also for $\delta \neq 0$.

Since the product of all eigenvalues equals unity, it follows

$$\sum_{i=1}^{4M} \gamma_i = 0 \,. \tag{6.64}$$

In numerical calculations this has been used to control the accuracy and also the validity of the results. In our case the sum of all Lyapunov exponents was of the numerically reasonable order $\approx 10^{-15}$. Increasing the number of multiplications between each orthonormalization increases the sum of Lyapunov exponents.

The continuous version of the Hamiltonian for free Dirac particles fulfills the following symmetry transformations

$$
\begin{aligned}
\sigma_1 H^\star \sigma_1 &= -H & \text{particle} - \text{hole} \\
\sigma_2 H^\star \sigma_2 &= H & \text{spin rotation} \\
\sigma_3 H \sigma_3 &= -H & \text{chiral} \,.
\end{aligned}
\tag{6.65}
$$

Including a scalar potential breaks the chiral symmetry. The mass term i.e. anything that couples to $\sigma_3$ breaks the chiral and the spin rotation symmetry. For the transfer matrix the mentioned symmetries at the Dirac point $(E = 0)$ translate to

$$
\begin{aligned}
\sigma_1 T^\star \sigma_1 &= T \\
\sigma_2 T^\star \sigma_2 &= T \\
\sigma_3 T \sigma_3 &= T \,.
\end{aligned}
\tag{6.66}
$$

Table 6.1 summarizes all symmetry transformations. Additionally, we like to mention that setting $\delta$ to a non-zero value has the same effect as a non-zero mass.

| Random potential: | Free | Scalar | Mass | Vector |
|---|:---:|:---:|:---:|:---:|
| $\sigma_1 T^\star \sigma_1 = T$ | $\checkmark$ | x | $\checkmark$ | x |
| $\sigma_2 T^\star \sigma_2 = T$ | $\checkmark$ | $\checkmark$ | x | x |
| $\sigma_3 T \sigma_3 = T$ | $\checkmark$ | x | x | $\checkmark$ |

**Table 6.1.:** Symmetry transformations of the transfer matrix for different types of disorder.

## 6.2.2. Simplified model $A$ and weak disorder expansion

Let us now develop a simplified model as a basis for the weak disorder expansion which we introduce subsequently. As mentioned before, each transfer matrix has a $2 \times 2$ block structure and each block is of size $2M \times 2M$. That means, that we have to deal with relatively large matrices and since we need wide strips for reliable results, calculations become quite time consuming.

This encourages us to deal with simplified models: Assume that we choose random numbers only for each column of the lattice. Each strip has consequently the same mass $m_l$, and therefore, each transfer matrix is in this sense non-random. This allows us to perform a Fourier transformation in the transverse direction $n$ and thus to diagonalize the block $H^Y$

$$\delta_{n,n+1} - \delta_{n,n-1} \longrightarrow 2i \sin(k_y)$$
$$\delta_{n,n+1} + \delta_{n,n-1} \longrightarrow 2 \cos(k_y)\,,$$

with $k_y = 2\pi n/M$ being the transverse wave number. Hence, we get for

$$\tilde{H}^Y = 2S^{-1}\{[E\sigma_0 + (2\delta - \delta \cos(k_y) - m)\sigma_3] + \sin(k_y)\sigma_2\}\,. \qquad (6.67)$$

The block $H^D$ is already diagonal in $n$ and we rewrite the transfer matrix

$$\tilde{T}_l = \begin{pmatrix} \frac{-2S\{E\sigma_0 + f_3(k_y,m_l)\sigma_3 + f_2(k_y)\sigma_2\}}{1-\delta^2} & \frac{(\delta^2+1)\sigma_0 - 2\delta\sigma_2}{1-\delta^2} \\ \sigma_0 & 0 \end{pmatrix}\,, \qquad (6.68)$$

where we have used $f_2(k_y) = \sin(k_y)$ and $f_3(k_y, m_l) = 2\delta - \delta \cos(k_y) - m_l$. Our minimal model is now effectively one dimensional and we are free to choose the transverse mode.

This model can be used as a testing ground for the developed *fortran* code, just like the recurrence equations. As an example we show in figure 6.10 the results for one Dirac cone with uniform gap without disorder. Here, we calculated the Lyapunov exponents from the transfer matrix defined in equation (6.45) and from the minimal model. The only propagating mode is that for $n = M$ yielding $k_y = 0$ which gives also the smallest Lyapunov exponent. As we would expect both models give the same results.

For the special case of $E = 0$ and the transverse edge mode we can evaluate the eigenvalues of (6.68) as

$$\lambda = \frac{\delta - m \pm \sqrt{1 - 2\delta m + m^2}}{\delta \pm 1} \qquad (6.69)$$

and for $\delta = 0$ we can expand the Lyapunov exponent in powers of $m$

$$\lambda = \pm m \pm \sqrt{1 + m^2} \to \gamma_{min} = \Re(\ln(\lambda_{min})) = m + \mathcal{O}(m^3)\,. \qquad (6.70)$$
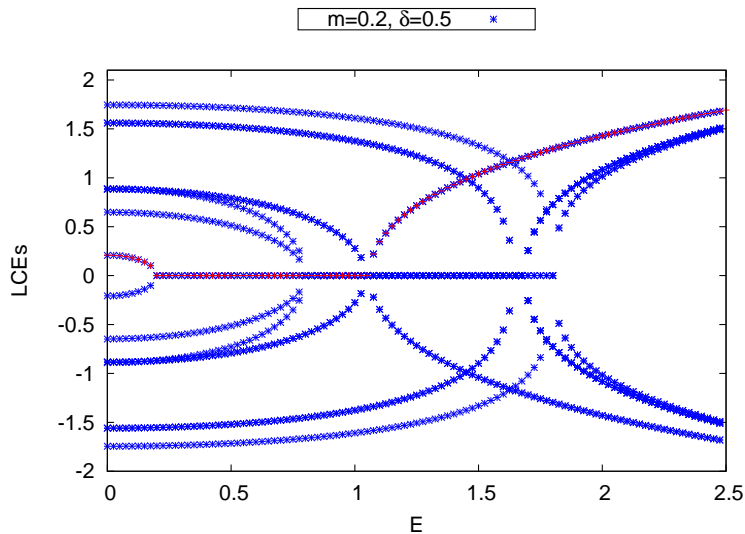
**Figure 6.10.:** Lyapunov spectrum for $M = 4$ vs. energy for one cone $\delta = 0.5$ and uniform gap $m = 0.2$. The blue data points depict the results obtained from the transfer matrix defined in (6.45), the red points depict the smallest positive Lyapunov exponent calculated from (6.68).

This means that the smallest positive Lyapunov exponent is approximately proportional to the mass $m$ and independent of the system width $M$. As a direct consequence, the rescaled Lyapunov exponent grows linearly with system size, pictured in figure 6.11. Owing to the fact that the normalized localization length is the inverse of $M\gamma_{min}$, clean systems with finite mass show insulating behavior for $E = 0$.

Let us now consider the disordered case. For this reason we choose $m_l$ to be uniformly distributed in the interval $[\bar{m} - W/2, \bar{m} + W/2]$. Since the transfer matrix is only of dimension $4 \times 4$, calculations are fast and we are able to produce a density plot 6.12, where we present the results for one and four Dirac cones.

For $\delta = 0$, increasing $W$ or $\bar{m}$ always results in a growing Lyapunov exponent, whereas for $\delta \neq 0$ there is an intermediate regime at $W \approx 3.5$ where it seems that $\gamma_{min}$ goes to zero. Plotting a cross section (cf. 6.13) for fixed $\bar{m}$ shows that this is apparently not the case. Although $\gamma_{min}$ decays in the range of $2 < W < 3.5$ it never reaches zero. Comparing the latter to the results presented in the left panel of figure 6.1, suggests that both methods are equivalent.

Concluding, we have shown that the minimal model is effectively one dimensional and Dirac fermions are localized for non-zero disorder although there exists a regime where the Lyapunov exponent reaches a local minimum for $\delta \neq 0$. This
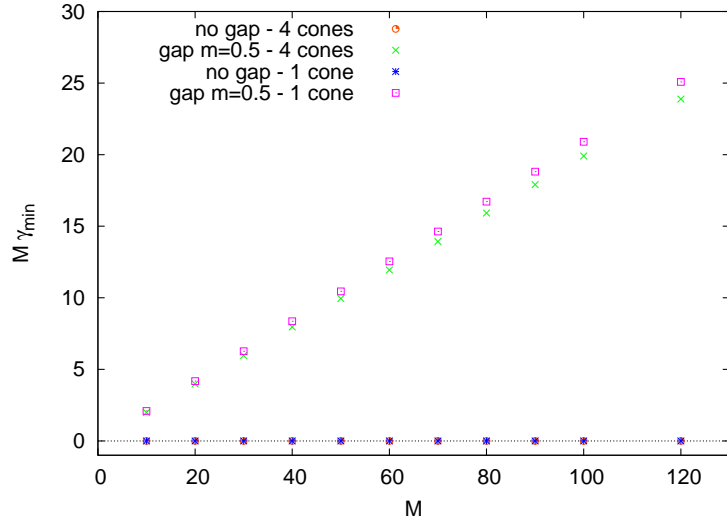
**Figure 6.11.:** Smallest Lyapunov exponents at $E = 0$ for clean systems.

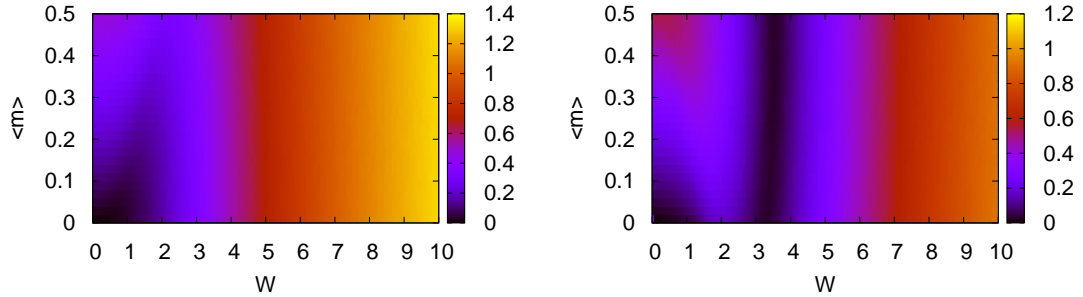corresponds to results of section 6.1.



**Figure 6.12.:** Smallest Lyapunov exponent as a function of $\bar{m}$ and disorder strength $W$ for the minimal model. The left panel corresponds to $\delta = 0$ and the right panel to $\delta = 0.5$.

**Weak disorder expansion**

Apart from the result for a tight-binding chain with Cauchy distributed disorder discussed in Ref. [71] it is most likely hopeless to derive an analytical result for $\gamma$, even for the minimal model. How could we check, if our results for disordered systems are correct? One possibility would be a perturbation theory and indeed
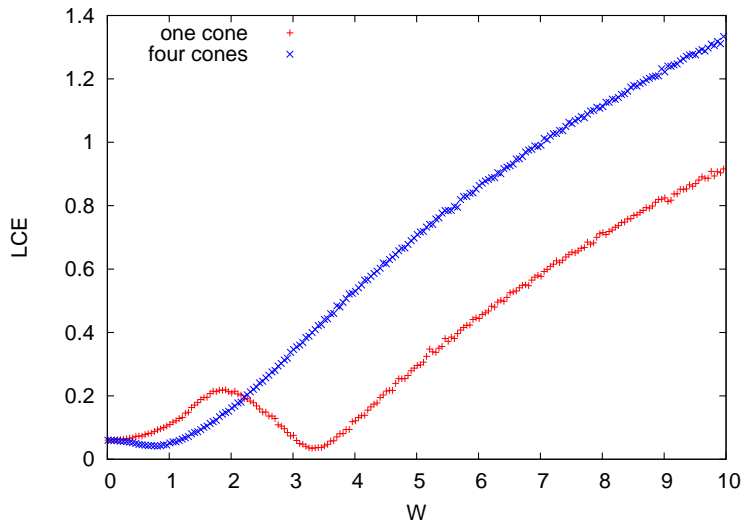
**Figure 6.13.:** Cross section from fig 6.12.

such a method was derived by Derrida et al. [72] and is called weak disorder expansion (WDE).

In this section we like to apply this perturbation method to the simplified model up to fourth order. Before giving the rather lengthy expression, we want to illustrate the derivation up to second order, following Ref. [72].

If disorder is small, we may decompose the transfer matrix

$$T_l = A + \mu B_l \tag{6.71}$$

into a non-random part $A$, independent from $l$ and into a random part $B_l$. The random numbers should be independent and the parameter $\mu$ kept small. Furthermore, all eigenvalues of $A$ have to be non-degenerate with different modulus

$$|\lambda_1| > |\lambda_2| > \ ... \ |\lambda_q| \, . \tag{6.72}$$

If these conditions are satisfied, an expansion of the sum of Lyapunov exponents in powers of $\mu$ is possible. For the minimal model this is the case for $\delta \neq 0$ and $\bar{m} \neq 0$.

Let us assume $A$ to be already diagonal with all eigenvalues ordered by size. If this is not the case, we can always change the basis using an appropriate transformation $S$

$$S^{-1} T_l S = A + \mu \ S^{-1} B_l S \, . \tag{6.73}$$

Furthermore, we assume the size of matrices to be $N \times N$. We choose $p$ different

arbitrary vectors $U_i$ with length $N$ and define

$$\mathcal{W}_i = \left( \prod_{l=1}^{N} T_l \right) U_i .$$  (6.74)

The sum of the first $p$ Lyapunov exponents is given by the exponential growth rate of a $p$–dimensional volume spanned by $p$-vectors $U_i$. A possible measure for the volume is

$$\det{}_p(U_1, U_2, ..., U_p),$$  (6.75)

where $(U_1, U_2, ..., U_p)$ is a $p \times p$ matrix containing the fist $p$ entries of vectors $U_i$. Consequently, the first $p$ Lyapunov exponents can be obtained from

$$\sum_{i=1}^{p} \gamma_i = \lim_{N \to \infty} \frac{1}{N} \log \left[ \frac{\det_p(\mathcal{W}_1, \mathcal{W}_2, ..., \mathcal{W}_p)}{\det_p(U_1, U_2, ..., U_p)} \right]$$

$$= \lim_{N \to \infty} \frac{1}{N} \log \left( \prod_{l=1}^{N} T_l \right) = \lim_{N \to \infty} \frac{1}{N} \log(\mathcal{P}_N) .$$  (6.76)

We can now expand the product $\mathcal{P}_N$ in $\mu$ and it turns out that it is sufficient to expand only up to order $\mu^{q/2}$, if one needs to compute $\gamma_i$ up to the order $\mu^q$. The first order expansion of the product yields

$$\mathcal{P}_N = A^N + \mu \prod_{l=1}^{N} A^{N-l} B_l A^{l-1}$$

$$= A^N \left( \mathbb{1} + \mu \prod_{l=1}^{N} A^{-l} B_l A^{l-1} \right)$$

$$= A^N \left( \mathbb{1} + \mu C \right) .$$  (6.77)

In the next step we have to evaluate the logarithm of the product, where we can use the the identity $\log(\det(X)) = \text{Tr}(\log(X))$ with $\text{Tr}(\ )$ being the trace operator. Thus

$$\log\left( \det(\mathcal{P}_N) \right) = \log \left( \det(\tilde{A}^N) \right) + \log \left( \det \left( \tilde{\mathbb{1}} + \mu \, \tilde{C} \right) \right)$$

$$= \text{Tr} \left( \log(\tilde{A}^N) \right) + \text{Tr} \left( \log(\tilde{\mathbb{1}} + \mu \, \tilde{C}) \right) ,$$  (6.78)

where matrices with a tilde ($\tilde{\ }$) contain only first $p$ columns and rows. The purpose of writing the product expansion (6.76) $\propto \mu(1 + x)$ is that we can now expand its logarithm as

$$\log\left( \det(\mathcal{P}_N) \right) = \text{Tr} \left( \log(\tilde{A}^N) \right) + \mu \, \text{Tr}(\tilde{C}) - \frac{1}{2} \mu^2 \, \text{Tr}(\tilde{C}^2) + \mathcal{O}(\mu^2) .$$  (6.79)

If we assume $\langle B_l \rangle = 0$ with $\langle ... \rangle$ being the average over disorder and symmetric probability distribution, we obtain

$$\langle B_l \rangle = 0 \Rightarrow \lim_{N \to \infty} \frac{1}{N} \operatorname{Tr}(\tilde{C}) = 0 \,. \tag{6.80}$$

This also implies that all odd moments are zero and we have no terms of odd order in $\mu$. For the remaining terms we have

$$\lim_{N \to \infty} \frac{1}{N} \operatorname{Tr}(\tilde{C}^2) = \sum_{i=1}^{p} \sum_{j=1}^{p} \frac{\langle B_{ij} B_{ji} \rangle}{\lambda_i \, \lambda_j} \tag{6.81}$$

and

$$\lim_{N \to \infty} \frac{1}{N} \operatorname{Tr}\left( \log(\tilde{A}^N) \right) = \operatorname{Tr}\left( \log(\tilde{A}) \right) = \sum_{i=1}^{p} \log(\lambda_i) \,. \tag{6.82}$$

The evaluation of higher order terms is analogous. As a result the weak disorder expansion up to fourth order in $\mu$ for the sum of the first $p$ Lyapunov exponents is given by [72]

$$\begin{aligned}
\sum_{i=1}^{p} \gamma_i = &\sum_{j=1}^{p} \log \lambda_j - \frac{\mu^2}{2} \sum_{i=1}^{p} \sum_{j=1}^{p} \frac{\langle B^{ji} B^{ij} \rangle}{\lambda_i \lambda_j} \\
&- \frac{\mu^4}{4} \sum_{i=1}^{p} \sum_{j=1}^{p} \sum_{k=1}^{p} \sum_{l=1}^{p} \frac{\langle B^{ij} B^{jk} B^{kl} B^{li} \rangle}{\lambda_i \lambda_j \lambda_k \lambda_l} \\
&- \frac{\mu^4}{2} \sum_{i=1}^{p} \sum_{j=1}^{p} \sum_{r>p}^{q} \sum_{s>p}^{q} \frac{\langle B^{ir} B^{js} \rangle \langle B^{rj} B^{si} \rangle}{\lambda_i \lambda_j (\lambda_i \lambda_j - \lambda_r \lambda_s)} \\
&+ \mu^4 \sum_{i=1}^{p} \sum_{j=1}^{p} \sum_{k=1}^{p} \sum_{r>p}^{q} \frac{\langle B^{ir} B^{kl} \rangle \langle B^{rj} B^{jk} \rangle}{\lambda_i \lambda_j \lambda_k (\lambda_j - \lambda_r)} \,.
\end{aligned} \tag{6.83}$$

Let us now apply the weak disorder expansion to the minimal model (6.68) for the zero mode $k_y = 0$ to check if our numerical results are consistent. We ensure that conditions are fulfilled by setting $\delta \neq 0$ and $\bar{m} \neq 0$. All four eigenvalues (6.69) have then different moduli. Restricting our calculations to the Dirac point $E = 0$

and setting $m_l = m + \Delta m_l$, the transfer matrix (6.68) can be decomposed as

$$T_l = \frac{1}{\delta^2 - 1} \begin{pmatrix} 2\delta(\delta - m) & 2i(\delta - m) & -1 - \delta^2 & -2i\delta \\ -2i(\delta - m) & 2\delta(\delta - m) & 2i\delta & -1 - \delta^2 \\ 1 & 0 & 0 & 0 \\ 0 & 1 & 0 & 0 \end{pmatrix}$$

$$+ \frac{\Delta m_l}{\delta^2 - 1} \begin{pmatrix} -2\delta & -2i\delta & 0 & 0 \\ 2i\delta & -2\delta & 0 & 0 \\ 0 & 0 & 0 & 0 \\ 0 & 0 & 0 & 0 \end{pmatrix} = T_0 + T_l \ . \tag{6.84}$$

For the first example we set $\delta = 1/2$ and $\bar{m} = 1/5$ and in the basis where $T_0$ is diagonal we get

$$A = \mathrm{diag}(\lambda_1, \lambda_2, \lambda_3, \lambda_4)$$
$$= \begin{pmatrix} \frac{1}{5}(3 + 2\sqrt{21}) & 0 & 0 & 0 \\ 0 & \frac{1}{5}(-3 + 2\sqrt{21}) & 0 & 0 \\ 0 & 0 & \frac{1}{15}(3 + 2\sqrt{21}) & 0 \\ 0 & 0 & 0 & \frac{1}{15}(-3 + 2\sqrt{21}) \end{pmatrix},$$

$$B_l = \Delta m_l \begin{pmatrix} 2 + \sqrt{3/7} & -2 + \sqrt{3/7} & 0 & 0 \\ (14 + \sqrt{21})/7 & 2 - \sqrt{3/7} & 0 & 0 \\ 0 & 0 & -(14 + \sqrt{21})/21 & -(-14 + \sqrt{21})/21 \\ 0 & 0 & (14 + \sqrt{21})/21 & (-14 + \sqrt{21})/21 \end{pmatrix}$$

As an example we calculate the disorder average of a single term

$$\langle B^{11} B^{11} \rangle = \langle \Delta m^2 \rangle (2 + \sqrt{3/7})^2 \approx 7.047 \ \sigma^2,$$

where $\Delta m$ is gaussian distributed with standard deviation $\sigma$. Finally, the evaluation of the weak disorder expansion (6.83) applied to the minimal model yields

$$\gamma_1 \approx \log(\lambda_1) - \alpha_1 \sigma^2 + \alpha_2 \sigma^4$$
$$\gamma_2 \approx \log(\lambda_2) + \alpha_1 \sigma^2 - \alpha_2 \sigma^4$$
$$\gamma_3 \approx \log(\lambda_3) - \alpha_1 \sigma^2 + \alpha_2 \sigma^4$$
$$\gamma_4 \approx \log(\lambda_4) + \alpha_1 \sigma^2 - \alpha_2 \sigma^4 \ ,$$

with $\alpha_1 = 25/42$ and $\alpha_2 = 625 \left( 43\sqrt{21} - 504 \right)/148176$.

The latter result can be directly compared to our numerical results. We calculated Lyapunov exponents for the transfer matrix (6.68) numerically with Gaussian distributed random mass at the neutrality point. Figure 6.14 shows all four

Lyapunov exponents compared to the weak disorder expansion exhibiting a good agreement up to $\sigma \approx 0.3$. Additional results are presented in figure 6.15, where we compare the numerical results of the smallest Lyapunov exponent with second and fourth order expansion. As one can see, the fourth order expansion is significantly better and nearly identical with the numerical data up to $\sigma \approx 0.3$ .
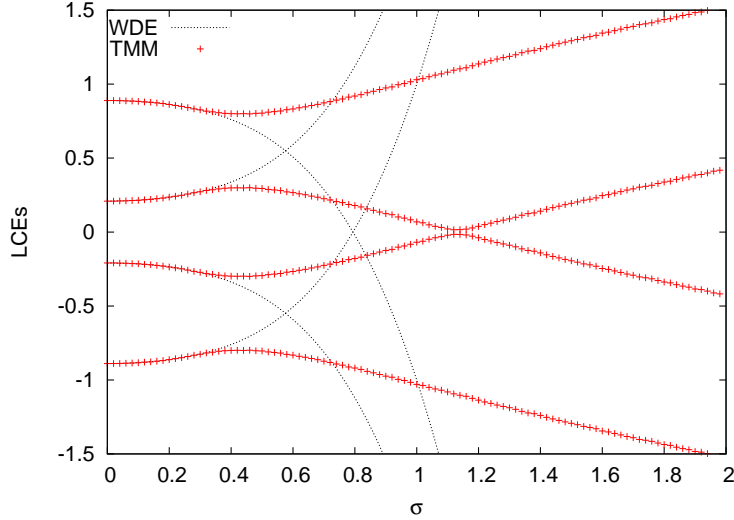


**Figure 6.14.:** Lyapunov exponents for Gaussian random mass compared to the weak disorder expansion in $\sigma$

In section 6.2 we have shown that the energy dispersion of model $A$ is not symmetric in $m$. In order to study the influence of this asymmetry in the disordered case, we calculate $\gamma_{min}$ for the minimal model and $(k_y = 0)$ as a function of $\bar{m}$ and disorder strength. The result is shown as a density plot in figure 6.16 which points out that due to the asymmetry in $m$ the minimum of $\gamma_{min}$ is shifted to negative values of $\bar{m}$. Without disorder $\sigma = 0$ we see the expected minimum at $\bar{m} = 2\delta$ which is also shifted for bigger disorder. Expressions for $\gamma_i(m, \sigma)$ in the weak disorder expansion are given by

$$\gamma_1 \approx \log(\lambda_1) - \sigma^2 \, \frac{1}{2u^2} + \sigma^4 \, \frac{9 - 24 \left(u - m^2 + m(1 - 2u)\right)}{16(2m - 1)u^5} \tag{6.85}$$

$$\gamma_2 \approx \log(\lambda_2) + \sigma^2 \, \frac{1}{2u^2} + \sigma^4 \, \frac{9 - 24 \left(u - m^2 + m(1 - 2u)\right)}{16(2m - 1)u^5} \tag{6.86}$$

$$\gamma_3 \approx \log(\lambda_3) - \sigma^2 \, \frac{1}{2u^2} - \sigma^4 \, \frac{9 - 24 \left(u - m^2 + m(1 - 2u)\right)}{16(2m - 1)u^5} \tag{6.87}$$
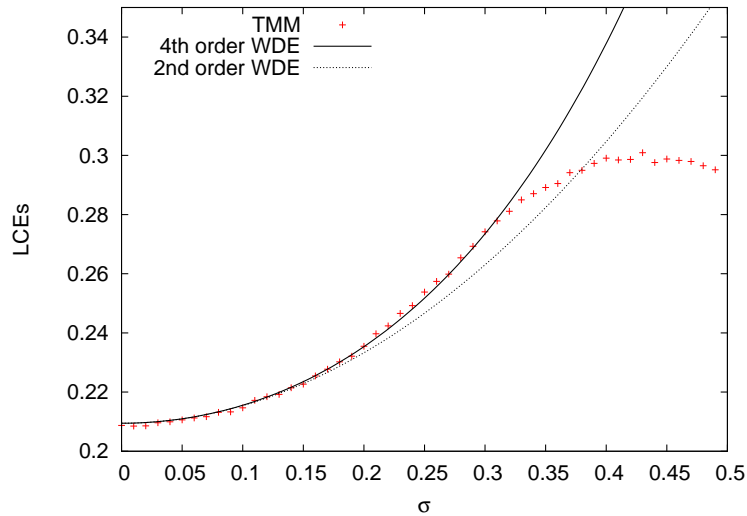
**Figure 6.15.:** Smallest positive Lyapunov exponent compared to weak disorder expansion in second and fourth order. Red crosses are calculated with the transfer matrix method.

$$\gamma_4 \approx \log(\lambda_4) + \sigma^2 \, \frac{1}{2u^2} - \sigma^4 \, \frac{9 - 24 \left( u - m^2 + m(1 - 2u) \right)}{16(2m - 1)u^5} \tag{6.88}$$

with

$$u^2 = 1 + (m - 1)m.$$

Figure 6.17 shows the numerical results for fixed $\sigma$ as a function of $\bar{m}$ compared to the weak disorder expansion. Again, for stronger disorder the second order expansion deviates and fourth order is needed. Nevertheless, the shifted minimum of $\gamma_{min}$ can be seen in both orders of the perturbation theory. Additionally, we have compared the weak disorder expansion for negative $\bar{m}$ as function of disorder to ensure validity (cf. figure 6.18). Because the results from the weak disorder expansion suggests that the Lyapunov exponent acquires zero, we checked if the minimum of $\gamma_{min}$ converges to zero at $\sigma = 0.3$ by increasing the accuracy and the number of data points in vicinity of this point. According to the results, we have to conclude that $\gamma_{min}$ acquires a finite value and thus Dirac fermions are localized for this model. Notice that we can not extrapolate to the two dimensional case. The smallest Lyapunov exponent in this model is independent of system size but we expect that if randomness is in each lattice point this assumption is no longer valid. Consequently, we can not perform finite size scaling.

Before we go on with model $A$ in two dimensions we like to introduce a further discretization method of the Dirac equation.
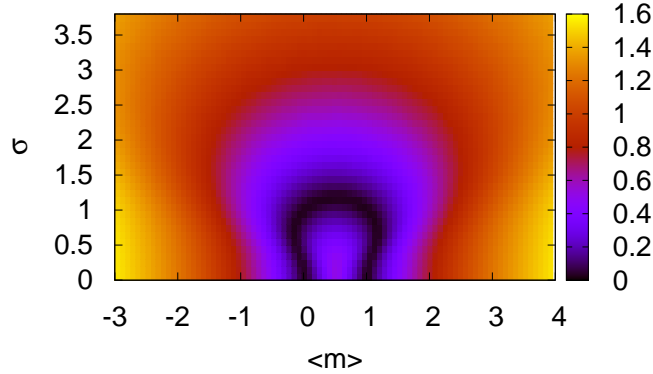
**Figure 6.16.:** Smallest Lyapunov exponent as a function of $\bar{m}$ and $\sigma$.

### 6.2.3. Non-symmetric discretization – model $B$

In this section we comment on the discretization of the Dirac equation introduced in Ref. [67], which we refer to as model $B$. Their approach follows the method of Stacey [69] to avoid fermion doubling, but is extended to a scalar potential and random mass [39] in two spatial dimensions. In what follows we like to outline the main idea in one dimension and then present results for the transfer matrix in two dimensions and refer to Refs. [39, 67] for more details.

The non-symmetric discretization of the differential operator is given by

$$\partial_x \approx \frac{1}{\Delta}(\psi_{l+\Delta} - \psi_l) \tag{6.89}$$

and obviously, the resulting Hamiltonian matrix is not hermitian. Recognizing that the latter discretization defines the derivative at the point $l + \Delta/2$ the Dirac equation for this discretization has to be changed

$$-i(\psi_{l+1} - \psi_l)\sigma_1 = E\psi_{l+1} \tag{6.90}$$

since $\psi$ and $\partial_x\psi$ have to be defined in the same point. Now the lattice has either to be shifted or equivalently the wave function itself has to be averaged

$$\psi_{l+\Delta/2} = \frac{1}{2}\{\psi_{l+\Delta} + \psi_l\}. \tag{6.91}$$

We set $\Delta = 1$ and acquire for the Dirac equation in one spatial dimension

$$-\{\psi_{l+\Delta} - \psi_l\}\sigma_1 = E\frac{1}{2}\{\psi_{l+\Delta} + \psi_l\}. \tag{6.92}$$
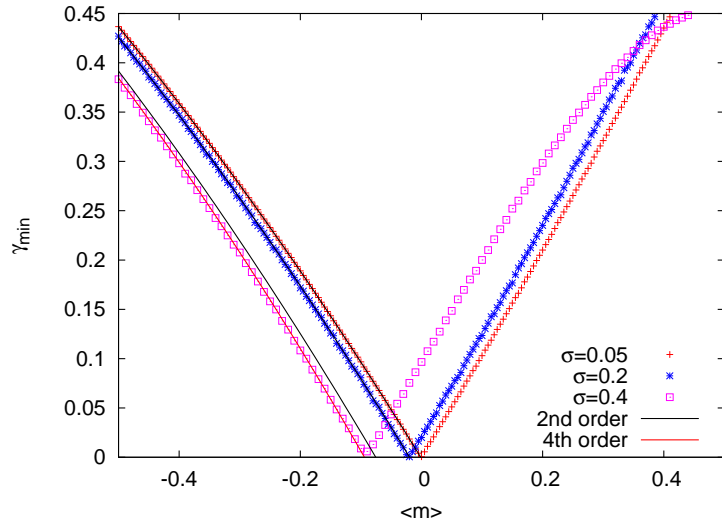
**Figure 6.17.:** Smallest Lyapunov exponent as a function of $\bar{m}$. The minimum is shifted to left for increasing disorder.

The resulting Hamiltonian matrix is hermitian. Fourier transformation in one dimension leads to the energy dispersion

$$E \propto \pm |\tan(k_x)| \,.$$

In two dimensions with uniform gap the latter is given by

$$E = \pm\sqrt{\tan(k_x/2)^2 + \tan(k_y/2)^2 + (m/2)^2}, \qquad (6.93)$$

exhibiting only one Dirac cone in the center of the Brillouin zone. Thus, by recognizing that the chosen discretization is defined between lattice points and then shifting the lattice, both problems (i.e. non-hermiticity and fermion doubling) are cured at the same time. Notice that in contrast to model $A$ where the bandwidth is finite the bandwidth of model $B$ diverges at the borders of the Brillouin zone. The idea of Stacey can now be adapted to derive the a transfer matrix.

**Transfer matrix**

Recalling Ref. [67] we start from the two dimensional Dirac equation (6.35). We include a scalar potential $U$ which couples to $\sigma_0$, isolate the derivative with respect to $x$, multiply from left with $\sigma_1$ and obtain

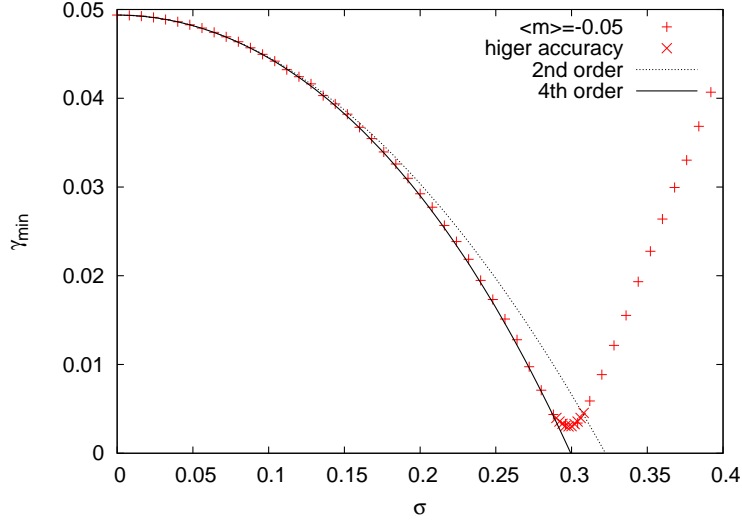$$\sigma_0 \partial_x \psi = (-i\sigma_3 \partial_y - i\sigma_1 V)\psi \,, \qquad (6.94)$$

**Figure 6.18.:** Smalles Lyapunov exponent for the minimal model compared to the weak disorder expansion.

where $V = U - E$. At this point we use the discretization introduced above and write the Dirac equation as

$$\frac{1}{2\Delta}\sigma_0 \mathcal{J}(\psi_{l+1} - \psi_l) = \left(-\frac{1}{2\Delta}\sigma_3 \mathcal{K} - \frac{i}{4}\sigma_1 \mathcal{V}^{(l)}\right)(\psi_l + \psi_{l+1}) \qquad (6.95)$$

with the help of matrices $\mathcal{J}$, $\mathcal{K}$, $\mathcal{V}$ which have only non-zeroo elements for

$$\mathcal{J}_{n,n} = 1, \qquad\qquad \mathcal{J}_{n,n+1} = \mathcal{J}_{n,n-1} = \frac{1}{2}, \qquad (6.96)$$

$$\mathcal{K}_{n,n+1} = \frac{1}{2}, \qquad\qquad\qquad \mathcal{K}_{n,n-1} = -\frac{1}{2}, \qquad (6.97)$$

$$\mathcal{V}_{n,n-1} = \frac{1}{2}V_{l,n-1}, \qquad \mathcal{V}_{n,n+1} = \frac{1}{2}V_{l,n}, \qquad \mathcal{V}_{n,n} = \frac{1}{2}(V_{l,n} + V_{l,n-1}), \qquad (6.98)$$

where $l = 1, 2, .., L$ for the $x$-direction and $n = 1, 2, ...M$ for the $y$-direction with $L$ being the number of multiplications and $M$ the strip width. The boundary conditions are chosen to be periodic in $y$-direction. The transfer matrix is then obtained from

$$\psi_{l+1} = \mathcal{T}_l \psi_l \qquad (6.99)$$

and reads

$$\mathcal{T}_l = \left(\mathcal{J} + i\sigma_3 \mathcal{K} + \frac{i\Delta}{2}\sigma_1 \mathcal{V}^{(l)}\right)^{-1} \left(\mathcal{J} - i\sigma_3 \mathcal{K} - \frac{i\Delta}{2}\sigma_1 \mathcal{V}^{(l)}\right). \qquad (6.100)$$

In particular, this choice of the transfer matrix restricts $M$ to odd numbers because otherwise $\mathcal{J}$ is not invertible. By replacing $i\Delta\sigma_1\mathcal{V}^{(l)}/2$ with $v^2\sigma_2\mathcal{M}^{(l)}/2$ one obtains the corresponding transfer matrix for random mass [39].

### 6.2.4. Comparison of model $A$ and $B$ without disorder

The introduced models share the same property, namely that the momentum dependence of the dispersion is linear for low energies. Thus both models are supposed to describe the behavior of Dirac fermions. At the same time they exhibit essential differences already at the level of zero disorder, which we like to point out here.

Let us first compare the energy dispersions for uniform gap, repeated here

$$\begin{aligned}
E^2 &= k_x^2 + k_y^2 + m^2 & \text{continous} \\
E^2 &= \sin(k_x)^2 + \sin(k_y)^2 + (m + \delta(\cos(k_x) + \cos(k_y)))^2 & \text{model } A \\
E^2 &= \tan(k_x/2)^2 + \tan(k_y/2)^2 + (m/2)^2 & \text{model } B\,.
\end{aligned}$$

To provide an easy understanding we present the energy dispersions again in a single figure 6.19. Every plot is labeled either with $A$ or $B$ according to the respective model. Fermion degeneracy is removed from the outset in model $B$ but singularities are present at the edge of the Brillouin zone, whereas in model $A$ the fermion degeneracy can be tuned via the parameter $\delta$. This opens a gap only at the outer nodal points and the overall gap can be tuned by $m$ separately. If $m = 2\delta$ ($m = 4\delta$) then the outer gaps close at symmetry point $M$ ($X$) and massless fermions reappear.
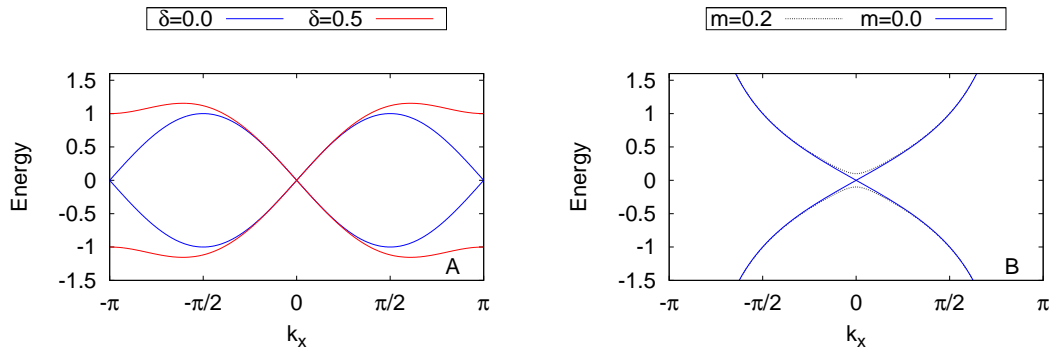


**Figure 6.19.:** Comparison of the two energy dispersions arising from different methods of discretization. Left: Energy dispersion (6.41) for $\delta = 0$ (blue line), $\delta = 0.5$ (red line). Right: Energy dispersion (6.93) without gap (blue line) and $m = 0.2$ (black dashed line).

For a clean system, wave functions are plain waves and therefore $\psi \propto \exp(ik_x x + ik_y y)$. If we assume a rectangular sample periodic in $y$- and extended in $x$-direction, $k_x$ is determined by the dispersion and $\Im(k_x)$ can be identified with the Lyapunov exponent (cf. equation (4.12)). We resolve the energy dispersions for $k_x$ at $E = 0$ and obtain for the continuous model

$$k_x = i\sqrt{k_y^2 + m^2}\,, \tag{6.101}$$

for model $A$

$$k_x = \pm \arccos\left[\frac{1}{2\delta^2 - 2}\left(\,2\delta^2[2 - \cos(k_y)] - 2\delta m\right.\right.$$
$$\pm \left\{6 + 12\delta^2 - 16\delta m + 4m^2 - 8\delta\cos(k_y)\,[m - 2\delta]\right. \tag{6.102}$$
$$\left.\left.+2\cos(2k_y)\left[2\delta^2 - 1\right]\right\}^{1/2}\right)\right]\,. \tag{6.103}$$

and for model $B$

$$k_x = 2\arctan\left(i\sqrt{\tan(k_y/2)^2 + (m/2)^2}\right)\,, \tag{6.104}$$

Extended states only exist if $\Im(k_x) = 0$. For finite $m$ in the continuous case it follows $\Im(k_x) \neq 0$ as expected and states with energies lying in the gap are not extended. Figure 6.20 shows equation (6.103) for $\delta = 0.5$ in the left panel and equation (6.104) in the right panel. In the right panel it can be seen that $\Im(k_x)$ acquires zero for $k_y = \pi$. In fact, taking the limit in equation (6.104) we obtain
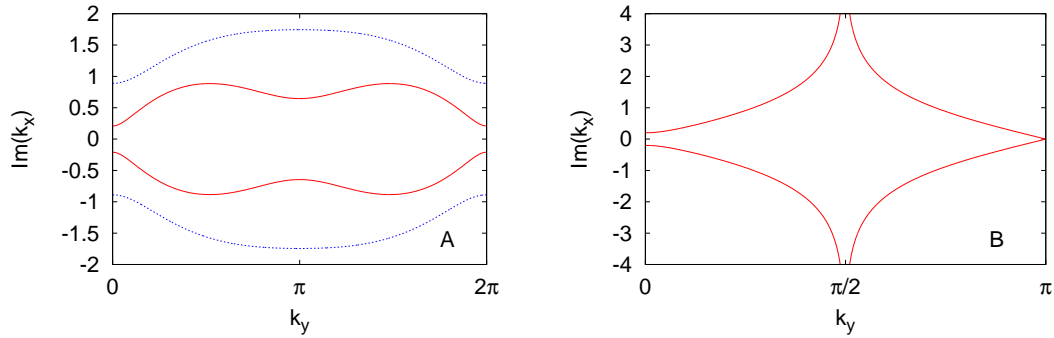


**Figure 6.20.:** Lyapunov exponents for clean systems with uniform gap $m = 0.2$. Plot of Eq. (6.103) for one Dirac cone ($\delta = 0.5$), left panel and Eq. (6.104) in the right panel.

$$\lim_{k_y \to \pi} \left\{ 2i \operatorname{artanh} \left( \sqrt{\tan(k_y/2)^2 + (m/2)^2} \right) \right\} = \pi \,,$$

yielding $\Im(k_x) = 0$ for model $B$ corresponding to an extended state at the Brillouin zone border. On the one hand, from the physical point of view this is not a problem at all, since the model is only valid for small energies and thus for small wave vectors. On the other hand, from the numerical point of view we are not able to distinguish $k_y = 0$ from $k_y = \pi$ because the transfer matrix method gives all Lyapunov exponents in an ordered sequence from which we choose the smallest one. Additionally, we saw that for $\delta = 0.5$ and $m = 2\delta$ or $m = 4\delta$ massless fermions appear again. Thus, the Lyapunov exponent as a function of $m$ has a additional roots.

For comparison with numerical results, we calculate $k_x$ for finite strip widths $M$ and take $k_y = 2\pi n/M$. Subsequently we sort $k_x$ from (6.104) and (6.103) in ascending order and plot them together with the Lyapunov spectrum calculated from the transfer matrix. Note, that in this case we do not need to use the orthonormalization procedure, it is sufficient to calculate the logarithm of eigenvalues. Figure 6.21 demonstrates the results and it can be seen that numerically and analytically calculated Lyapunov exponents are identical. We have, of course, verified that the Lyapunov spectrum obtained by both methods is identical.

Comparing left and right panel in figure 6.21 clearly displays the problem of the root for $k_y = \pi$. The expected gap in spectrum (6.93) is virtually not visible. In fact, $\gamma_{min}$ is not exactly zero because the definition of (6.100) restricts the strip width to odd numbers. For this reason $\gamma_{min} = 0$ appears only in the limit $M \to \infty$.
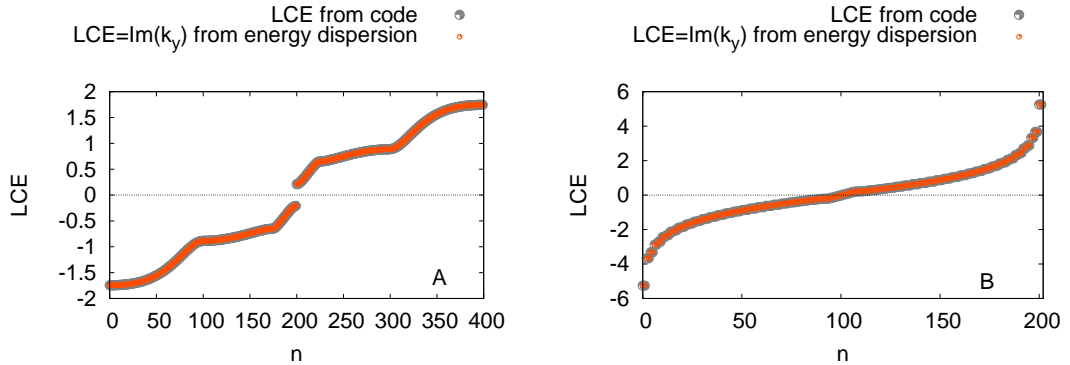


**Figure 6.21.:** Comparison of Lyapunov exponents for clean systems with uniform gap ($\bar{m} = 0.2$). Left: LCE from transfer matrix (6.45) and Eq. (6.103) for one Dirac cone ($\delta = 0.5$) and $M = 200$. Right: LCE from transfer matrix (6.100) and Eq. (6.104) for $M = 201$.

To stress this point we calculated the smallest positive Lyapunov exponent and

the normalized localization length as a function of strip width for a finite gap. From section 6.2.2 on the minimal model we know that $\gamma_{min}$ is non-zero and also independent of $M$, thus the system is insulating.

Figure 6.22 shows the comparison of the normalized localization lengths and the minimum Lyapunov exponent between models $A$ and $B$. It can be seen that the smallest Lyapunov exponent scales to zero $\propto 1/M$ for model $A$, whereas it is constant for model $B$. As expected, for energies lying in the gap, model $A$ shows insulating behavior: The normalized localization length goes to zero with increasing system size. However, the findings for model $B$ contradict this expectation: The normalized localization length is independent of the system size for model $B$. This is equivalent to a minimal Lyapunov exponent going to zero $\propto 1/M$, indicating critical behavior.

Summarizing, we have shown that Dirac fermions without disorder can show either localizing or critical behavior depending on the used model.
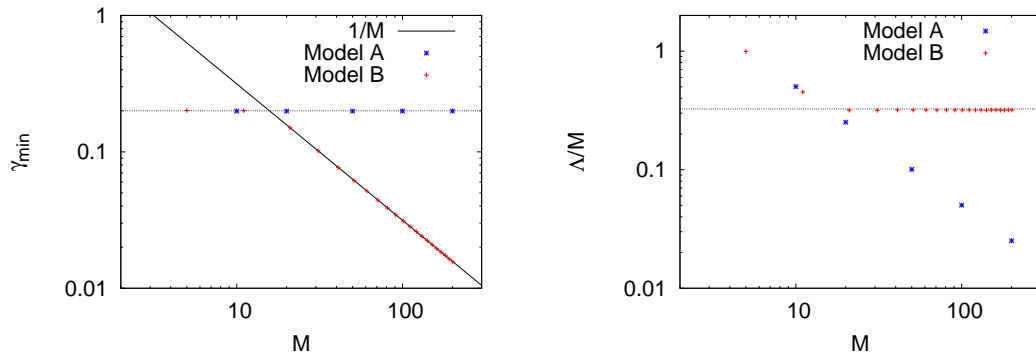


**Figure 6.22.:** Comparison of the two models for a clean system with uniform gap $\bar{m} = 0.2$. Blue points show results for model $A$, red points show results for model $B$. Left: Smallest Lyapunov exponent, right: Normalized localization length.

# 7. Lattice fermions with random gap: Influence of valley symmetry breaking

Now that we have introduced model $A$ and validated its reasonability with several tests we continue by considering two dimensions and random gap. Using the algorithm described in section 4.2, we calculate localization lengths $\Lambda$ by means of transfer matrix (6.45) for several parameter combinations.

## 7.1. Model $A$: Preserved valley symmetry

First, we consider zero average gap ($\bar{m} = 0$) and preserved valley symmetry ($\delta = 0$). In this case we have a four-fold degeneracy of the node structure. If not mentioned explicitly we use box distributed random numbers taken from an interval $[\bar{m} - W/2, \bar{m} + W/2]$ where the corresponding variance is given by $W^2/12$. Furthermore we restrict our calculations to the Dirac point (i.e. $E = 0$).

The left panel in figure 7.1 shows the raw data of the localization lengths. As disorder increases the localization length decreases and the slope decreases with the system size. The exponent in $\Lambda \propto M^\alpha$ is $0 < \alpha < 1$ for all data and thus states are not exponentially localized. If we normalize the raw data by strip width and perform finite-size scaling described before, almost all data points collapse to a single curve cf. right panel in figure 7.1. We had to neglect results below $W \leq 1.6$, suggesting that one-parameter scaling does not hold in this regime. Since $\alpha > 0$ this leads to a divergence of $\Lambda$ for infinite systems and diffusion can not be ruled out (cf. Ref. [64]).

The behavior of $\Lambda$ for a mass with finite mean ($\bar{m} = 0.2$) is more complex as can be seen in the left panel of figure 7.2. For small disorder the localization length converges to a constant value for increasing $M$ indicating $\alpha = 0$. As disorder increases, $\Lambda$ increases too, but remains constant for large $M$. Then there is a transition at $W \approx 2.1$ where $\Lambda$ is growing again with system size but the slope decreases with increasing disorder. To emphasize this point we also present $\Lambda$ as a function of disorder for a single strip width $M = 80$ in the right panel of figure 7.2.
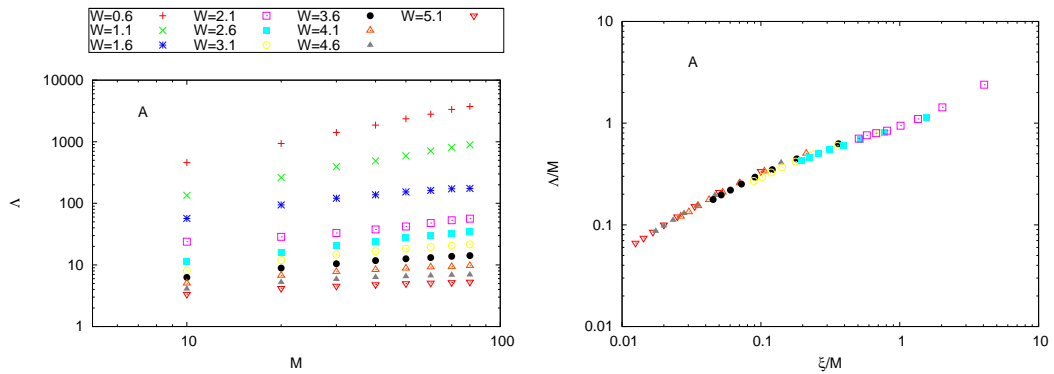
**Figure 7.1.:** Localization length for $\delta = 0.0$ and $\bar{m} = 0.0$ as a function of strip width (left) and the same data after rescaling the length scale with $\xi$ (right). Left: Localization length calculated from Eq. (6.45). Right: Rescaled data without $W = 0.6; 1.1; 1.6$.

This behavior of $\Lambda$ as a function of disorder does not allow to perform single-parameter scaling in the common way. A close look at the data in figure 7.2 (left) shows that neither there is a critical point nor one-parameter scaling seems possible by shifting the curves. Comparing to figure 7.2 (right) two regimes, separated at $W \approx 2.1$, can be distinguished. In both regimes we performed finite-size scaling separately which gives two scaling functions for the infinite system. Rescaling the raw data with the corresponding $\xi$ gives two branches as can be seen in figure 7.3 (left). Additionally, it is very important to recognize that $\tilde{\Lambda}$ is always decaying with system size. Usually this is interpreted as localization. At first sight this behavior seems rather unexpected. On the one hand the raw data shows two regimes. On the other hand the normalized localization length is always decaying with increasing systems.

Our analysis shows a rather unusual behavior, namely that the localization length diverges only when approaching the critical point from $W < W_c$. In order to extract critical quantities on the left from the transition point we fitted our data to

$$\xi(W) \propto |W - W_c|^{-\nu_L} \quad \text{for} \quad 0 < W < W_c. \tag{7.1}$$

The results are gathered in table 7.1 and equation (7.1) is plotted in the right panel of figure 7.3. If we compare the variance $g$ of the critical disorder strength

$$g_c = \frac{W_c^2}{12} \approx 0.387$$

to the gap width $2\bar{m} = 0.4$ we see a good agreement. A possible explanation for this might be that if fluctuations of the random gap are larger then the gap width states can evade exponential localization and diffusive transport is possible. From
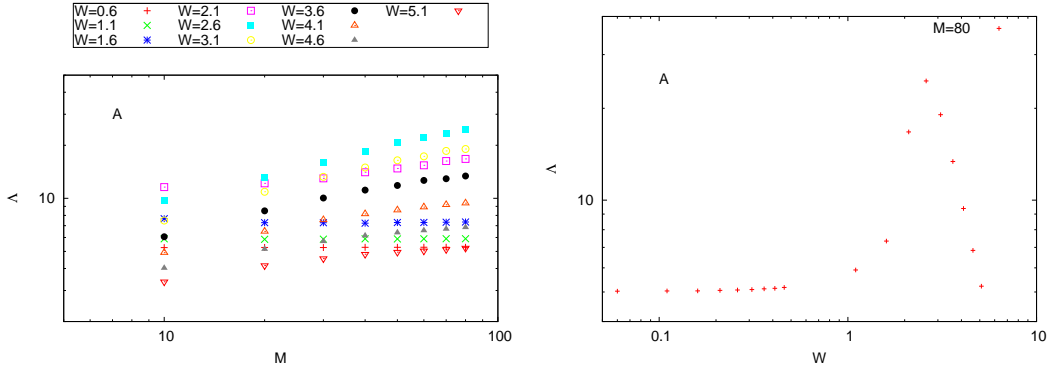
**Figure 7.2.:** Localization length for a gapped system with preserved valley symmetry ($\delta = 0.0$, $\bar{m} = 0.2$) as a function of strip width (left) and as a function of disorder for $M = 80$ (right).

this point of view we can also calculate $W_c$ from the average gap width yielding $\tilde{W}_c = \sqrt{2\bar{m} \times 12} \approx 2.191$. Fitting the data to equation (7.1) with fixed critical disorder results in a slightly different exponent but is also in very good agreement with the numerical scaling function cf. table 7.1. The behavior of $\Lambda \propto M^{\alpha}$ for $\delta = 0$ can be summarized as

$$\begin{cases} 0 < \alpha < 1 & \text{for } \bar{m} = 0 \\ \alpha = 0 & \text{for } \bar{m} \neq 0, \ W < W_c \ . \\ 0 < \alpha < 1 & \text{for } \bar{m} \neq 0, \ W > W_c \end{cases} \quad (7.2)$$

| critical exponents | |
|---|---|
| $\nu \approx 0.289 \pm 0.013$ | $(W_c \approx 2.156 \pm 0.009)$ |
| $\nu \approx 0.332 \pm 0.004$ | $(W_c \approx 2.191)$ |

**Table 7.1.:** Critical values for $\bar{m} = 0.2$ and $\delta = 0$ obtained by fitting $\xi$ with equation (7.1).

## 7.2. Model $A$: Broken valley symmetry

We lift the valley degeneracy by setting $\delta = 0.5$, thus retaining only one Dirac cone in the center of the Brillouin zone at point $\Gamma$.

Contrary to the case of $\delta = 0$, the localization length is not growing with system size if $\bar{m} = 0$. Let us first discuss the unnormalized data. Figure 7.4 (left) shows that for small disorders $\Lambda$ is constant with increasing $M$ but decreases with
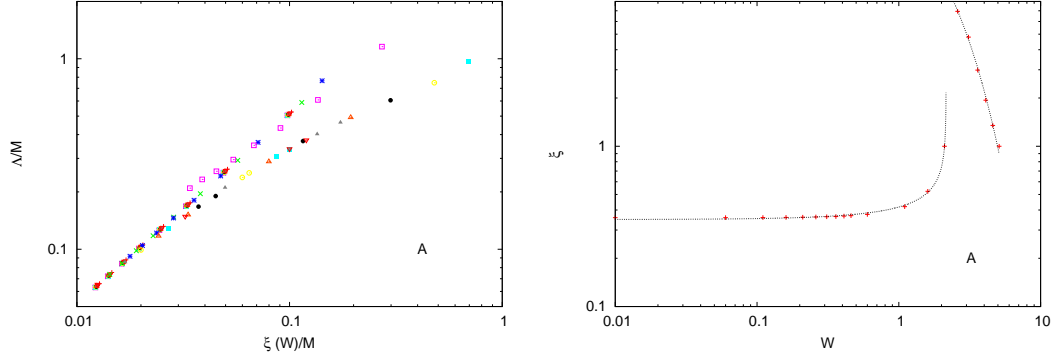
**Figure 7.3.:** One-parameter scaling for $\delta = 0$ and $\bar{m} = 0.2$ (left) and the resulting scaling function $\xi(W)$ (right).

increasing disorder $W$. Then for $W \geq 4.1$, the localization length $\Lambda$ is increasing with system size cf. right panel in figure 7.4.

The normalized data is shown in figure 7.5. To keep the plot illustrative, only a choice of the whole data is shown. What can be seen from the left panel of figure 7.5 is that for small disorder $W < 3.6$ the normalized localization length scales to zero with $M$. For disorder $W > 3.6$ the normalized localization length $\tilde{\Lambda}$ is growing with system size.
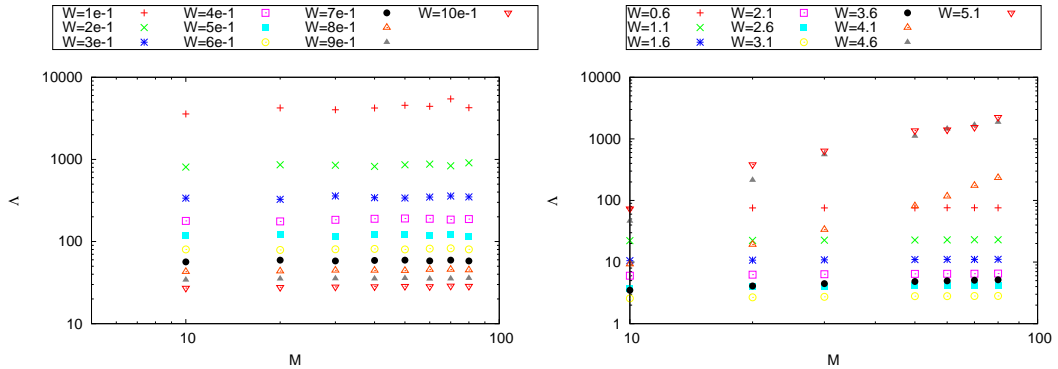


**Figure 7.4.:** Localization length for systems with zero average gap $\bar{m} = 0$ and broken valley symmetry $\delta = 0.5$. Left and right panels represent different disorder ranges.

If we consider $\tilde{\Lambda}$ as a function of disorder (cf. right panel of figure 7.5) we see that there are three regions. Up to $W \approx 3$: $\tilde{\Lambda}$ is decaying, in the region for $3 < W < 5$: $\tilde{\Lambda}$ is increasing and then decreasing again. The growing localization length may be explained as follows. If fluctuations of the random gap are of the order of $2\delta$ corresponding to $W = \sqrt{24\delta} \approx 3.46$, a massless fermion appears. This

means that disorder effectively closes the gap at the border of the Brillouin zone. Consequently, the model shows metallic behavior.
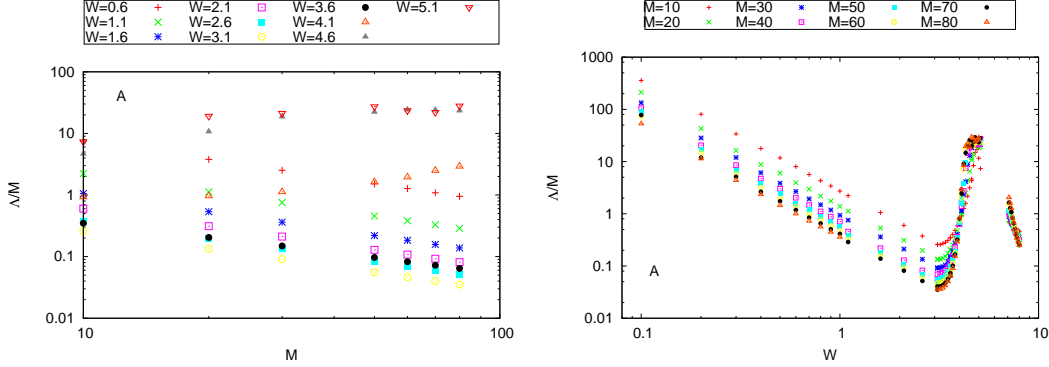


**Figure 7.5.:** Reduced localization length for random gap with zero mean and broken valley symmetry ($\delta = 0.5$ and $\bar{m} = 0$) as a function of system size (left) and disorder (right).

For weak (i.e. $W \lessapprox 4$) and strong disorder (i.e. $W \gtrapprox 7.5$) the behavior is in that sense the same, that the normalized localization length $\tilde{\Lambda}$ is decaying with growing system sizes. Plotting $\tilde{\Lambda}$ over $W$ reveals directly two scale invariant points where different $\tilde{\Lambda}$ are intersecting. These points indicate a metal-insulator transition.

## 7.2.1. Critical exponents for the metal-insulator transition

In order to extract the critical exponent we fitted expression (5.7) with $s = 5$ to our data. The used data and the resulting curves are plotted in figure 7.6 and the critical parameters can be taken from table 7.2. Changing the variables of $\tilde{\Lambda}(M, W)$ from $M$ to $\xi/M$ shifts the raw data onto a single curve shown in figure 7.7. Both plots contain data points for a wider range of $W$ than have been used for the fitting procedure. It is clear that the power-law dependence of the scaling function is only valid in the vicinity of the transition point. This is the reason for the small deviations of some data points with bigger $|W - W_c|$.

An appropriate method to find the scaling function away from the critical points is to minimize the variance of $\ln M - \ln \xi$, as already mentioned. This works well for $0 < W < 3$ and we use $\xi$ to rescale the data. Figure 7.8 (left); shows that all points collapse onto a single curve. Fitting the scaling function as $\xi = cW^{-\beta}$ we get $c \approx 9.1 \pm 0.3$ and $\beta \approx 2.37 \pm 0.02$.

The case of a non-zero average mass needs only a brief discussion since the results and its analysis are qualitatively the same as for $\bar{m} = 0$. The reason for this rather unexpected behavior will be explained later.

| Critical point | I | II |
|---|---|---|
| Exponent $\nu$ | $1.297 \pm 0.031$ | $1.299 \pm 0.066$ |
| $W_c$ | $3.975 \pm 0.002$ | $7.668 \pm 0.008$ |
| $\Lambda_c$ | $0.574 \pm 0.009$ | $0.447 \pm 0.005$ |
| Disorder range | $3.87 \leq W \leq 4.17$ | $7.35 \leq W \leq 7.8$ |
| System sizes | $20 \leq M \leq 80$ | $30 \leq M \leq 80$ |

**Table 7.2.:** Critical values for $\bar{m} = 0$ and $\delta = 0.5$ obtained from fitting the data to equation (5.7).
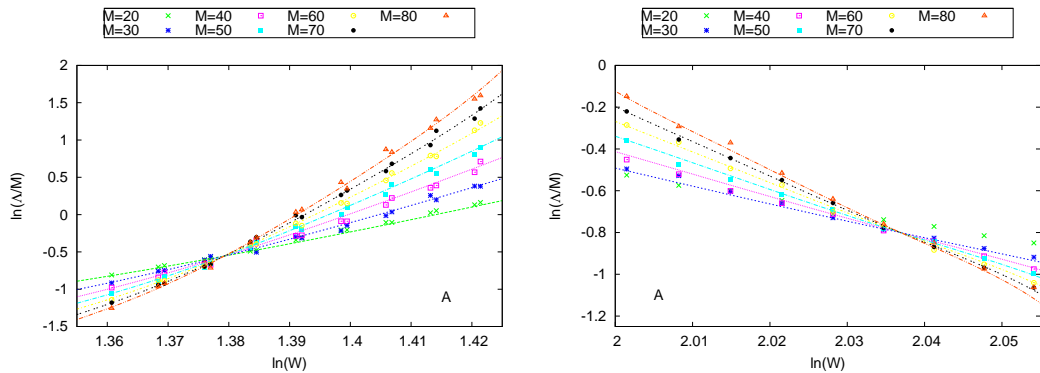


**Figure 7.6.:** Fits to equation (5.7) for $\bar{m} = 0$ and $\delta = 0.5$ around the critical point I (left) and around the critical point II (right).

We have calculated $\Lambda$ for various $M$ and $W$, and present the raw data for $\bar{m} = 0.2$ in the left panel of figure 7.8. The data in the vicinity of the critical points and the resulting fitting curves are shown in figure 7.9. The validity of one-parameter scaling is demonstrated by changing the scale to $\xi/M$ cf. figure 7.10. Increasing the mean of the random mass results mainly in increasing the critical exponent at the second transition point. The other critical quantities remain more or less untouched as can be seen in table 7.3. In addition, we have performed the latter finite-size scaling also for $\bar{m} = 0.8$, but instead of showing the data which looks exactly like for $\bar{m} = 0.2$ we only present the results of the scaling analysis in table 7.4.

**Intermediate conclusion**

So far we have found two critical points where a disorder driven metal-insulator transition occurs. For finite mean of the random gap critical point $I$ can be related to analytical results [37, 38], whereas the transition at point $II$ is most likely due to the finite band width. For zero mean the situation is different: From
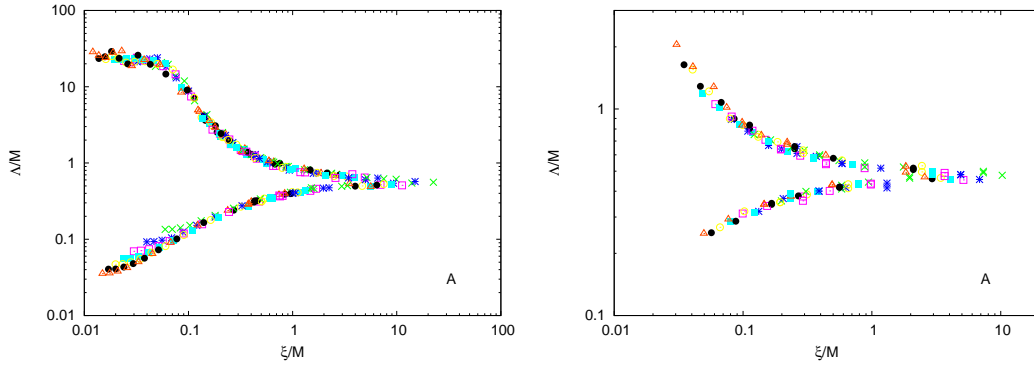
**Figure 7.7.:** Rescaled NLL for $\bar{m} = 0$ and $\delta = 0.5$ around the critical point I (left) and around the critical point II (right). Plots contain more data points than used for the fitting procedure to show the validity of one parameter scaling.

| Critical point | I | II |
|---|---|---|
| Exponent $\nu$ | $1.297 \pm 0.045$ | $1.397 \pm 0.069$ |
| $W_c$ | $3.792 \pm 0.002$ | $7.629 \pm 0.015$ |
| $\Lambda_c$ | $0.591 \pm 0.007$ | $0.517 \pm 0.009$ |
| Disorder range | $3.72 \leq W \leq 3.88$ | $7.1 \leq W \leq 8.0$ |
| System sizes | $20 \leq M \leq 80$ | $20 \leq M \leq 80$ |

**Table 7.3.:** Critical values for $\bar{m} = 0.2$ and $\delta = 0.5$ obtained from fitting the data to equation (5.7).

analytical [37, 38] or numerical [39, 73, 74] calculations one would expect that if $\bar{m} = 0$ there exists a phase boundary where the system is critical. Instead of extended states for zero mean of the random mass our calculations show almost the same behavior as for finite mean. This suggests the absence of such a phase boundary.

To clarify the discrepancy we have to recall the discussion on the energy dispersion of model $A$ and the results for one dimension. We have shown that the model is not symmetric when replacing $m \to -m$ and we also have shown that the minimum of the Lyapunov exponent is shifted to negative $\bar{m}$. Moreover, we have confirmed this shift by means of a perturbation theory in section 6.2.2 but it is also possible to set up an effective model showing the same: A Taylor expansion of the energy spectrum (6.41) at $\mathbf{k} = (0,0)$ for $\delta > 0$ and $0 < m < \delta$ gives

$$E = \pm\sqrt{m^2 + (k_x^2 + k_y^2)(1 - m\delta)}. \tag{7.3}$$

Like in model $A$ the latter is not symmetric in $m \to -m$ and gives rise to define
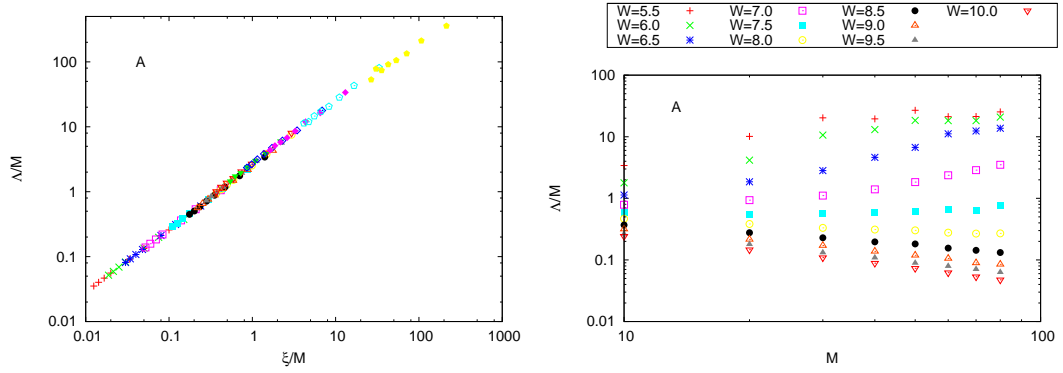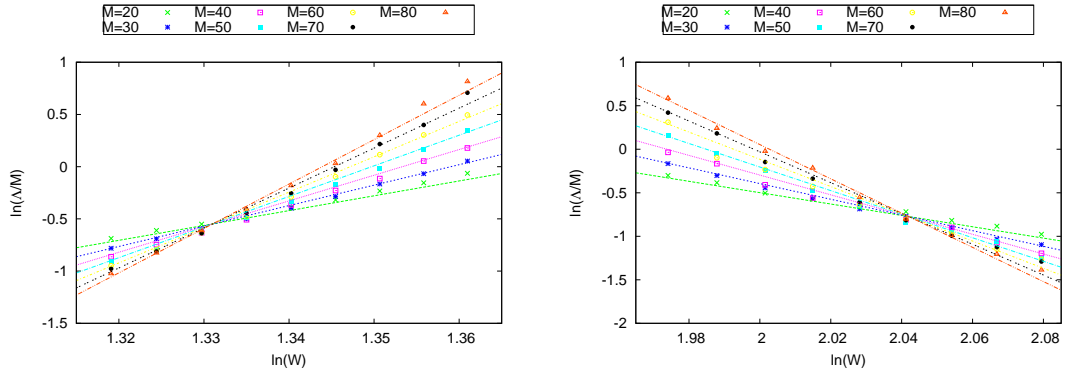
**Figure 7.8.:** Rescaled localization length for $0 < W < 3.1$ for $\bar{m} = 0$ and $\delta = 0.5$ (left) and reduced localization length versus system size for uniform distributed gap with $\bar{m} = 0.2$ and $\delta = 0.5$.



(a) Fitted curves around the critical point I.     (b) Fitted curves around the critical point II.

**Figure 7.9.:** Fits to equation (5.7) for $\bar{m} = 0.2$ and $\delta = 0.5$ indicating phase transitions.

an effective low-energy Hamiltonian

$$H = \sqrt{1 - m\delta} \; k_x \sigma_1 + \sqrt{1 - m\delta} \; k_y \sigma_2 + m\sigma_3. \tag{7.4}$$

As a direct consequence, we see from the low-energy model that considering $m$ as a random variable in the original lattice leads to randomness coupled to all three Pauli matrices. To check whether this model is able to describe the shifted minimum of the Lyapunov exponent, we derive a recurrence equation in one dimension ($k_y = 0$) analogous to section 6.1.1

$$z_{l+2} = M_{l+1} \left( \frac{1}{M_{l+1}} + 4M_l + \frac{1}{M_{l-1}}(1 - z_l^{-1}) \right) \tag{7.5}$$
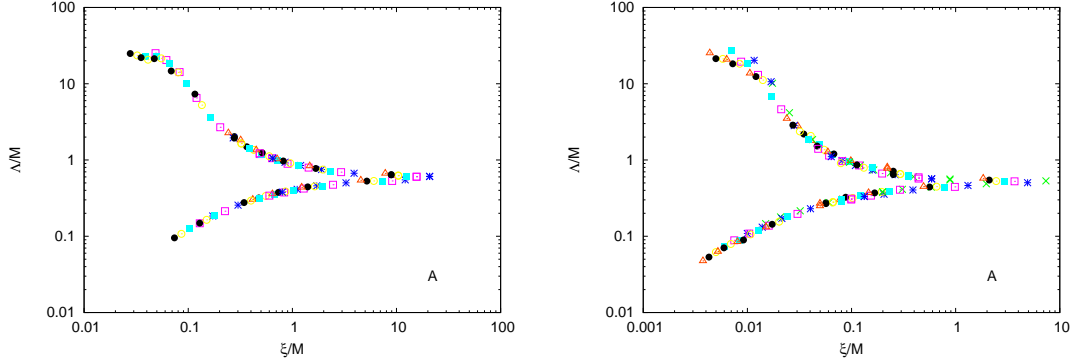
**Figure 7.10.:** Rescaled NLL for $\bar{m} = 0.2$ and $\delta = 0.5$ in the vicinity of critical point I (left) and in the vicinity of critical point II (right).

| Critical point | I | II |
|---|---|---|
| Exponent $\nu$ | $1.217 \pm 0.017$ | $1.451 \pm 0.024$ |
| $W_c$ | $3.047 \pm 0.004$ | $7.727 \pm 0.01$ |
| $\Lambda_c$ | $0.893 \pm 0.013$ | $0.479 \pm 0.007$ |
| Disorder range | $2.7 \leq W \leq 3.33$ | $6.6 \leq W \leq 8.4$ |
| System sizes | $20 \leq M \leq 80$ | $20 \leq M \leq 80$ |

**Table 7.4.:** Critical values for $\bar{m} = 0.8$ and $\delta = 0.5$ obtained from fitting the data to equation (5.7).

with $z_{l+2} = v_{l+2}/v_l$, $M_l = m_l/\sqrt{1 - m_l \delta}$ and calculate the Lyapunov exponent depending on the mean $\bar{m}$. The comparison between $\delta = 0$ and $\delta \neq 0$ is shown in figure 7.11. The minimum of $\gamma_{min}$ is shifted to negative $\bar{m}$.

For this reasons we expect the phase boundary to be curved to negative $\bar{m}$ and dependent on the disorder strength. In order to confirm this assumption and to gain a sharper picture of the phase diagram we calculate $\gamma_{min}$ for a small system as function of disorder $W$ and average gap $\bar{m}$.

Figure 7.12 shows the result for a strip of width $M = 10$ as a color map. The black areas correspond to the minimum of the Lyapunov exponent where we expect the metallic behavior. Whether or not there is a transition, can only be decided from finite-size scaling analysis. In order to investigate the insulator-insulator transition we need to know how the minimum of $\gamma_{min}$ depends on disorder $W$. Therefore we have extracted the minimum for a strip of width $M = 10$ of several $W$ and have fitted this to

$$m_0 = aW^b, \tag{7.6}$$

which gives $a = 0.038$ and $b = 2.006 \pm 0.002$, and allows us to estimate the critical value of $m$.
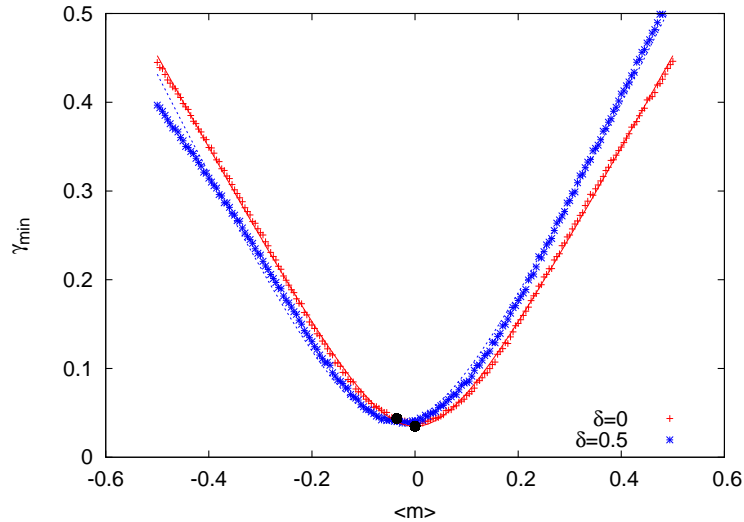
**Figure 7.11.:** Lyapunov exponent for fixed disorder $W = 1$ as a function of $\bar{m}$. Red data points are for $\delta = 0$ and blue points are for $\delta = 0.5$. The black dots are the corresponding minima obtained from fitting.

### 7.2.2. Critical exponent for the insulator-insulator transition

Now that we have an estimation of $m_c$ where the system is expected to be critical we calculate $\gamma_{min}$ for fixed $W$ and various system sizes as a function of $\bar{m}$. Figure 7.14 shows the results in the vicinity of $\bar{m} \approx 0$ and figure 7.15 shows the results in the vicinity of $\bar{m} \approx 2\delta$. It turns out that the minimum of $\gamma_{min}$ is indeed a critical point, thus independent of $M$. We have obtained critical exponents $\nu$ and $m_c$ by fitting the data to

$$z = M\gamma_{min} \propto |\bar{m} - m_c| M^{1/\nu}. \tag{7.7}$$

The critical quantities are gathered in table 7.5 and the critical exponent in vicinity of the three considered points is approximately $\nu \approx 1$.

### 7.2.3. Phase diagram

Let us conclude this section by combining the latter results: We have studied the influence of valley symmetry breaking on lattice fermions with random gap and we have shown that there is a metal-insulator transition for which have calculated the critical exponents using finite-size scaling. Surprisingly, the expected phase boundary separating two insulating regimes depends on the disorder strength. This is owed to the fact that the model is asymmetric in $m$. The explanation for this behavior is that due to the symmetry breaking parameter $\delta$ the random mass term also couples to the wave vector. We have confirmed that the minimum of
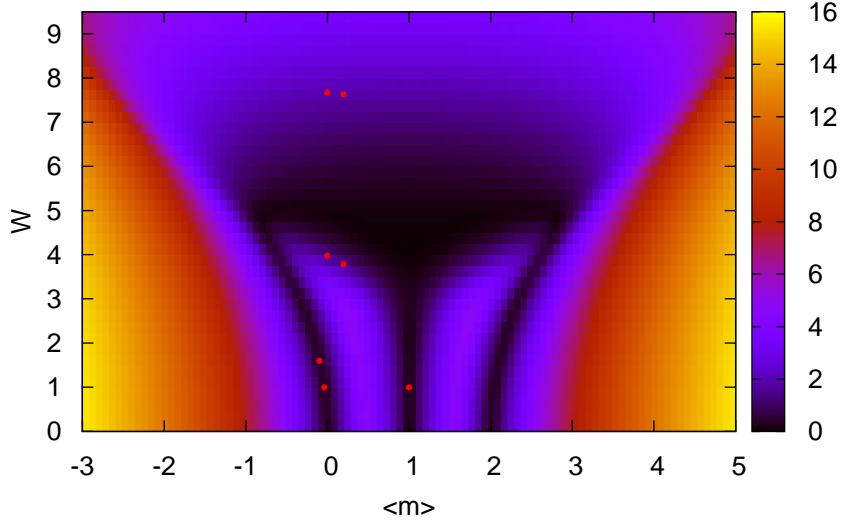
**Figure 7.12.:** Normalized smallest Lyapunov exponent for $M = 10$ and $\delta = 0.5$.
The red points are the critical points obtained from the finite-size
scaling.

$\gamma_{min}$ is shifted by means of the weak disorder expansion in section 6.2.2 and using
an effective low-energy Hamiltonian exhibiting the same behavior. Moreover, we
have shown that model $A$ behaves critical at the phase boundary and calculated
the critical exponent for the insulator-insulator transition at three different points.

The growth of the localization length can again be summarized by discussing
the exponent $\alpha$ in

$$\Lambda \propto M^{\alpha} \text{ with } \begin{cases} \alpha = 0 & \text{for } \bar{m} \neq m_c, \ W < W_{c1} \\ \alpha > 1 & \text{for } \bar{m} \neq m_c, \ W_{c1} < W < W_{c2} \\ 0 < \alpha < 1 & \text{for } \bar{m} \neq m_c, \ W > W_{c2} \\ \alpha = 1 & \text{for } \bar{m} = m_c \text{ or } W = W_{c1,c2} \end{cases}. \tag{7.8}$$

Finally, our extensive study of the introduced model leads to the phase diagram
by combining figure 7.12 and the locations of the critical points extracted so far
(cf. figure 7.16). Since the model is symmetric around $\bar{m} = 1$ critical points for
$\bar{m} < 1$ can be mirrored to $\bar{m} > 1$ ($\bar{m} = 0.8$ is equivalent to $\bar{m} = 1.2$).
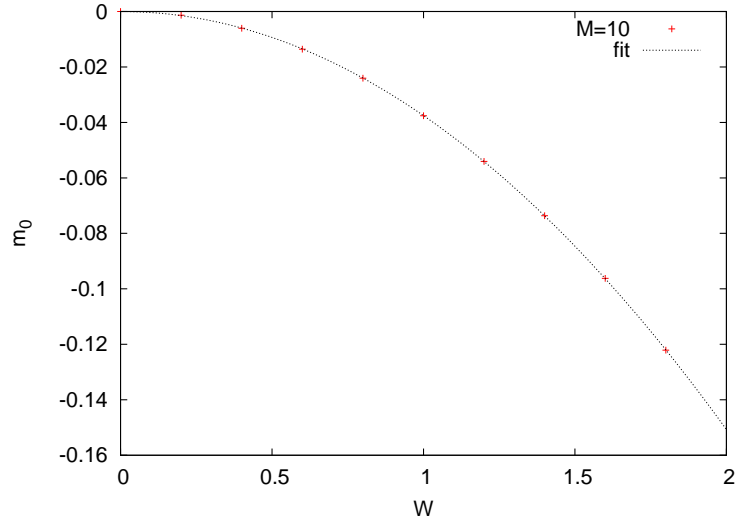
**Figure 7.13.:** Minimum of $\gamma_{min}$ as a function of disorder $W$ the dashed line is a fit to equation (7.6)

| $\bar{m} = 0$: | | |
|---|---|---|
| $W = 1$ | $m_c = -0.037$ | $\nu = 1.019 \pm 0.001$ |
| $W = 1.6$ | $m_c = -0.095$ | $\nu = 1.033 \pm 0.002$ |

| $\bar{m} = 2\delta$: | | |
|---|---|---|
| $W = 1$ | $m_c = 1.00$ | $\nu = 1.006 \pm 0.005$ |

**Table 7.5.:** Critical quantities at the insulator-insulator transition.

## 7.3. Model B

In this section we want to investigate the influence of the random mass on model $B$ and compare results to model $A$.

### 7.3.1. Critical exponent for the insulator-insulator transition

Since our intention is not to reproduce results of Ref. [39] but rather to complement their findings, let us take a closer look at a comparable result. According to the phase diagram proposed in [39, 73, 74], there is an insulator-insulator transition when $\bar{m}$ crosses zero. For disorder strengths smaller then the critical value $W_c$ the system is in the insulating phase and for $\bar{m} = 0$ critical behavior is expected. Thus
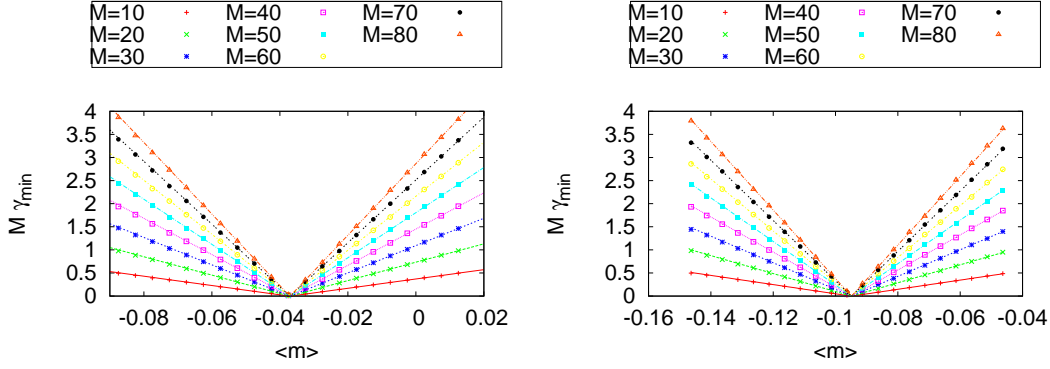
**Figure 7.14.:** Smallest Lyapunov exponent as a function of $\bar{m}$ in vicinity of the first phase boundary $m = 0$. Left panel shows the results for $W = 1$, the right panel for $W = 1.6$.

by fixing $W < W_c$ and calculating $\Lambda$ for various $\bar{m}$ and system sizes, we should be able to extract the critical exponent $\nu$ by fitting

$$z = \frac{M}{\Lambda} \approx z_c + c\,(\bar{m} - m_c)M^{1/\nu} \tag{7.9}$$

to our data. We have done this for two disorder strengths $W = 1.25$ and $W = 2$, and obtained the exponent $\nu \approx 1.03$ which is very close to $\nu = 1.05$ found in Ref. [39], results can be taken from table 7.6.

The data we have used for the fitting procedure is shown in figure 7.17, where we have plotted the data for $W = 1.25$ in gray. As expected, the critical exponent should be the same for all disorder strengths in the insulating regime. Additionally, we neglected the values of $z$ for the smallest two $\bar{m}$. The reason is that we can not see that $z$ goes to zero linearly as $\bar{m}$ approaches zero from our numerical results. Instead we see that for $\bar{m} = 0$ the rescaled Lyapunov exponent acquires a finite value independent of system size which is interpreted as critical behavior.

|  | critical exponents |
|---|---|
| $W = 2$ | $\nu = 1.032 \pm 0.006$ |
| $W = 1.25$ | $\nu = 1.030 \pm 0.006$ |

**Table 7.6.:** Critical exponents for the insulator-insulator transition in model $B$. The used system sizes are: $M = 17, 25, 33, 41, 49, 59, 77$, $m_c \approx 1 \times 10^{-4}$.

Now that we have shown that we reproduce results obtained in Ref. [39] correctly, let us compare both models. Since model $B$ describes a single Dirac fermion we
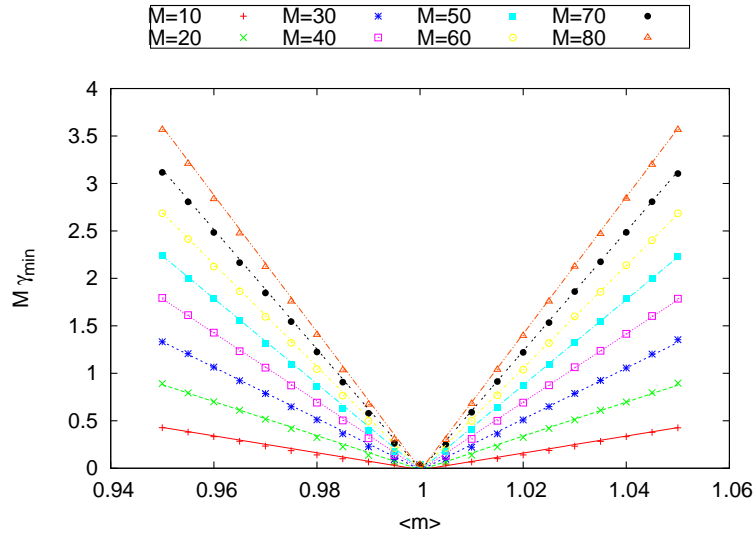
**Figure 7.15.:** Smallest Lyapunov exponent as a function of $\bar{m}$ in vicinity of the second phase boundary $m = 2\delta$ for $W = 1$.

can only compare with results of model $A$ with broken valley symmetry ($\delta = 0.5$). We have calculated the localization length for $\bar{m} = 0.0$, $\bar{m} = 0.06$ and strip widths $M = 11$ to $M = 81$ in steps of 10 using transfer matrix (6.100). Surprisingly, the results shown in figure 7.18 reveal major differences. It turns out that for all disorder strengths considered here, the localization length grows with increasing system size. Only if the mean of the gap is nonzero ($\bar{m} = 0.06$) then $\Lambda$ is almost constant for small disorder but increases again for large system sizes. This means that increasing the system size suppresses exponential localization. A possible reason for this behavior can be found by comparing to the clean case discussed in section 6.2.4. Therefore, it is likely that the smallest Lyapunov exponent becomes that for large wave numbers.

## 7.4. Summary

We have introduced a model for lattice fermions which allows for numerical calculations of the localization length for disordered systems within the framework of the transfer matrix formalism. Using this model it is possible to break the valley symmetry and to compare between one and four nodal points in the Brillouin zone. We have calculated localization lengths for various system sizes and disorder strengths of the random gap.

If the valley symmetry is preserved, the localization length grows with system size but with an exponent smaller than unity (cf. (7.2)). This means that in the
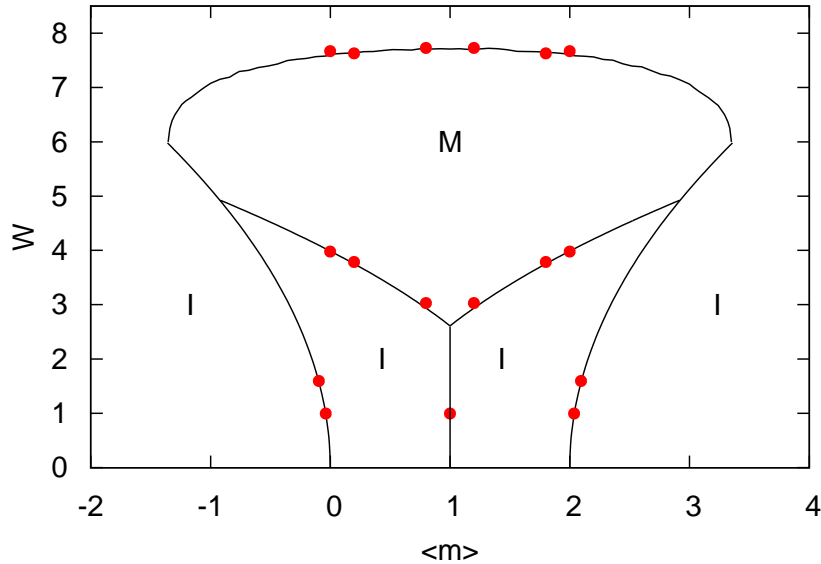
**Figure 7.16.:** Schematic phase diagram for model $A$ with broken valley symmetry. Red points are the critical points obtained from the finite-size scaling.

limit of $M \to \infty$ the localization length diverges. For systems where the mean of the random gap is nonzero we have found that there is a critical disorder strength $W_c$. Below this value states are exponentially localized and the correlation length diverges with power-law when the critical point is reached from $W < W_c$. Using finite-size scaling, we have shown that the rescaled localization length has two branches.

If the valley symmetry is broken, we have found scale invariant points where a metal-insulator transition occurs. For this case we have calculated the scaling function in the vicinity of the critical points, extracted critical exponents and rescaled the data onto a single curve. In addition, we have found that the phase boundary, separating two insulating phases, is curved to negative $\bar{m}$ and have shown that states are critical along this line by calculating the critical exponent at the insulator-insulator transition.

Furthermore, we have compared our results to a different model describing lattice fermions and have shown that there are substantiate differences, although both models show a linear energy spectrum for small wave numbers.
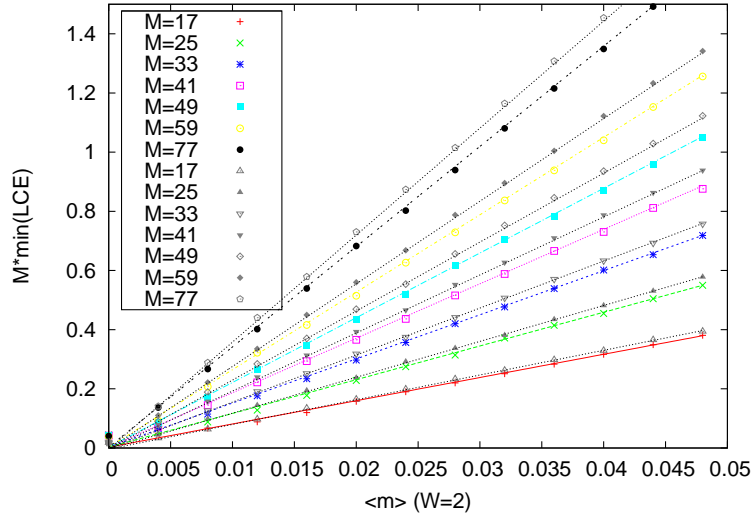
**Figure 7.17.:** Normalized Lyapunov exponents calculated for the model $B$. Data points in color are for distribution width $W = 2$, the gray data is for $W = 1.25$.
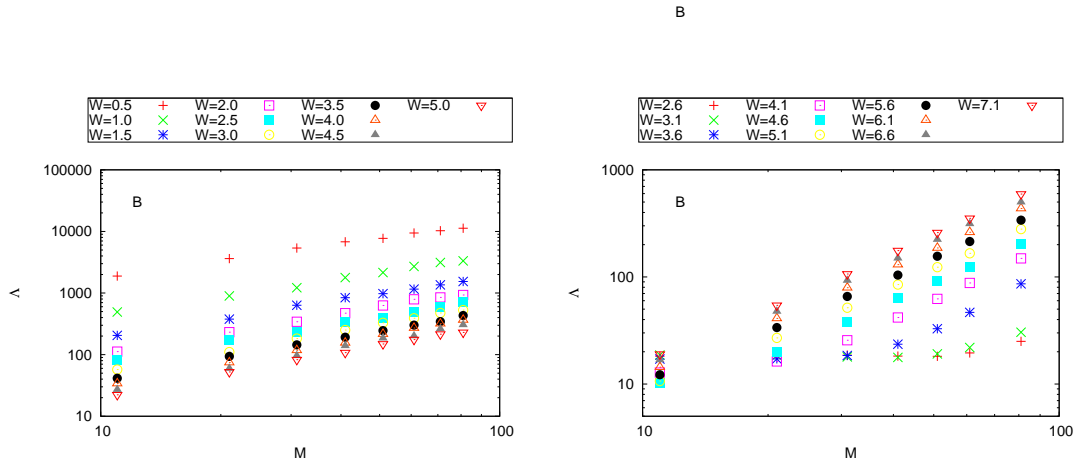


**Figure 7.18.:** Localization lengths calculated from (6.100) for zero mean ($\bar{m} = 0$) of the random gap (left) and for fine mean ($\bar{m} = 0.06$) (right).

# 8. Lattice fermions and the Chalker-Coddington model

In this chapter we like to recall the network model of Chalker and Coddington [18], which is assumed to describe plateau to plateau transitions of the integer quantum Hall effect. We summarize the main ideas of the model and implement its transfer matrix to calculate localization lengths and the critical exponent. A review of the quantum Hall transition can be found in Ref. [17]. Since the network model can be mapped onto the Dirac equation under certain conditions [21, 75] we compare numerical results of the network model with those of model $A$.

## 8.1. Chalker-Coddington network model

Let us briefly review the situation of a quantum Hall experiment [16, 76]. A sample, where a two dimensional electron gas is realized (e.g. AlGaAs), is connected to leads and placed perpendicular into a strong magnetic field. During the experiment, a current is driven along the sample and the Hall voltage across the sample is measured. From this, one can calculate the Hall resistance or the carrier density.

In the classical experiment for high temperatures and low magnetic fields, the Hall resistance grows linearly with magnetic field. For quantum conditions, i.e. low temperatures (a few Kelvin) and high magnetic fields ($\approx 20$ T) the Hall resistance exhibits plateaux.

The energy dispersion of a particle moving in a magnetic field is quantized and the energy levels are called Landau levels. In real samples the density of states in each Landau level is broadened due to disorder and has the shape of a Lorentzian, where states are localized in the center and extended at the edges. When the magnetic field increases the number of states, that fit into one Landau level, increases. The "room" for states grows, so to say, until all states are in a single Landau level. At a plateau, the Hall resistance remains constant with increasing magnetic field as long as states occupy the localized region in one Landau level. When states begin to populate the next Landau level they are extended in the beginning, the Hall resistance increases. When the Hall resistance reaches the next plateau states are again localized. Nowadays, the effect is used to define the electrical resistance standard since the Hall conductance is a multiple of $e^2/h$.
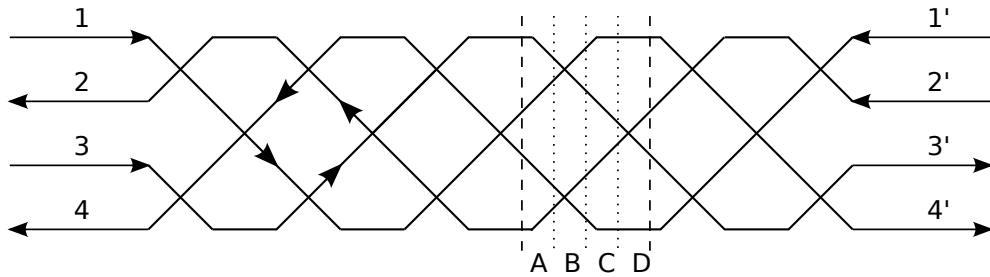
**Figure 8.1.:** Network of the Chalker-Coddington model for $M = 4$, $L = 6$ and strip boundary conditions. Arrows indicate the current flow, amplitudes on the links 1, ..., 4 are connected to 1', ..., 4' by a product of transfer matrices composed of sub–matrices $A$, $B$, $C$, $D$ which are contained between the broken lines.


This transition between plateaux is the starting point for the network model of Chalker and Coddington [18]: Non-interacting electrons in a quantum Hall system move in a varying potential. If the length scale of the varying potential is small compared to the magnetic length $l_c$ then the electron movement can be separated in two components: Rapid cyclotron orbiting at frequency $\omega_c$ and a slow drift of the orbiting center following equipotentials. The network can be described by a lattice composed of nodes, connected each with four links, cf. figure 8.1. The links correspond to equipotentials on which electrons acquire a phase $\phi_i$ according to the arclength. The phases are chosen to be random from the interval $[0, 2\pi]$. The nodes correspond to saddle points of the potential, where electrons can either scatter or tunnel.

It is illustrative to think of a landscape made up of lakes and mountains where the waterline corresponding to the energy is either increasing or decreasing. If the energy is low, electrons are trapped in a lake, for increasing energy it is more likely that more and more lakes join until the water is extended over the whole area. This corresponds to the critical point where electrons are delocalized. For the introduced lattice of nodes and links one can construct a transfer matrix by cutting it into slices. To simplify notation each slice is again split into four pieces. Referring to figure 8.1 this corresponds to the areas between broken lines. The transfer matrix for one slice gets

$$T_\alpha = A_\alpha B C_\alpha D \,, \tag{8.1}$$

where the entries of the sub-matrices can be taken from appendix B.

We have implemented the transfer matrix (8.1) in the present code and have calculated two data sets. One set, shown in figure 8.2 on the left panel, mimics the results of Ref. [18] as a test of the present code. We have performed single

parameter scaling for this data and have plotted the rescaled data in the right panel. All points collapse nicely onto a single curve.
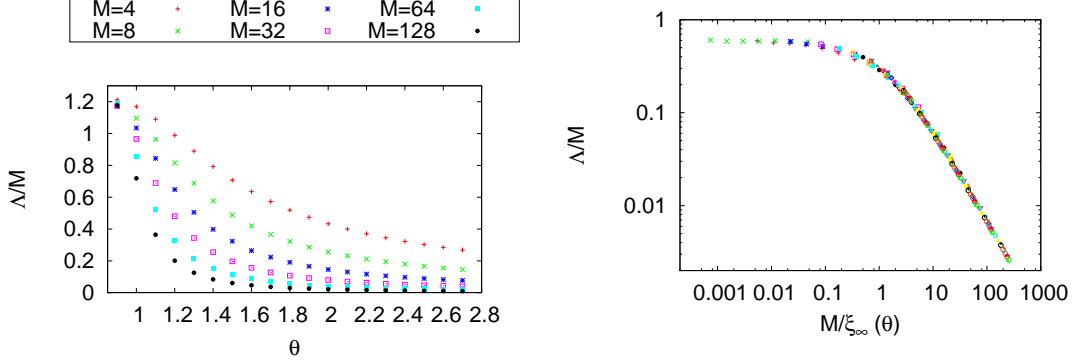


**Figure 8.2.:** Right: Raw data for the CC model, the system is critical at the band center of a Landau level at $\theta_c \approx 0.88$. Left: Rescaled data for the Chalker-Coddington model corresponding to the left panel.

The second set of data, presented in figure 8.3, was calculated in the vicinity of the critical point $\theta_c \approx 0.88$ and is plotted as the normalized Lyapunov exponent $z$. To be precise, the data shows no truly metallic behavior as the localization length never grows faster then the system width, instead the system is critical only in one point $\theta = \theta_c$. For the calculation of the critical exponent we used the second set of data and followed Ref. [77]: As $z$ is an even function around $\theta_c$ the scaling function can be assumed to be of the form

$$z = F(M^{2\mu}x^2)\,, \tag{8.2}$$

with $x = \theta - \theta_c$ and the critical exponent is defined through $\mu = 1/\nu$. Comparing to the scaling function, the curvature at $x = 0$ is proportional to

$$\left.\frac{d^2z}{dx^2}\right|_{x=0} \propto M^{2\mu}\,. \tag{8.3}$$

The latter can be used to calculate the critical exponent. By fitting the data for fixed $M$ to

$$z = z_0 + \sum_{n=1}^{6} A_n(\theta - \theta_c)^n \tag{8.4}$$

the curvature for a certain $M$ can be obtained. Finally, this leads to the critical exponent
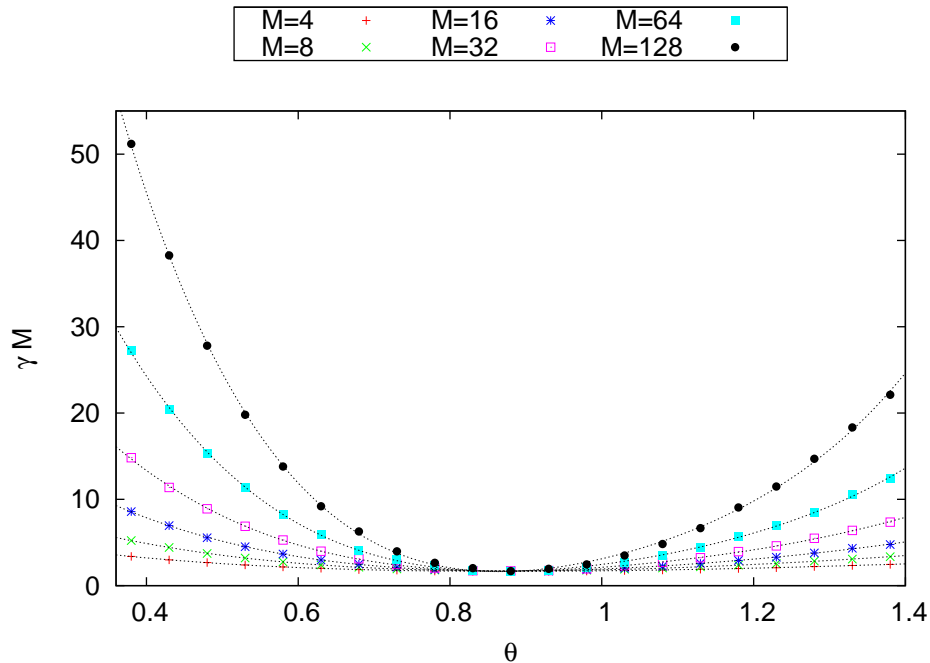
$$\nu = 2.517 \pm 0.1 \tag{8.5}$$

**Figure 8.3.:** Normalized Lyapunov exponent, dashed lines are fits to equation (8.4).

which is slightly smaller but comparable to Refs. [77, 78]. For our calculations we have used smaller systems $M = 4, 8, ..., 128$ and less data points which might be one explanation for the relatively large error. Most groups find critical exponents ranging between $2.3 < \nu < 2.6$ (cf. Ref. [77] for a review of recent exponents). But it is still unclear whether or not the metal-insulator transition between Landau levels is a universal phenomenon or sample dependent.

In addition, we like to point out that computing critical exponents from finite systems using Lyapunov exponents is always an approximation and a delicate issue. Results depend strongly on the method and the range of data that is used. Using the method Chalker and Coddington suggested [18] we obtain a critical exponent which is close to $\nu = 2$. Moreover, we did not consider irrelevant scaling parameters, which take deviations of $z_c$ into account [79] and are supposed to improve the accuracy of critical exponents. In this section we only have intended to use the Chalker-Coddington transfer matrix as another benchmark for our code in order to demonstrate a further method of estimating the critical exponent. As for this transition the localization length is an even function in $\theta$ at the critical point, we may adapt this procedure to similar cases.

Turning now to the next section, we will discuss a special case of model $A$ where we find a transition similar to the latter.

## 8.2. Model A: Broken valley symmetry and scalar disorder

In contrast to the Chalker-Coddington model where the disorder strength is fixed, it is a tunable parameter in calculations for lattice fermions. From the outset it is not clear whether and under which conditions the mapping between both models proposed in Ref. [21] can be confirmed. Therefore, we have tried to find the disorder strength at which a comparable transition occurs. Subsequently, we fix disorder strength and investigate the scaling behavior when changing the energy.

### 8.2.1. Finite-size scaling for the disorder dependence

So far we treated only lattice fermions with random gap, i.e. disorder coupled to the third Pauli matrix. It is natural, also to consider scalar disorder, since it only requires minor changes in the present code.
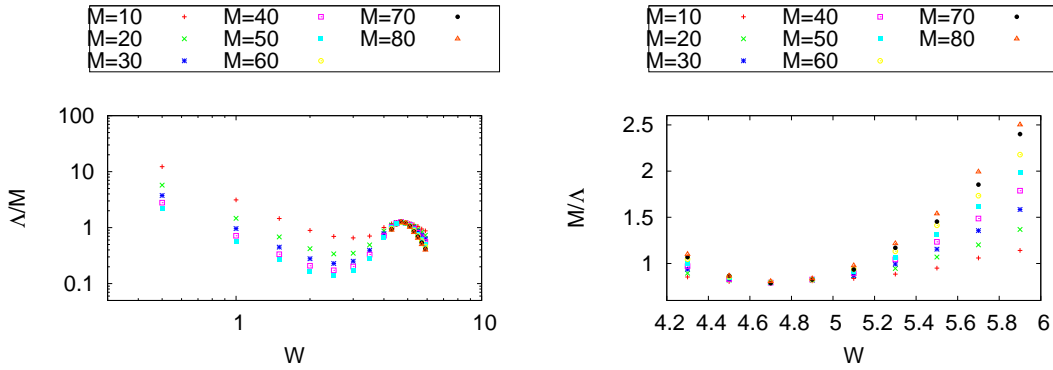


**Figure 8.4.:** Normalized localization length (left) and the normalized Lyapunov exponent (right) as a function of disorder for $\delta = 0.5$ and scalar disorder with $\bar{U} = 0$.

The transfer matrix has been derived in section 6.2 from Hamiltonian (6.50)

$$H = \sigma_1 p_x + \sigma_2 p_y + \delta(\hat{B} - 2)\sigma_3 + U(l, n)\,\sigma_0 \,,$$

with $p_i = -i\hbar\partial_i$. The random numbers $U$ are uniformly distributed and taken from the interval $[\bar{U} - W/2; \bar{U} + W/2]$. We denote the mean value as $\bar{U}$ and the disorder strength as $W$.

Let us consider the case of broken valley symmetry $\delta = 0.5$ and scalar disorder with zero mean ($\bar{U} = 0$). We calculate localization lengths for various system sizes and present them as a function of disorder in figure 8.4. For distribution widths

larger then $W \approx 2.5$, the localization length is growing with disorder and decaying system size, reaching a scale invariant point at $W \approx 4.7$. For stronger disorder the localization length is decreasing, both with system size and disorder strength. This behavior, namely that the system is critical in a single point, appears in model $A$ only for scalar disorder with broken valley symmetry and is reminiscent of the network model.

Plotting the data around the critical point as $z = M/\Lambda$, cf. right panel in figure 8.4 shows similar behavior like in the Chalker-Coddington model (figure 8.3), although the variable is disorder instead of energy. We apply the same method as used for the network model to calculate the critical exponent. This gives

$$\nu = 2.486 \pm 0.108 \tag{8.6}$$

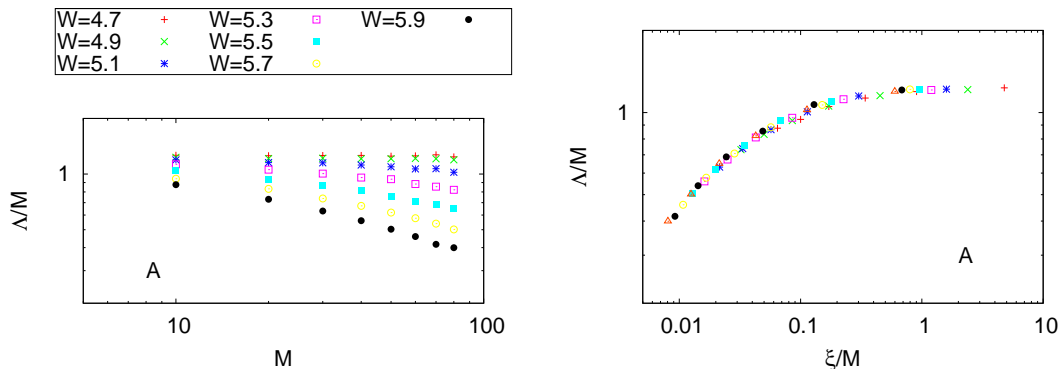which is remarkable close to the result for the Hall transition.



**Figure 8.5.:** Raw (left) and rescaled (right) data for scalar disorder with $\bar{U} = 0$ and broken valley symmetry $\delta = 0.5$.

This might be just a coincidence, but a mapping from the network model to Dirac fermions in two dimensions [21] is known to exist and may justify the comparison. Without going into detail, the mapping results in a Dirac Hamiltonian

$$H = (p_x - A_x)\sigma_1 + (p_y - A_y)\sigma_2 + m\sigma_3 + U\sigma_0 \,,$$

where the randomness in the link phases of the network model translates into randomness in the vector potential, scalar potential and mass. From this point of view model $A$ should give the behavior of the Chalker-Coddington model with disorder in all three potentials. In contrast to this, our results indicate that a critical point of this type only occurs with scalar disorder and broken valley symmetry.

In order to demonstrate validity of single parameter scaling we use the data right of the critical point ($W > 4.7$) for a finite-size scaling analysis. The raw data used for scaling is shown in the left panel of figure 8.5. After rescaling all points collapse onto one single curve cf. right panel in the same figure.

### 8.2.2. Finite-size scaling for the energy dependence

Since we have found a critical point where a disorder driven metal-insulator transition, similar to the Chalker-Coddington model, occurs the next step is obviously to study the energy dependence at this transition. For this reason we have fixed the distribution width to $W = 4.7$ and calculated the Lyapunov exponents as a function of energy. The left panel of figure 8.6 shows the raw data and the result
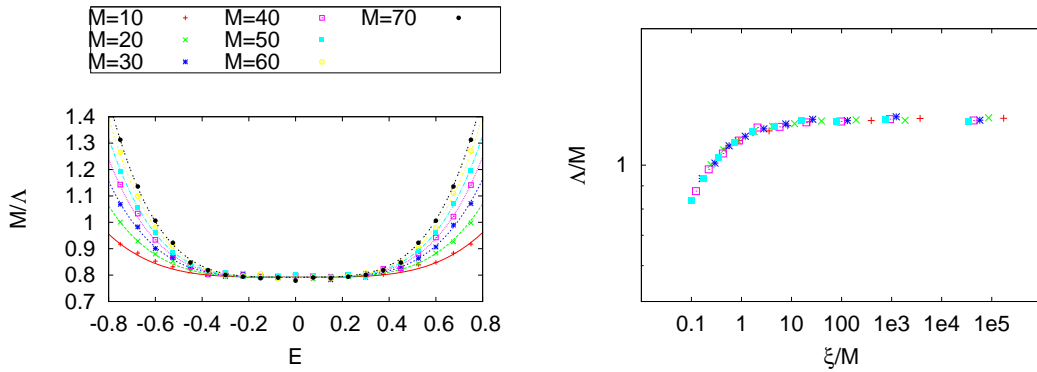


**Figure 8.6.:** Left: Raw data of the rescaled Lyapunov exponent and fitted curves. Right: rescaled data for scalar disorder with $\bar{U} = 0$ and broken valley symmetry $\delta = 0.5$. The distribution width is fixed to $W = 4.7$

of fitting our data to equation (5.7) up to sixth order. From the fitting procedure we have been able to extract the critical quantities at the transition point

$$z_c = 0.792 \pm 0.001 \quad \nu = 5.45 \pm 0.07 \,. \tag{8.7}$$

Assuming a quadratic energy dependence of the scaling function like in equation (8.2) did not lead to a result with satisfying accuracy. If we use a scaling function of the form

$$z = F(M^{4\mu} E^4) \tag{8.8}$$

instead, we obtain a comparable result for the critical exponent of $\nu = 5.40 \pm 0.07$ using the same method described in section 8.1. This form of the scaling function is due to the fact that the leading contribution of the fit is from the fourth order and the latter exponent can be calculated from fitting each data set for fixed $M$ to $\propto E^4$. No smaller or higher order is needed. The resulting power-law behavior of the localization length

$$\xi(E) \approx |E|^{-1/\nu} \tag{8.9}$$

allows to rescale the raw data onto a single curve, cf. right panel in figure 8.5. Although, the critical exponent is notable high, we conclude its correctness from the latter scaling analysis, as we have calculated the critical exponent using two different methods.

## 8.3. Summary

Concluding this chapter, we have recalled the network model supposed to describe the plateau to plateau transition in quantum Hall systems. Typical for such systems is the existence of only one critical point meaning that there is no truly metallic phase since the localization length never grows faster then the system size. We have extracted the critical exponent for the network model and found agreement with present works.

Moreover, we have tried to validate the mapping from the network model to a two dimensional Dirac Hamiltonian by means of lattice fermions. When the transition is disorder driven, we have found an exponent comparable to the Chalker-Coddington model. When driven by energy, the critical exponent is roughly two times larger. In both cases the critical point is a minimum of the Lyapunov exponent and an even function in disorder and in energy.

We have also checked our model for further transitions or metallic phases but only found the described critical point. Unfortunately, our results do not agree with analytical mappings [21, 75], even though we see a similar metal-insulator transition for scalar disorder with broken valley symmetry. The reasons for the discrepancies are not completely clear, but we think, they are a consequence of discretization and its accompanying problems, like fermion doubling. A further explanation might be that there are several approximations made for the mapping from the network model to the Dirac Hamiltonian. Our latter results suggest that both models are different and lattice fermions described by model $A$ do not share the same transition as the Chalker-Coddington model.

# 9. Tight-binding models for lattice fermions with random mass

We have seen in the introduction on graphene that due to the special geometry of the honeycomb lattice the low-energy behavior can be described using the Dirac equation. In this sense graphene (i.e. the honeycomb lattice) serves as a lattice model for Dirac fermions. As a direct consequence of the bisected lattice the energy dispersion has two bands. This observation is crucial for further lattice models since they must be bipartite to exhibit a pseudo spinor structure in the Hamiltonian. In the following we like to introduce two tight-binding models which we then use to calculate localization lengths for finite-size scaling.

## 9.1. Brickwork lattice

The brickwork lattice has already been studied for on-site disorder in Refs. [10, 62] by means of the transfer matrix method. It is topologically equivalent to the honeycomb lattice and can be obtained by removing every second bond in one direction of a simple square lattice. As a consequence, the new lattice is bipartite.

We use the brickwork lattice for our calculations as shown in figure 9.1. This orientation corresponds to a graphene nanoribbon with zigzag edges which is supposed to be metallic. Nanoribbons with armchair edges are either metallic or semiconducting depending on their width. This is due to different boundary conditions. Since we are not interested in transport properties of nanoribbons but to perform a finite-size scaling to make statements on infinite systems, we refer to Refs. [41, 43] as an introduction for further reading.

Figure 9.1 suggests that two different transfer matrices are needed, since only every second column is identical, and periodic boundary conditions are only contained in every second transfer matrix.

In order to derive the transfer matrix for the brickwork lattice let us start with a simple square lattice. The tight-binding Hamiltonian for a square lattice with nearest neighbor hopping reads

$$H = -t \sum_{l,n} \left( c^{\dagger}_{l,n+a} c_{l,n} + c^{\dagger}_{l+a,n} c_{l,n} + \text{H.c.} \right) + \sum_{l,n} \epsilon_{l,n} c^{\dagger}_{l,n} c_{l,n} , \qquad (9.1)$$
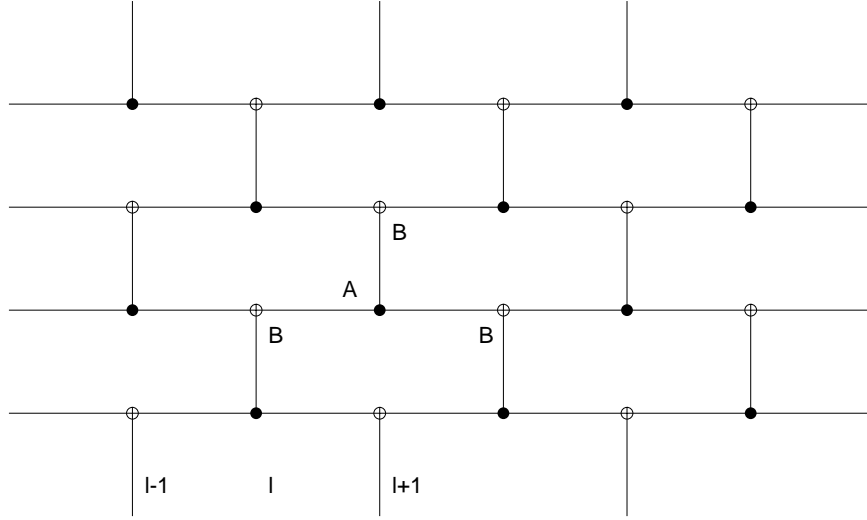
**Figure 9.1.:** Brickwork lattice consisting of two sublattices $A$ and $B$ as it has been used for numerical calculations.

where $t$ is the hopping parameter, $a$ the lattice constant and $\epsilon_{l,n}$ the potential at each lattice site, $c_{l,n}^\dagger$ $(c_{l,n})$ are the creation (annihilation) operators. The index $l$ labels the $x$-direction and accordingly $n$ the $y$-direction. Furthermore, we set $t = 1$ and $a = 1$. From the latter we can construct a transfer matrix in the standard way [2, 7, 9, 10] by separating perpendicular and longitudinal part. The connection between wave function amplitudes is then given by

$$
\begin{pmatrix} A_{l+1} \\ A_l \end{pmatrix} = \begin{pmatrix} \mathbb{1}E - H_l & -\mathbb{1} \\ \mathbb{1} & 0 \end{pmatrix} \begin{pmatrix} A_l \\ A_{l-1} \end{pmatrix} = T_l \begin{pmatrix} A_l \\ A_{l-1} \end{pmatrix}
\tag{9.2}
$$

with

$$
H_l = \sum_{n=1}^{M} \left( \epsilon_{l,n}\, \delta_{n,n} + \delta_{n,n+1} + \delta_{n+1,n} \right) ,
\tag{9.3}
$$

being the Hamiltonian of a perpendicular chain. We have chosen periodic boundary conditions in $y$-direction.

For the brickwork lattice we have to remove every second bond in $H_l$. This gives two transfer matrices $T_l^{odd}$ and $T_l^{even}$ containing the corresponding Hamiltonians

for perpendicular chains. Both matrices have the following structure [10]

$$
H_l^{odd} = \begin{pmatrix}
\epsilon_{l,1} & & & & & & & 1 \\
& \epsilon_{l,2} & 1 & & & & & \\
& 1 & \epsilon_{l,3} & & & & & \\
& & & \epsilon_{l,4} & 1 & & & \\
& & & 1 & \epsilon_{l,5} & & & \\
& & & & & \ddots & & \\
1 & & & & & & \epsilon_{l,M} &
\end{pmatrix}
\tag{9.4}
$$

$$
H_{l+1}^{even} = \begin{pmatrix}
\epsilon_{l+1,1} & 1 & & & & & \\
1 & \epsilon_{l+1,2} & & & & & \\
& & \epsilon_{l+1,3} & 1 & & & \\
& & 1 & \epsilon_{l+1,4} & & & \\
& & & & \epsilon_{l+1,5} & & \\
& & & & & \ddots & \\
& & & & & 1 & \epsilon_{l+1,M}
\end{pmatrix}
\tag{9.5}
$$

and have to be multiplied alternately. In this case periodic boundary conditions are only imposed in $T_l^{odd}$.

## 9.1.1. Scaling behavior with staggered potential

Just like the honeycomb lattice, the brickwork lattice consists of two equivalent sublattices labeled as $A$ and $B$ (cf. figure 9.1). We can break the sublattice symmetry by choosing the opposite sign for the on-site potential on each sublattice ($\epsilon_A = -\epsilon_B$). This is in analogy with introducing a mass term to the Dirac Hamiltonian (cf. section 2.1.1) and we denote the mass as $m = |\epsilon_A|$. Thus, by generating random numbers for one strip of our lattice and changing the sign according to the sublattice we can model lattice fermions with random gap. Comparing to the model $A$ where four nodal points are present, the brickwork lattice exhibits only two nodes within the Brillouin zone. Since the number of valleys is even and time reversal symmetry is preserved, we expect similar results as for the case $\delta = 0$ and $\bar{m} \neq 0$ in section 7.1.

We have calculated the Lyapunov spectrum by means of the transfer matrix approach for uniform distributed random numbers and system sizes up to $M = 200$. Because we have to deal only with real numbers and no spinor structure, we are able to consider larger systems. The raw data for the localization length is presented in figure 9.2. Indeed, calculations show that results from the discretized Dirac equation and from the brickwork lattice are qualitatively the same. Again, there are two regions where the localization length behaves qualitatively different. Up to disorder strengths of $W \approx 2$ the localization length $\Lambda$ is more or less independent

of system size. For stronger disorder the localization length is increasing. We have performed finite-size scaling in the two regions independently and have fitted the resulting scaling function to equation (7.1). From this we have obtained the critical quantities which are collected in table 9.1. The critical exponent is not identical but close to the exponent for the discrete Dirac equation with $\delta = 0$ and $\bar{m} = 0.2$. This suggests, that both transitions are of the same type and may be observed in real graphene samples.
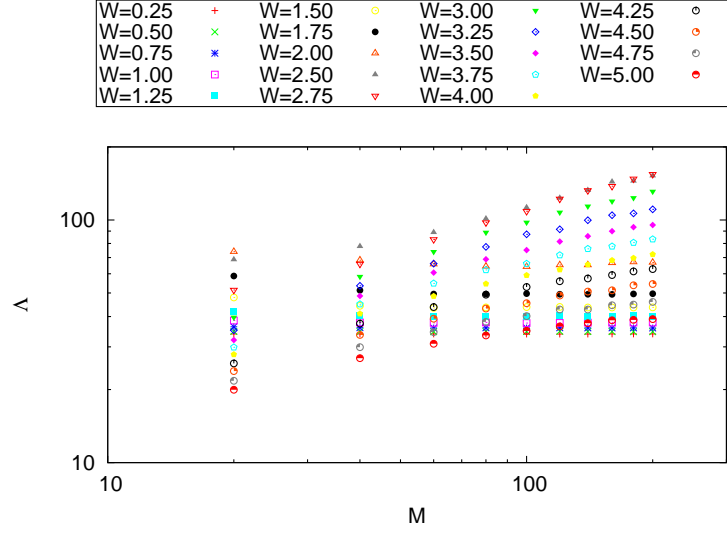


**Figure 9.2.:** Raw data of the localization length for the brickwork lattice with random staggered potential $\bar{m} = 0.06$.

|  | $0 < W < W_c$ |
| --- | --- |
| $W_c$ | $2.123 \pm 0.009$ |
| Exponent $\nu$ | $0.250 \pm 0.007$ |

**Table 9.1.:** Critical values for electrons on a brickwork lattice with random staggered potential.

## 9.2. Scaling behavior for the $\pi$-flux lattice

It is always preferable to have a another model describing the same physical situation. Is there another model where the latter transition can be found? Indeed, the square lattice tight-binding Hamiltonian (9.1) is the basis for a second bipartite

**Figure 9.3.:** Rescaled data (left) and scaling function with fit (right) for electrons on a brickwork lattice. Symbols are identical to those used in figure 9.2.

lattice, the π-flux lattice [80]. If we introduce two different hopping parameters

$$t_x = t \tag{9.6}$$

$$t_y = e^{i\pi n} \, t = (-1)^n t, \tag{9.7}$$
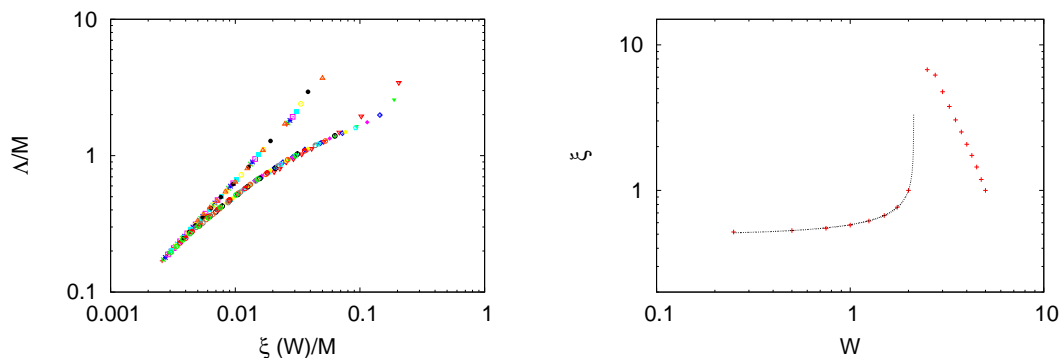
we get

$$H = -t \sum_{l,n} \left( (-1)^n \, c^\dagger_{l,n+a} c_{l,n} + c^\dagger_{l+a,n} c_{l,n} + \text{H.c.} \right) + \sum_{l,n} \epsilon_{l,n} \, c^\dagger_{l,n} c_{l,n} \,. \tag{9.8}$$

By this choice of the hopping parameters the flux through each plaquette is half a flux quantum $h/2e$ and the lattice consists of two sublattices. The free Hamiltonian reads in momentum space [81]

$$\tilde{H} = -t \sum_{k_x, k_x} \psi^\dagger_{\mathbf{k}} \begin{pmatrix} \cos(k_y) & \cos(k_x) \\ \cos(k_x) & -\cos(k_y) \end{pmatrix} \psi_{\mathbf{k}} \tag{9.9}$$

with $\psi_{\mathbf{k}} = (c_{\mathbf{k}} \, \tilde{c}_{\mathbf{k}})$ where $c_{\mathbf{k}} \, (\tilde{c}_{\mathbf{k}})$ is the Fourier transform of the creation operator on lattice sites with odd (even) index $l$. The resulting energy dispersion reads

$$E = \pm\sqrt{\cos^2(k_x) + \cos^2(k_y)} \tag{9.10}$$

and has four Dirac cones in the Brillouin zone. Just like the brickwork lattice the π-flux lattice describes lattice fermions. We derive a transfer matrix in the standard way and perform the same procedure as described for the brickwork lattice. By introducing a staggered potential we are able to consider the case of random gap.

Since we got similar results as for the brickwork lattice, we show only the rescaled data and the scaling function in figure 9.4. Once more we have computed the critical quantities and gathered them in table 9.2. It turns out that critical disorder and critical exponent are slightly larger than for the brickwork lattice.

|            | $0 < W < W_c$     |
| ---------- | ----------------- |
| $W_c$      | $3.236 \pm 0.037$ |
| Exponent $\nu$ | $0.330 \pm 0.022$ |

**Table 9.2.:** Critical values for electrons on a $\pi$-flux lattice with random staggered potential.
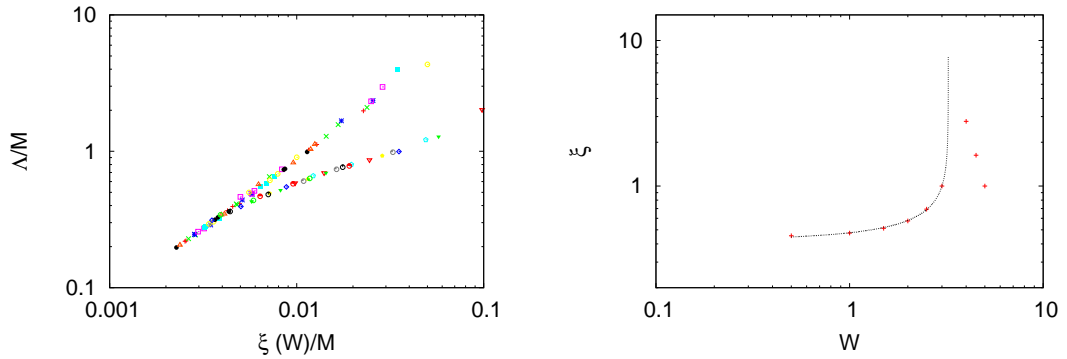


**Figure 9.4.:** Rescaled data (left) and scaling function with fit (right) for electrons on a $\pi$-flux lattice.

## 9.3. Summary

We have applied two well known tight-binding models describing lattice fermions for transfer matrix calculations. By choosing the opposite sign for the random on-site potential on each sublattice we have broken the sublattice symmetry. This is equivalent to the random gap problem. Since the valley symmetry is preserved and thus the node degeneracy is not lifted we have expected that the results should be comparable to the discrete Dirac equation with $\delta = 0$. By means of finite-size scaling of the localization length we have shown that this is indeed the case. For finite mean of the random gap there is a transition from exponentially localized states to probably power-law localized states. The behavior of the localization length for the brickwork and the $\pi$-flux lattice can be discussed by considering $\Lambda \propto M^\alpha$ with

$$\begin{cases} \alpha = 0 & \text{for } \bar{m} \neq 0, \ W < W_c \\ 0 < \alpha < 1 & \text{for } \bar{m} \neq 0, \ W > W_c . \end{cases} \tag{9.11}$$

# 10. Conclusion

Motivated by recent progress in condensed matter physics, in particular the discovery of graphene, we have studied various aspects of disordered lattice fermions in two dimensions.

In the beginning of this thesis we have discussed the emergence of Dirac fermions in graphene and have briefly mentioned other fields where they are present. We have introduced the concept of transfer matrices and applied it to the Dirac equation in one dimension as an elementary but illustrative example. For this purpose we have investigated the transmission through different types of barriers.

Afterwards, we have presented a method to calculate Lyapunov exponents and localization lengths which allows to perform finite size scaling in order to study metal-insulator transitions.

We have discretized the Dirac equation in chapter 6 in one and two spatial dimensions. In one dimension we have derived recurrence equations for the calculation of Lyapunov exponents complementary to the transfer matrix approach. This has allowed us to show that two independent methods give the same result, yielding that disordered Dirac fermions in one dimension are localized for all three considered potentials. Furthermore, we have related certain results obtained by means of transfer matrices for continuous Dirac fermions to those for lattice fermions.

In two spatial dimensions we have introduced a simplified model and confirmed the results for a special case by means of a perturbation theory. This expansion has also enabled us to verify the observed shift for the minimum of the smallest Lyapunov exponent.

For the two dimensional case we have shown that model $A$ with random gap exhibits a rich phase diagram. By means of finite-size scaling we have identified metal-insulator transitions and phase boundaries between different insulating phases exhibiting insulator-insulator transitions. Subsequently, we have calculated critical quantities like the critical exponents of the localization length. We have also considered a second method for discretization proposed by a different group. Already in the clean case our comparison of both models has shown substantial differences.

Since model $A$ allows to control the node degeneracy, we have been able to compare with appropriate tight-binding models. Both models considered in this thesis, the brickwork and the $\pi$-flux lattice, exhibit more than one Dirac cone and,

thus, inter-valley scattering is present. For random gap with finite mean we have found a transition from exponentially localized states to decaying states where diffusion in two dimensions can not be ruled out. At this transition we have found a critical exponent of the localization length $\approx 0.3$.

In addition to the random gap problem, we have considered random scalar potential for lattice fermions. Motivated by the mapping from the Chalker-Coddington model to a Dirac Hamiltonian, we have tried to confirm this mapping numerically. We have found another metal-insulator transition for model $A$ with broken valley symmetry and scalar disorder. We have discussed the scaling behavior for disorder and energy dependence of the localization length and have calculated critical exponents. Although the transition seems to be very similar to the quantum Hall transition, differences are substantial. Consequently, we cannot confirm the mapping and attribute this to the approximations made and to the discretization procedure.

The main findings in this thesis, in particular the phase transitions for lattice fermions with random gap and random scalar potential described by model $A$, suggest that critical exponents are rather model dependent than universal.

What is next? And what else can be done? Calculations for the discretized Dirac equation with random vector potential would be the next step continuing this work. It would be interesting to include appropriate next nearest neighbor terms in the brickwork lattice in order to break the valley symmetry and, thus, to lift the node degeneracy. Comparing to the discrete Dirac equation, we expect an Anderson transition, too. Another possibility would be to go beyond single layers. Implying to consider stacked lattices that are weakly coupled, for example two or three brickwork lattices, corresponding to bi- and trilayer graphene, or stacked discrete Dirac equations. Technically, this would mean to construct new transfer matrices which, of course, would be larger and, thus, computation time would increase. A further direction one could go, is to apply the transfer matrix to calculations of the conductance. Pendry et al. [82] have introduced an algorithm which allows to calculate the transmission coefficient and consequently the conductance by means of the Landauer formula.

Finally, there are still questions left and continuing this work is an exciting task that may lead to interesting results.

# A. Probability densities

For numerical calculations we have used random number generators for continuous distributions provided by the *Intel Math Kernel Library*.

The probability density function for uniform distributed random numbers is given by

$$f_{a,b}(x) = \begin{cases} \frac{1}{b-a} & \text{for } a < x < b \\ 0 & \text{otherwise.} \end{cases} \tag{A.1}$$

We define $a = \bar{x} - W/2$ and $b = \bar{x} + W/2$, thus the mean is given by $\bar{x}$ and $W = b - a$ is the width of the distribution. Accordingly, the standard deviation is given by

$$\frac{W}{\sqrt{12}} . \tag{A.2}$$

For normally distributed random numbers the probability density function reads

$$f_{\bar{x},\sigma}(x) = \frac{1}{\sigma\sqrt{2\pi}} \exp\left(-\frac{(x - \bar{x})^2}{2\sigma^2}\right) , \tag{A.3}$$

where $\bar{x}$ is the mean value and $\sigma$ the standard deviation.

When Cauchy distributed random numbers are used, its probability density is given by

$$f_{\bar{x},W}(x) = \frac{1}{\pi} \frac{W}{W^2 + (x - \bar{x})^2} . \tag{A.4}$$

Strictly speaking the Cauchy distribution has no mean and higher moments. Here, $\bar{x}$ is the center of the distribution and $W$ is the scale factor which denotes the half-width at half maximum.

# B. Transfer matrix for the Chalker-Coddington model

The transfer matrix is split into four sub-matrices according to figure 8.1

$$T_\alpha = A_\alpha B C_\alpha D .$$

The sub-matrices $A$ and $C$ are diagonal

$$[A_\alpha]_{ii} = \exp(i\phi_i(\alpha)) \qquad\qquad [C_\alpha]_{ii} = \exp(i\phi_i(\alpha)) \qquad (\text{B.1})$$

and the matrices $B$ and $D$ are composed of $2 \times 2$ blocks with non-zero entries

$$
\begin{aligned}
B_{ii} &= \cosh(\theta') & i &= 1, 2, ..., M & (\text{B.2}) \\
B_{2i,2i-1} &= B_{2i-1,2i} = \sinh(\theta') & i &= 1, ..., M/2 & (\text{B.3}) \\
D_{ii} &= \cosh(\theta) & i &= 2, 3, ..., M-1 & (\text{B.4}) \\
D_{2i,2i+1} &= D_{2i+1,2i} = \sinh(\theta) & i &= 1, ..., M/2 - 1 . & (\text{B.5})
\end{aligned}
$$

For cylindrical geometry (periodic boundary conditions)

$$
\begin{aligned}
D_{11} = D_{MM} &= \cosh(\theta) & (\text{B.6}) \\
D_{1M} = D_{M1} &= \sinh(\theta) & (\text{B.7})
\end{aligned}
$$

and for strip geometry

$$D_{11} = D_{MM} = 1 . \qquad (\text{B.8})$$

The values of $\theta$ and $\theta'$ correspond to the energy and are related by

$$\theta' = \operatorname{arcosh}\left(\coth(\theta)\right) . \qquad (\text{B.9})$$

The latter has for $\theta = \theta'$ the solution $\theta_c = \ln(1 + \sqrt{2})$.

# Bibliography

[1] P. W. ANDERSON, *Physical Review* **109**, 1492 (1958).

[2] B. KRAMER and A. MACKINNON, *Reports on Progress in Physics* **56**, 1469 (1993).

[3] P. A. LEE, *Reviews of Modern Physics* **57**, 287 (1985).

[4] E. ABRAHAMS and P. W. ANDERSON, *Physical Review* **42**, 637 (1979).

[5] J. L. PICHARD and G. SARMA, *Journal of Physics C: Solid State Physics* **14**, L127 (1981).

[6] G. BENETTIN, L. GALGANI, A. GIORGILLI, and J. M. STRELCYN, *Meccanica* , 21 (1980).

[7] A. MACKINNON and B. KRAMER, *Physical Review Letters* **47**, 1546 (1981).

[8] B. KRAMER, K. BRODERIX, and A. MACKINNON, *Physica A: Statistical and* **167**, 163 (1990).

[9] A. MACKINNON and B. KRAMER, *Zeitschrift für Physik B Condensed Matter* **53**, 1 (1983).

[10] M. SCHREIBER and M. OTTOMEIER, *Journal of Physics: Condensed* **4**, 1959 (1992).

[11] M. KAVEH, *Philosophical Magazine B* **52**, 521 (1985).

[12] I. M. SUSLOV, *Journal of Experimental and Theoretical Physics* **101**, 661 (2005).

[13] J. L. PICHARD and G. SARMA, *Journal of Physics C: Solid State Physics* **14**, L617 (2000).

[14] N. TIT and M. SCHREIBER, *Journal of Physics: Condensed Matter* **7**, 5549 (1995).

[15] F. EVERS and A. D. MIRLIN, *Reviews of Modern Physics* **80**, 1355 (2008).

[16] K. von Klitzing, G. Dorda, and M. Pepper, *Physical Review Letters* **45**, 494 (1980).

[17] B. Huckestein, *Reviews of Modern Physics* **67**, 357 (1995).

[18] J. T. Chalker and P. D. Coddington, *Journal of Physics C: Solid State Physics* **21**, 2665 (1988).

[19] F. D. M. Haldane, *Physical Review Letters* **61**, 2015 (1988).

[20] A. W. W. Ludwig, M. Fisher, R. Shankar, and G. Grinstein, *Physical Review B* **50**, 7526 (1994).

[21] C. Ho and J. T. Chalker, *Physical Review B* **54**, 8708 (1996).

[22] P. A. M. Dirac, *Proceedings of the Royal Society A: Mathematical, Physical and Engineering Sciences* **117**, 610 (1928).

[23] P. R. Wallace, *Physical Review* **71**, 622 (1947).

[24] K. S. Novoselov, A. K. Geim, and S. V. Morozov, *Science* **306**, 666 (2004).

[25] Y. Zhang, Y.-W. Tan, H. L. Stormer, and P. Kim, *Nature* **438**, 201 (2005).

[26] K. Ziegler, *Physical Review Letters* **97**, 266802 (2006).

[27] K. Ziegler, *Physical Review B* **75**, 233407 (2007).

[28] M. I. Katsnelson, *The European Physical Journal B* **51**, 157 (2006).

[29] K. S. Novoselov, A. K. Geim, S. V. Morozov, D. Jiang, M. I. Katsnelson, I. V. Grigorieva, S. V. Dubonos, and a a Firsov, *Nature* **438**, 197 (2005).

[30] V. P. Gusynin and S. Sharapov, *Physical Review Letters* **95**, 146801 (2005).

[31] R. F. Curl and R. E. Smalley, *Science (New York, NY)* **242**, 1017 (1988).

[32] H. Kroto, *Science (New York, NY)* **242**, 1139 (1988).

[33] J. Moore and L. Balents, *Physical Review B* **75**, 121306(R) (2007).

[34] C. L. Kane and E. J. Mele, *Physical Review Letters* **95**, 146802 (2005).

[35] D. Hsieh, D. Qian, L. Wray, Y. Xia, Y. S. Hor, R. J. Cava, and M. Z. Hasan, *Nature* **452**, 970 (2008).

[36] D. Hsieh, Y. Xia, L. Wray, D. Qian, a Pal, J. H. Dil, J. Oster-walder, F. Meier, G. Bihlmayer, C. L. Kane, Y. S. Hor, R. J. Cava, and M. Z. Hasan, *Science (New York, N.Y.)* **323**, 919 (2009).

[37] K. Ziegler, *Physical Review B* **79**, 195424 (2009).

[38] K. Ziegler and A. Sinner, *Physical Review B* **81**, 241404(R) (2010).

[39] M. Medvedyeva, J. Tworzydło, and C. W. J. Beenakker, *Physical Review B* **81**, 214203 (2010).

[40] G. Semenoff, *Physical Review Letters* **53**, 2449 (1984).

[41] A. H. Castro Neto, F. Guinea, and N. M. R. Peres, *Reviews of Modern Physics* **81**, 109 (2009).

[42] D. Abergel, V. Apalkov, J. Berashevich, K. Ziegler, and T. Chakraborty, *Advances in Physics* **59**, 261 (2010).

[43] S. Das Sarma, S. Adam, E. Hwang, and E. Rossi, *Reviews of Modern Physics* **83**, 407 (2011).

[44] K. S. Novoselov, Z. Jiang, and Y. Zhang, *Science* **315**, 1379 (2007).

[45] N. W. Ashcroft and N. D. Mermin, *Solid State Physics*, Saunders College, 1976.

[46] S. Datta, *Electronic transport in mesoscopic systems*, Cambridge University Press, 1995.

[47] F. Schwierz, *Nature nanotechnology* **5**, 487 (2010).

[48] T. Ohta, A. Bostwick, and T. Seyller, *Science* **313**, 951 (2006).

[49] P. Markoš and M. C. Soukoulis, *Wave Propagation*, Princeton University Press, 2008.

[50] Y. Imry, *EPL (Europhysics Letters)* **1**, 249 (1986).

[51] J. L. Pichard and G. André, *EPL (Europhysics Letters)* **2**, 477 (1986).

[52] F. Schwabl, *Quantenmechanik*, Springer, 2002.

[53] O. Klein, *Zeitschrift für Physik A Hadrons and Nuclei* **53**, 157 (1929).

[54] M. I. Katsnelson, K. S. Novoselov, and A. K. Geim, *Nature Physics* **2**, 620 (2006).

[55] A. F. Young and P. Kim, *Nature Physics* **5**, 222 (2009).

[56] N. Stander, B. Huard, and D. Goldhaber-Gordon, *Physical Review Letters* **102**, 026807 (2009).

[57] C. W. J. Beenakker, *Reviews of Modern Physics* **80**, 1337 (2008).

[58] A. Crisanti, G. Paladin, and A. Vulpiani, *Products of random matrices in statistical physics*, Springer, 1993.

[59] M. L. Mehta, *Random matrices*, Elsevier, 2004.

[60] V. I. Oseledec, *Transactions of the Moscow Mathematical Society* **19**, 197 (1968).

[61] W. G. Faris, P. Bougerol, and J. Lacroix, *Products of Random Matrices with Applications to Schrödinger Operators*, Birkhäuser, 1985.

[62] S.-J. Xiong and Y. Xiong, *Physical Review B* **76**, 214204 (2007).

[63] P. Markoš, *Acta Physica Slovaca* **56**, 561 (2006).

[64] A. Hill and K. Ziegler, *arXiv:1211.2329* (2012).

[65] M. E. Fisher, *Physical Review Letters* **28**, 1516 (1972).

[66] F. Wegner, *Zeitschrift für Physik B Condensed Matter* **36**, 209 (1980).

[67] J. Tworzydło, C. Groth, and C. W. J. Beenakker, *Physical Review B* **78**, 235438 (2008).

[68] L. Susskind, *Physical Review D* **16**, 3031 (1977).

[69] R. Stacey, *Physical Review D* **26**, 468 (1982).

[70] K. Ziegler, *Physical Review B* **53**, 9653 (1996).

[71] I. M. Lifshits, S. A. Gredeskul, and L. A. Pastur, *Introduction to the theory of disordered systems*, Wiley Interscience, 1988.

[72] B. Derrida, K. Mecheri, and J. L. Pichard, *Journal de Physique* **48**, 733 (1987).

[73] J. T. CHALKER, N. READ, V. KAGALOVSKY, B. HOROVITZ, Y. AVISHAI, and A. W. W. LUDWIG, *Physical Review B* **65**, 012506 (2001).

[74] V. KAGALOVSKY and D. NEMIROVSKY, *Physical Review Letters* **101**, 127001 (2008).

[75] U. ECKERN and K. ZIEGLER, *Journal of Physics: Condensed Matter* **10**, 6749 (1998).

[76] K. V. KLITZING, *Reviews of Modern Physics* **58**, 519 (1986).

[77] K. SLEVIN and T. OHTSUKI, *arXiv:1203.1384* (2012).

[78] K. SLEVIN and T. OHTSUKI, *Physical Review B* **80**, 041304(R) (2009).

[79] B. HUCKESTEIN, *Physical Review Letters* **72**, 1080 (1994).

[80] Y. HATSUGAI and P. LEE, *Physical Review B* **48**, 4204 (1993).

[81] Y. MORITA and Y. HATSUGAI, *Physical Review Letters* **79**, 3728 (1997).

[82] J. PENDRY, A. MACKINNON, and P. ROBERTS, *The Royal Society* **437**, 67 (1992).

# List of publications

A. Hill, S. A. Mikhailov, K. Ziegler, "*Dielectric function and plasmons in graphene*", EPL **87**, 27005 (2009)

A. Hill, A. Sinner, K. Ziegler, "*Valley symmetry breaking and gap tuning in graphene by spin doping*", New J. Phys. **13**, 035023 (2011)

A. Hill, K. Ziegler, "*Scaling behavior of disordered lattice fermions in two dimensions*", *arXiv:1211.2329* (2012)

A. Hill, A. Sinner, K. Ziegler, "*Optical Hall conductivity of gapped graphene*", Eur. Phys. J. B **86**, 53 (2013)

# Conference contributions

A. Hill, S. A. Mikhailov, K. Ziegler, "*Plasmons in graphene*", DPG Spring Meeting 2009 (Poster HL 14.18)

A. Hill, A. Sinner, K. Ziegler, "*Valley symmetry breaking and gap tuning in graphene by spin doping*", DPG Spring Meeting 2012 (Talk HL 15.8)

A. Hill, A. Sinner, K. Ziegler, "*Valley symmetry beaking and quantum Hall effect without magnetic field in graphene*", Quantum Dynamics of Nano-Structured Systems (QDNS) 2012 (Poster)

# Danksagung

Abschließend möchte ich mich bei all denen bedanken, die zum erfolgreichen Abschluss dieser Dissertation beigetragen haben.

In erster Linie möchte ich mich bei Herrn Prof. Dr. Klaus Ziegler dafür bedanken, dass er mir die Möglichkeit gab bei ihm zu promovieren. Die Diskussionen mit ihm waren stets fruchtbar und er hat mich ermutigt eigene Ideen zu verfolgen.

Ich bedanke mich bei Herrn Prof. Dr. Gert-Ludwig Ingold für die Anfertigung des Zweitgutachtens und bei Herrn Jun.-Prof. Dr. Liviu Chioncel und Herrn Dr. Hubert Krenner für die Bereitschaft meiner Prüfungskommission anzugehören.

Ein besonderer Dank gilt Herrn Prof. Dr. Ulrich Eckern für seine Unterstützung und dafür, dass ich am Symposium QDNS'12 mitwirken durfte. Das gab mir die Gelegenheit hinter die Kulissen einer Tagung zu sehen und interessante Persönlichkeiten kennenzulernen.

Für die Bereitschaft mir jederzeit bei Fragen zu Helfen, für zahlreiche Diskussionen und für das Korrekturlesen dieser Arbeit danke ich Dr. Andreas Sinner.

Zudem danke ich allen Mitgliedern des Lehrstuhls Theoretische Physik II und I und natürlich bei unserer Sektretärin Marion Amling für die Unterstützung in allen organisatorischen Dingen.

Außerdem danke ich Joseph Beer, Stefan Götz, Johannes Weirather, Matthias Ziegler. Vornehmlich danke ich Armin Seibert, Michael Stark und Martin Wolf für das Korrekturlesen und für die vielen Gespräche in der gemeinsamen Mittagspause in denen das Thema nicht immer Physik war.

Für den Rückhalt und die Unterstützung danke ich meinen Eltern Anna und Alexander Hill und insbesondere meiner Schwester Lisa für wertvolle Korrekturen, etliche Fahrdienste und Eventmanagement.

Für ihre Unterstützung, ihr Verständnis und ihre Geduld, während dieser für mich wichtigen Zeit, danke ich ganz besonders herzlich meiner Partnerin Simone Neumann.

# Lebenslauf

## Persönliche Daten

Name:             Antonio Hill

Geburtsdatum:     10.05.1980

Geburtsort:       Augsburg

## Studium

bis Feb. 2013        Promotion bei Herrn Prof. Dr. K. Ziegler

10/2003 - 8/2009     Studium der Physik mit Abschluss: Diplom

## Schulbildung

2000 - 2002        Städtische Berufsoberschule Augsburg mit Abschluss: Fachgebundene Hochschulreife

1992 - 1996        Realschule Wertingen mit Abschluss: Mittlerer Reife

1990 - 1992        Gymnasium Wertingen

1986 - 1990        Grundschule Hochzoll Nord

## Berufsausbildung

1996 - 1999        Ausbildung zum Indutrieelektroniker mit IHK Abschluss

## Wehrersatzdienst

2002 - 2003        Zivildienst, Sozialstation St. Blasius